

Generation and dissipation of Alfvén-cyclotron turbulence in the solar corona and solar wind and related ion differential heating and acceleration

Dissertation

zur Erlangung des mathematisch-naturwissenschaftlichen Doktorgrades

“Doctor rerum naturalium”

der Georg-August-Universität Göttingen

vorgelegt von

Yana Georgieva Maneva

aus Sofia, Bulgarien

Göttingen 2010

Bibliografische Information der Deutschen Nationalbibliothek

Die Deutsche Nationalbibliothek verzeichnet diese Publikation in der Deutschen Nationalbibliografie; detaillierte bibliografische Daten sind im Internet über <http://dnb.d-nb.de> abrufbar.

Referent: Prof. Dr. Stefan Dreizler

Korreferent: Prof. Dr. Eckart Marsch

Tag der mündlichen Prüfung: 24.09.2010

ISBN 978-3-942171-39-7

uni-edition GmbH 2010

<http://www.uni-edition.de>

© Yana Georgieva Maneva



This work is distributed under a
Creative Commons Attribution 3.0 License

Printed in Germany

Contents

Summary	5
1 Introduction	7
1.1 The solar corona and the solar wind - overview and plasma parameters . . .	7
1.1.1 Solar corona	7
1.1.2 Solar wind: types and origin	9
1.1.3 Plasma composition and collisional conditions	11
1.2 Observations of Alfvén waves in the solar corona and fast solar wind . . .	16
1.3 Motivation, scope and outline of the present work	18
2 Plasma kinetics in the corona and the solar wind	23
2.1 Common features, observed in the corona and the fast solar wind	24
2.1.1 Velocity distributions	25
2.1.2 Temperature profiles and kinetic temperature ratios	27
2.1.3 Ion anisotropies and differential streaming	30
3 Analytical description of nonlinear couplings in multi-species plasmas	35
3.1 Parametric instabilities	35
3.1.1 Nonlinear nature and different types	36
3.1.2 Pump wave dispersion relation – setting up the ground state . . .	37
3.1.3 Ground state perturbations – instability analysis	38
3.1.3.1 General derivation – Equation of motion	38
3.1.3.2 General derivation – Maxwell’s equations	42
3.1.4 Dispersion relation for electron-proton plasma case	43
3.1.5 Electron-proton-alpha particles	44
3.1.6 Inclusion of oxygen ions	45
3.2 Kinetic damping mechanisms	47
3.2.1 Landau damping and cyclotron resonance	47
3.2.2 Quasilinear diffusion	48
4 Numerical modeling of nonlinear processes in multi-species plasmas - hybrid simulations	51
4.1 Description of the code	51
4.1.1 From Vlasov to superparticles: the idea of PIC codes	51
4.1.2 1D hybrid code	55
4.2 Initial setup	57

4.2.1	Physical considerations	57
4.2.2	Numerical issues	59
4.3	Application to parametric instabilities of Alfvén-cyclotron waves	60
5	Dissipation of nonlinear Alfvén-cyclotron waves – impact on ion distributions in multi-species plasma	63
5.1	Trapping of particles in large-amplitude waves	63
5.2	Heating and acceleration of protons and alpha particles via wave-particle interactions	64
5.3	Heating and acceleration in the presence of relative drift	72
6	Regulation of ion drifts and anisotropies via parametrically unstable Alfvén- cyclotron waves	91
6.1	Simulation study and numerical results	91
7	Heating and acceleration of heavy ions in CHs and fast solar wind	103
7.1	Initial setup	104
7.2	Trapping, heating and acceleration	105
8	Conclusions and outlook	115
A	Kinetic dispersion relation for the pump wave - Sonnerup’s solution	119
	Bibliography	121
	Publications	129
	Acknowledgements	131
	Lebenslauf	133

Summary

Nonthermal ion velocity distribution functions are ubiquitous in the fast solar wind, which is permeated by large-amplitude Alfvén waves and plasma wave turbulence, including ion-cyclotron waves, observed recently near 1 AU. Remote sensing of the solar corona by means of ultraviolet spectroscopy and modeling of *in situ* measured data by Helios, Ulysses and Wind spacecrafts indicate that similar anisotropic kinetic ion features are present also in the solar atmosphere, especially in coronal holes where Alfvén waves are considered to be important. In the present work we have investigated the role of parametric instabilities and the consequent wave-particle interactions of parallel monochromatic nonlinear Alfvén-cyclotron waves with solar wind ions as a possible source for the anisotropic preferential ion heating and differential acceleration, as observed both in coronal holes and the fast solar wind. For this aim we performed 1D nonlinear hybrid simulations, treating the electrons as a charge- and current-neutralizing fluid, and use the particle-in-cell approach to describe the ions in a fully kinetic manner. We consider an initially homogeneous magnetized plasma, with a constant magnetic background field, on top of which we superimpose high-frequency transverse fluctuations, corresponding to a nonlinear monochromatic Alfvén-cyclotron wave that propagates along the constant background magnetic field. The code is initialized with different initial plasma β_s values, ranging from rather low, $\beta_s = 0.02$, as typical for a solar coronal hole, to high thermal speeds, $\beta_s = 0.35$, characteristic for the outgoing solar wind. The pump-wave frequencies used for the simulations vary between 0.2 and $0.3 \Omega_p$. After the onset of parametric instabilities, particles are trapped in the potential well of daughter ion-acoustic waves, whose Landau damping results in parallel heating and ion differential acceleration. Simultaneously, the formation of ion beams is observed, whose strength depends on the phase speed of the longitudinal daughter waves. In addition, the pump wave forces the entire ion velocity distribution functions to gyrate in transverse direction with a specific bulk velocity, which depends on the gyrofrequency of the ion species, as well as on their parallel drift speed. As the pump wave decays, the ions are no longer obliged to perform this coherent motion, and they start to diffuse and heat in transverse direction, thus filling in the phase space at low velocities. Then, depending on the phase speed of the transverse daughter waves and the gyrofrequency of the ions, the latter can get additionally heated by cyclotron resonance effects.

In most of the cases, the ion beams are found to be rather persistent and long lived. Simultaneously, the minor ions are differentially accelerated and preferentially heated up to high temperatures with a more than mass proportional heating rate, $T_h > m_h/m_p T_p$, as observed *in situ* in the fast solar wind. The model results demonstrate preferential and anisotropic heating for the heavy ions as well, and their differential acceleration is investigated.

1 Introduction

1.1 The solar corona and the solar wind - overview and plasma parameters

1.1.1 Solar corona

The solar corona is the very hot outermost layer of the solar atmosphere (cf. Fig. 1.1), which has a volume much larger than the Sun itself. It consists of a highly dilute almost fully ionized plasma. Its temperature varies around several million degrees in Kelvin with typical values between $1 - 2 \times 10^6$ K at 1.3 solar radius, however, in the hottest regions it can reach out from 8MK to about 20MK. Thus on average the coronal temperature is by two orders of magnitude higher than the temperature of the denser chromosphere beneath. This sharp increase of the temperature (from 10^4 K at the upper chromosphere to 10^6 K) and the related decrease in particle densities (from 10^{10}cm^{-3} at the upper chromosphere to 10^7cm^{-3} in the corona, see 1.1.3) occur in a very narrow region of the Sun's atmosphere, called the transition region. The transition region starts at altitudes of about 2Mm above the chromosphere and is less than 0.2Mm thick. It is related to the open problem, which keeps on long puzzling scientists, namely what suddenly makes the corona so drastically hot, even though it is furthest away from the heat producing radioactive core. To be able to answer the so called "coronal heating problem", though, one needs precise information about the magnetic fields in the corona. Since the corona is rather dilute and optically very thin (except for X-ray and UV radiation) it is difficult to use spectroscopy means to derive the coronal magnetic field and any "in situ" measurements are far beyond the scope of the contemporary space missions. Studies on magnetic field extrapolations, based on underlying photospheric or chromospheric data, can give clues about the magnitude and the global structure of the magnetic field (ref. to Figs. 1.2 and 1.3), but yet they are unable to provide reliable information about the small-scale structures, nor they are able to track any wave activities. For a thorough review on the solar corona see [Aschwanden (2005)]. As we shall see in the following sections, the solar corona extends further into space, supplying material for the solar wind, that passes by the Earth's orbit and travels far out into the heliosphere (see Fig. 1.4). The coronal plasma is gravitationally stratified and turbulent. It is strongly driven by the underlying photospheric magnetoconvection, which is continuously pushing around the magnetic field lines reaching out into the corona. Thus the magnetic field contains ample free energy for driving plasma macro- and micro-instabilities. Consequently, magnetohydrodynamic as well as kinetic plasma waves and associated wave-particle interactions are expected to play a major role. More discussions on this issue will follow in Chapter 2 and Sec. 1.2.

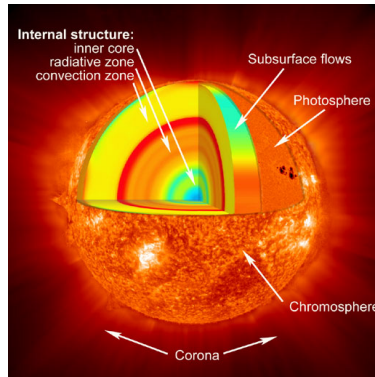


Figure 1.1: Overview of the internal structure of the Sun with its constituent layers. In the center is the hydrogen burning core, where thermo-nuclear reactions take place. Next come the radiative zone, where the energy transfer is done by means of radiation. Afterwards follows the convection zone, where the surface magnetic field is being generated. The surface layers (photosphere, chromosphere and the corona) are clipped from actual SOHO images of the Sun (Courtesy of SOHO consortium – international cooperation between ESA and NASA).

Depending on the magnetic activity, the solar corona has three major features: (1) active regions (associated with strong magnetic field concentrations and related to the visible sunspots); (2) quiet Sun regions and (3) very tenuous (almost “empty”) parts, called coronal holes (hereafter CHs). The occurrence and position of the latter three strongly depends on the magnetic field of the Sun and hence on the solar cycle. On average during solar minimum the CHs are mostly situated in the polar regions (in the northern and southern hemispheres) and the corona consists mainly of “quiet Sun” regions. During this period there are less and smaller active regions, predominantly situated in the equatorial regions. During maxima of solar activity the position of the CHs and active regions is rather mixed: there are more parts of the Sun covered by active regions (to be found also at higher latitudes) and CHs can be found at much lower latitudes (see Fig. 1.5).

Normally, the active regions constitute just a small fraction of the total surface area. The reason why they are called “active” is that the strength and topology of the magnetic field there changes, giving rise to large coronal loops filled with plasma, and many large-scale dynamical processes (like solar flares, prominences and coronal mass ejections) originate from there. On the contrary within the resolution of the early missions the rest of the Sun used to form a smooth background, made of plasma at rest, with no prominent motions or activity. Nowadays it is known that the “Quiet Sun”, whose small features could not be resolved before, is not “quiet” either, but is associated with plenty of small-scale activities, like microflares, explosive events, mini coronal mass ejections or X-ray jets. The third major coronal constituents, namely the CHs, are the tenuous funnel-like coronal regions (with a variable density, that can be 100 times lower than the rest of the corona), dominated by unipolar concentrations of open magnetic field lines. They have

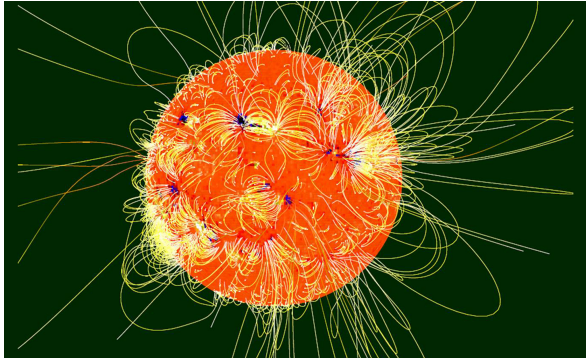


Figure 1.2: Non-linear force-free extrapolation of the global coronal magnetic field [T. Wiegelmann and S.K. Solanki (2004)].

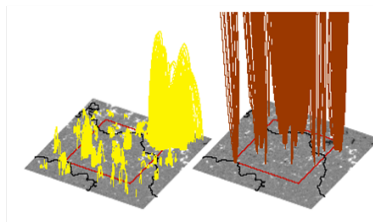


Figure 1.3: Non-linear force-free extrapolation of the coronal magnetic field in a coronal hole [T. Wiegelmann *et al.* (2005)]. The yellow curves to the left represent closed loop structures, whereas the brown lines to the right correspond to open magnetic field lines.

lower density than their surroundings and therefore they appear darker than the Quiet Sun during an eclipse or in X-rays and EUV images of the corona. Nowadays it is generally believed that CHs give origin to the fast solar wind [Tu *et al.* (2005)]. The plasma source are the small magnetic fields created by convection cells in the solar atmosphere that confine the plasma and transport it into the narrow necks of the coronal funnels, located about 20 Mm above the photosphere. When these magnetic field lines reconnect, the plasma is released into the funnel, thus supplying material to the fast solar wind (see Figs. 1.8 and 1.9).

1.1.2 Solar wind: types and origin

First estimation of the million degrees Kelvin hot corona was done in the 1930's by observations during a solar eclipse. Later, in 1958, Sidney Chapman [Chapman (1958)] showed that a gas under such a high temperature cannot be static, but due to its extreme heat conduction should expand out into space and reach out beyond Earth's orbit. The idea of the expanding corona was further developed by Eugene Parker [Parker (1958)],

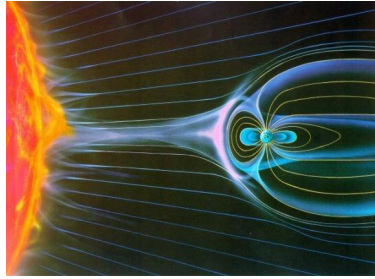


Figure 1.4: Artistic view of the outflowing solar wind, attached to open magnetic field lines after solar eruptions. As it stretches out into space to 1AU, the solar wind hits the Earth’s magnetosphere and bends the geomagnetic field lines, which shield the Earth from the solar radiation. Part of the wind reaches the Earth’s ionosphere through the poles and is responsible for the creation of aurorae (or better known as the polar lights). Most of the wind passes by to continue its quest throughout the heliosphere.

who developed the first hydrodynamic model for the acceleration of the solar wind. Later, it was realized that the solar magnetic field plays an important role and a pure hydrodynamic model cannot reproduce the interplanetary gas pressure far away from the source. Thus the solar wind is a supersonic and super-Alfvénic flow, whose acceleration saturates within 0.1 AU. However, due to its complex nature, it is still difficult for the contemporary science to build up a complete model of the solar wind, including its different types and all its multi-scale features.

As the solar wind plasma is highly electrically conductive (the so-called frozen-in conditions are satisfied), further away from the Sun where the magnetic field strength drops down, the solar magnetic field lines are dragged away by the flow, and due to the solar rotation they are wound up and form the so-called Parker’s spiral. The wind attains a constant terminal speed, and its density then decreases radially in proportion to the square of the radial distance.

There are three main types of solar wind, respectively termed the slow solar wind, fast solar wind and transient wind [Marsch (2006)]. The **slow solar wind** has an average velocity of about 400 km/s and a temperature of about $1.4 - 1.6 \times 10^6$ K. Its composition closely matches that of the corona and it represents an unsteady flow that is believed to arise from the tips and edges of temporarily open coronal streamers or from opening coronal loops and active coronal regions. The slow wind strongly depends on the solar cycle. It appears to originate from a region around the solar equatorial belt, known as the “streamer belt”. Coronal streamers extend outward from this region, carrying plasma from the interior along temporarily open, but otherwise closed magnetic loops. Observations show that emission of the slow solar wind occurs between latitudes of $30^\circ - 35^\circ$ around the equator during the solar minimum. However, as the minimum wanes, the slow wind expands toward the poles and by the time when maximum of solar activity is reached, it becomes more isotropic in latitude and is emitted not only from streamer belts, but from the poles as well (see Fig. 1.6). The slow solar wind is twice denser and more variable

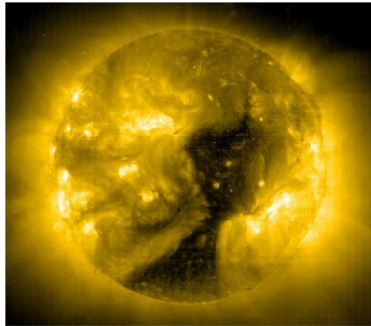


Figure 1.5: An extreme ultraviolet image of an equatorial coronal hole taken in the Fe XV line by the EIT telescope on board of SOHO on 7th January 2002.

in intensity than the fast solar wind and it bears a more complex nature, with turbulent regions and large-scale structures.

By contrast, the **fast solar wind** remains “steadier” to the changes of the solar magnetic activity. It has a typical velocity of 750 km/s (varying between 600-800 km/s), a temperature of 8×10^5 K and it nearly matches the composition of the solar photosphere, supporting the idea for its CHs origin. The fast solar wind is less turbulent, but rather carries many coherent large-amplitude waves (see the following section 1.2). Though a lot of effort in this direction has been thrown it is still not well-established how the fast wind accelerates from its 10 km/s value at a height of 20 Mm above the photosphere to its observed values of up to 800 km/s at Earth’s orbit. The origin of the slow solar wind remains even less clear [Schwadron and McComas (2003)]. Most likely it involves magnetic reconnection, which leads to transient openings of coronal loops and feeds plasma to the slow wind.

The third type - the **transient wind** - is related primarily to big flares and coronal mass ejections (CMEs) that may in the interplanetary space later evolve into magnetic clouds. Just like the slow solar wind, the CMEs strongly depend on the phase of the solar cycle. Their frequency of occurrence ranges from about one every other day near solar minimum to at least 5 - 6 per day near solar maximum. The average mass based on LASCO (the coronagraph on board of SOHO) is 1.6×10^{12} kg. Since the coronagraph images are of two-dimensional nature, this gives a lower mass limit for the CME’s mass. Most CMEs originate from active regions, though they can be launched from the “quiet Sun” as well. Their position varies with the magnetic activity. During solar minimum, CMEs form predominantly in the coronal streamer belt near the solar magnetic equator. During maximum they originate from active regions with more homogeneous latitudinal distribution.

1.1.3 Plasma composition and collisional conditions

The solar wind consists of electrons, protons, alpha particles (that are already referred to as minor ions, as they constitute only about 5% of the electron density) and tenuous populations of heavy ions (with atomic number >2 , predominantly oxygen, but also dif-

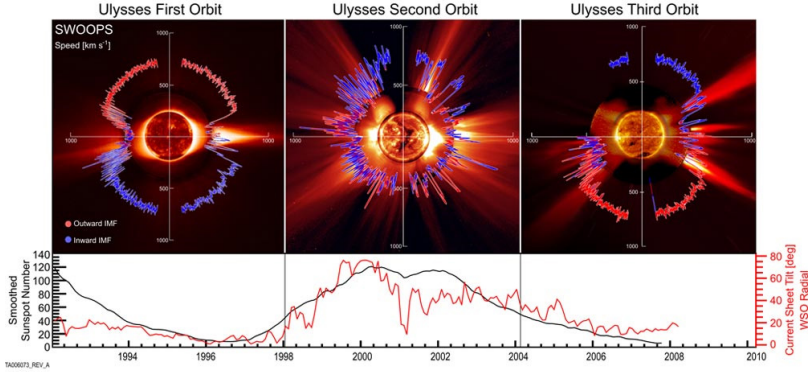


Figure 1.6: Dependence of the solar wind on the solar cycle based on solar wind observations over the poles of the Sun (SWOOPS) during the three Ulysses orbits. Polar plots of the solar wind speed versus latitude are shown on top. Below are the smoothed number of sunspots per year, together with the current sheet tilt angle, after [McComas *et al.* (2008)]. During minimum of the solar activity fast wind dominates over the polar regions, whereas the slow wind appears confined within the equatorial plane. During solar maximum the slow wind becomes homogeneously distributed in latitude space. The data from the third orbit indicates that the solar wind is about 25% less powerful than it was in the previous solar minimum cycle. The solar images are taken by EIT on board of SOHO, Mauna Loa K-coronameter and C2 instrument of LASCO spectrometric coronagraph on board of SOHO.

ferent ionization states of carbon, nitrogen, neon, magnesium, silicon, iron ions and more, see Fig. 1.7). Kinetic plasma physics deals with their collective behavior as a statistical ensemble. Particle spectrometers on board of contemporary space missions enable us to measure “in situ” the composition of the solar wind and the three-dimensional velocity distribution functions (VDFs) of the particles. The Boltzmann kinetic plasma theory (or Vlasov in absence of collisions) provides an adequate means for a theoretical description of the non-thermal features in the corona and fast solar wind (see next Chapter 2 for observational evidence). Key issues of kinetic physics are to address the coronal origin and acceleration of the wind and the spatial and temporal evolution of the particles’ VDFs. They are shaped through the forces of the solar gravitational field, the average-mesoscale and fluctuating-mesoscale electric and magnetic fields of the interplanetary space, and through multiple microscale kinetic processes like binary Coulomb collisions and collective wave-particle interactions [Marsch (2006)].

Let us now see what is the role of Coulomb collisions in the corona and the fast solar wind and what makes the wave-particle interaction important under those conditions. The number of collisions N between any two particles in the solar wind is generally very low (higher for ions and very low for electrons) and the Knudsen number $Kn = \lambda/L$ (given by the ratio of the mean free path λ over the characteristic length of the system

Element	Abundance Relative to Oxygen
H	1900 ± 400
He	75 ± 20
C	0.67 ± 0.10
N	0.15 ± 0.06
O	1.00
Ne	0.17 ± 0.02
Mg	0.15 ± 0.02
Si	0.19 ± 0.04
Ar	0.0040 ± 0.0010
Fe	0.19 ± 0.10, - 0.07

Figure 1.7: Long-term average abundances in the solar wind relative to the oxygen species [“Solar Wind” by J. Gosling in “*Encyclopedia of the Solar System*” (2007)].

Parameter	Chromosphere (1.01R _S)	Corona (1.3R _S)	Solar wind (1AU)
n_e [cm ⁻³]	10 ¹⁰	10 ⁷	10
T_e [K]	10 ³	1 - 2 * 10 ⁶	10 ⁵
λ [km]	10	10 ³	10 ⁷

Table 1.1: Mean free paths in the solar atmosphere and beyond [Marsch (2006)].

L) is of the order of unity or higher. This causes a break down in the classical transport theory and a need for kinetic treatment of the binary collisions, including the contribution of the wave-particle interactions, which allow for indirect energy and momentum transfer between the particles via the waves. This makes kinetic processes like micro-instabilities and wave-particles interactions very important in space plasmas, particularly in the hot solar corona and the tenuous solar wind, where we have many particle species far from local thermodynamical equilibrium. Typically for the slow wind there is approximately one collision $N = 1$ per 1AU, i.e. as the ions travel from the Sun to the Earth, whereas the fast wind is even strongly collisionless with a rate of about 1 collision by the time it reaches Jupiter or Neptune at about 10AU. We should note, though, that just a few collisions are sufficient to remove extreme anisotropies in the ion distributions, but still the enormous mean free paths lead to strong deviations from simple Maxwellian distributions and coherent fluid-like motion. Comparison between the mean free paths of the ions, the electron temperatures and densities in the different layers of the solar atmosphere and the solar wind are given in table 1.1.3 below. We can see that the chromosphere is dominated by collisions as the mean free path λ there is by orders of magnitude shorter than the corresponding values in the corona and the solar wind. Generally the fast solar wind is more collisionless than the slow wind (being denser). Therefore the particle distribution functions in the fast wind exhibit stronger deviations from thermal equilibrium, where the slow wind stays more isotropic. Another reason for the strong anisotropies in the fast solar wind is attributed to the presence of many large-amplitude waves of monochromatic nature, unlike the lower-amplitude turbulent structures, characteristic for the slow solar wind.

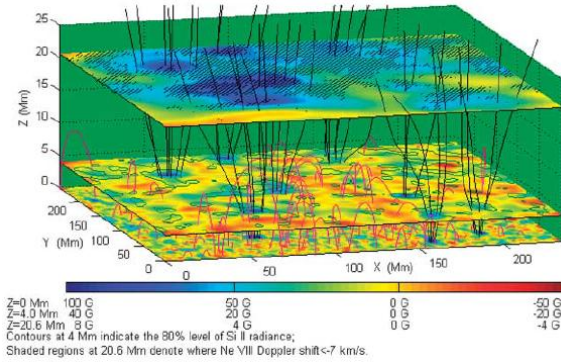


Figure 1.8: Magnetic field structures in the 3-D solar atmosphere. The black and the red curves illustrate open and closed magnetic field lines. As the magnetic field decreases in height, Z , the scales on the colour bars change. At 4 and 20.6 Mm respectively the Si II radiance and the Ne VIII Doppler shifts (smaller than -7 km/s) are compared with the extrapolated B_z . The shaded areas indicate where the Ne^{7+} outflow speed is larger than 7 km/s [Tu *et. al.* (2005)].

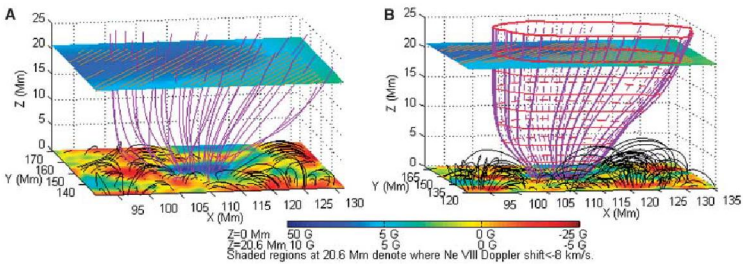


Figure 1.9: Magnetic funnel in the solar atmosphere: (A) Open field lines and correlation with the Ne^{7+} outflow speed larger than 8 km/s (dark shading). (B) Illustration of the funnel boundary and magnetic unipolar flux constriction by adjacent, surrounding bipolar loops [Tu *et. al.*(2005)].

The mean free path here is determined as the ratio of the thermal speed of electrons to the collision frequency $\lambda = v_{\text{th},e}/\nu_{ei}$. If we consider a fully ionized plasma, the collisions with neutrals can be neglected and the classical collision rate between electron and ions is given by [Braginskii (1965)]

$$\nu_{ei} = \frac{4\sqrt{2}\pi n_i Z_i^2 e^4 \ln \Lambda}{3m_e^{1/2} T_e^{3/2}}. \quad (1.1)$$

The collision frequency between two ions is slightly different

$$\nu_{ii} = \frac{4\sqrt{\pi} n_i Z_i^4 e^4 \ln \Lambda}{3m_i^{1/2} T_i^{3/2}}, \quad (1.2)$$

where the Coulomb logarithm in the corona takes typical values of $\ln \Lambda \approx 19$, m_e , e , T_e are the mass, charge and temperature of the electrons, n_i is the ion density and Z_i - the ion charge number of the quasi-neutral plasma $\sum_i n_i Z_i \approx n_e$. As we keep these expressions in mind we can easily understand what makes the corona and the solar wind so highly-collisionless in comparison with the much denser chromospheric plasma in table 1.1.3. Since the Coulomb logarithm changes slowly, the major factors in the collision frequency are the temperature and the density. Now the chromospheric plasma is very dense and much colder in comparison to the corona, so it is dominated by collisions. In the corona the density is decreasing and the temperature goes high, which makes it almost collisionless. Similar thing happens to the slow solar wind, whereas the even less dense plasma in CHs and fast solar wind is practically collisionless. Our entire analysis addresses the collisionless conditions in CHs and fast solar wind.

Another important parameter, characteristic for the solar plasma is the so-called plasma β , determined by the ratio of the thermal to magnetic pressure. In principle the plasma β is a fluid term, which originates from the momentum equation in an ideal fluid description. One can easily generalise it for a multi-fluid with s number of species

$$\beta_s = \frac{p_s}{\rho_B} = \frac{2n_s k_B T_s}{B^2/8\pi}. \quad (1.3)$$

The role of the plasma β is to show which force dominates in the system and determines the plasma behavior - whether the pressure gradient or the Lorentz force. Thus when $\beta < 1$ in an ideal fluid the plasma is guided by the magnetic field, whereas for $\beta > 1$ the field strength is weaker and the plasma motion determines the direction of the magnetic field lines. The values of the plasma β in the Sun vary with height as shown on Fig. 1.10. The plasma β is rather important for determining the dominant heating mechanism of the plasma system under consideration, be it the solar corona or the solar wind. It drastically changes the character of the linear plasma micro and macro-instabilities, the non-linear wave-wave couplings and the wave-particle interactions, causing different features in the particle distribution functions. As will be shown in Chapters 6 and 7, our analysis concentrates on low plasma β regions in CHs and fast solar wind near the Sun, $\beta \ll 1$.

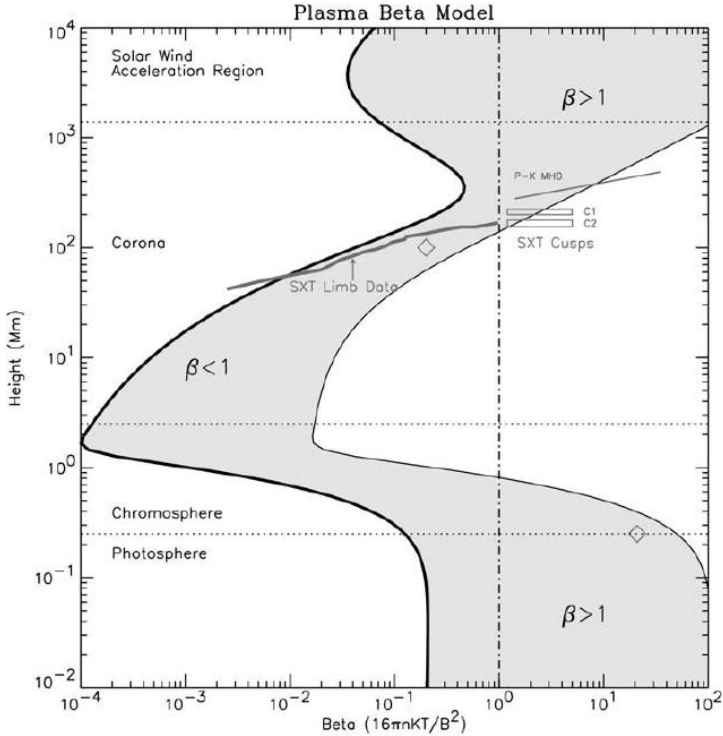


Figure 1.10: Variation of the plasma β within the solar atmosphere [G. Gary (2001)]. The two dark lines correspond to magnetic field strength of 100G and 2500G respectively.

1.2 Observations of Alfvén waves in the solar corona and fast solar wind

There are different ways to detect the presence of electromagnetic waves in the corona and the solar wind. Since we have no direct access to the solar corona, we can infer information about the wave propagation there only by means of remote sensing. One can use photometry by space-born or ground-based telescopes to follow the plasma motion of different solar structures, like coronal loops, prominences or spicules, and deduce the phase speed of the waves. One can also utilize spectroscopy to invert the wave properties, assuming a certain atmospheric model. Both ways are however limited by the resolution of the CCD cameras and hence can only work for relatively low-frequency MHD type waves (ways below any ion-cyclotron gyration). On the contrary, due to the very low density in the solar wind, in order to detect waves activity we rely on “in situ” measurements with wave-analyzers on board of space-shuttles. A list of solar wind related space

missions that carried on board a waves analyser is presented on Fig. 1.11 together with the dates of launch and end of the mission, the orbit and the distance from the Sun in AU during the pericentre and apocentre.

In the low frequency (MHD) limit, the perturbation of the magnetic field ($\delta\mathbf{B}$) and the averaged motion of the ions ($\delta\mathbf{V}$) are parallel to each other and transverse to the direction of propagation

$$\frac{\delta\mathbf{B}}{B_0} = \pm \frac{\delta\mathbf{V}}{V_A}. \quad (1.4)$$

where the Alfvén velocity ($V_A = B_0 / \sqrt{4\pi\rho_0}$) is the phase speed of the Alfvén waves, B_0 is the strength of the background magnetic field and ρ_0 is the mass density. (We should note that for the hybrid description in our analytical and simulation analysis (Chapters 3-6) we slightly redefine the Alfvén speed, substituting the mass density with the product of the proton mass and electron number density $\rho = m_p n_e$.) This relation describes parallelly propagating Alfvén waves, whose existence was predicted for the first time by Hannes Alfvén [Alfvén (1942)].

Alfvén waves have long been observed in the solar wind in the early 1970s [Unti and Neugebauer (1968); Belcher and Davis (1971)]. Since they are rather low-frequency normal modes of an MHD system, it is difficult to dissipate them and they are expected to permeate the whole solar atmosphere. Alfvén waves are ubiquitous in the solar wind, where the Alfvénic correlation Eq. (1.4) is often satisfied, particularly in the fast solar wind and at shorter heliocentric distances [Bruno and Carbone (2005)]. Most of the Alfvén waves observed in the solar wind are outward (anti-sunward) propagating and probably originate from the solar surface [Tu and Marsch (1995); Erdelyi and Fedun (2007)]. However, inward Alfvén waves are also observed in the solar wind and as we travel further away from the Sun their power decreases more slowly than the power of the outward propagating waves [Bruno and Carbone (2005)]. As sunward propagating waves cannot originate from the Sun and travel in a super-Alfvénic wind, they must be locally generated by some physical process, involving mode-conversion and/or cascading via wave-wave interactions. Now, there is a lot of wave-power in the large-amplitude forward propagating Alfvén waves in the solar wind, so they can serve as an energy source for such interactions, generating the observed backward propagating fluctuations. And since low frequency Alfvénic fluctuations in the solar wind are typically robust to collisionless damping mechanisms, parametric instabilities are of particular interest for the dissipation of such Alfvén waves (see Chapter 3, Sec. 3.1).

Upward propagating Alfvén waves in the chromosphere and transition region have recently been identified in Ca II H 3968 Å images taken by the Solar Optical Telescope on board of Hinode spacecraft [He *et al.* (2009)]. Tracing the transverse motions of solar spicules, relatively high-frequency (≤ 20 mHz) Alfvén waves were found to propagate upward with phase speeds between 50 - 150 km/s. Earlier, similar studies based on Hinode data reveal that much slower Alfvén waves (with velocities about 10-25 km/s) of lower frequencies (2-10 mHz) permeate the entire chromosphere, suggesting that those waves are strong enough to power the solar wind [De Pontieu *et al.* (2007)]. Alfvén waves with frequencies < 8 mHz and amplitudes of 2.6 km/s are also claimed to be identified in the lower solar atmosphere by comparison of simultaneous photospheric and chromospheric H_α images (see Figs. 1.15 and 1.16) of bright points taken by the Swedish Solar Telescope (SST) [Jess *et al.* (2009)]. Signatures of Alfvén waves in coronal holes were observed in

Mission Name	Launch year	End Year	Orbit	Periapsis (AU)	Apoapsis (AU)
PIONEER 8	1967	1996	Heliocentric near ecliptic plane	0.992	1.088
PIONEER 9	1968	1983	Heliocentric near ecliptic plane	0.754	0.99
HELIOS 1	1974	1981	heliocentric near ecliptic plane	0.309	0.985
HELIOS 2	1976	1986	heliocentric near ecliptic plane	0.29	0.983
ISEE 1-2	1977	1987	Highly elliptical geocentric	1.	1.
ISEE 3	1978	1983(*)	Highly elliptical geocentric	1.	1.
VOYAGER 1/2	1977	2007	Interstellar mission	1	–
GALILEO(**)	1989	2003	Jupiter Orbiter	1	5
ULYSSES	1990	2008	Solar Polar	2.3	5.4
WIND	1994	–	Ecliptic plane		
CASSINI(**)	1997	–	Saturn Orbiter	1	10
CLUSTER II (**)	2000	–	Elliptical geocentric	1	1
STEREO	2006	–	Ecliptic plane	0.9 (sat A)	1 (sat B)

Figure 1.11: Solar wind missions that carried on board a wave analyser [C. Briand (2009)].

the Fe XII and Fe XIII line width variations in images from EUV imaging spectrometer (EIS) on board of Hinode [Banerjee *et al.*(2009)] and low frequency ($< 5\text{mHz}$) propagating Alfvénic motions in the solar corona were revealed by coronagraphic polarimetry [Tomczyk *et al.*(2007)].

Alfvén waves in the solar wind close to the Sun have been detected “in situ” by Helios as shown on Figs. 1.12 and 1.13 [Bruno and Carbone (2005); Neugebauer *et al.* (1978)] and Alfvénic fluctuations appear both on small and large scales as illustrated by Fig. 1.14.

Other types of waves with somewhat higher frequency like Langmuir waves, IAWs and whistlers were also detected in the solar wind by different spacecrafts (Helios, Ulysses and Wind) as shown in the review by C. Briand in [Briand (2009)]. Furthermore, large-amplitude high-frequency ion-cyclotron waves were finally discovered from high-resolution Solar Terrestrial Observatory (STEREO) data in fast solar wind [Jian *et al.* (2009)]. Those left-hand circularly polarized waves have predominantly parallel propagation and exhibit nonlinear nature as their amplitude can exceed 10% of the external magnetic field strength. High-frequency nonlinear waves are prone to parametric decays. They can rather easily cascade and be absorbed, thus playing an important role for the solar wind plasma heating and acceleration, and for the generation and evolution of micro-turbulence as well. Hence they are of great interest for our analysis and their evolution will be extensively studied and presented in Chapters 3, 5, 6 and 7.

1.3 Motivation, scope and outline of the present work

The purpose of this work is to investigate the nonlinear damping of large-amplitude Alfvén-cyclotron waves as a possible mechanism to explain the differential heating and preferential acceleration of ions as observed in CHs and the fast solar wind. The process involves parametric decays which lead to the generation of ion-acoustic and Alfvén-cyclotron micro-turbulence, whose dissipation via wave-particle interactions is responsible for the deviation from thermodynamical equilibrium. Trapping in the large-amplitude daughter ion-acoustic waves (IAWs) and a consequent Landau damping results in parallel

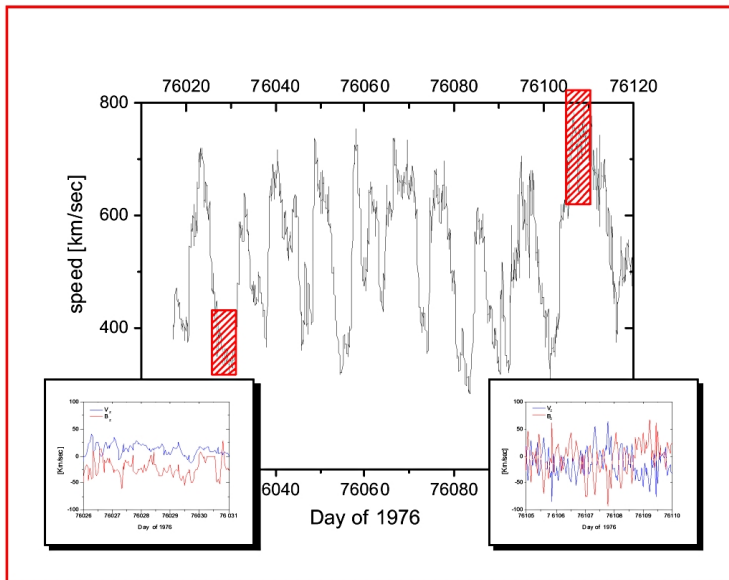


Figure 1.12: Measurements of the solar wind speed during the first Helios 2 flyby to the Sun in 1976. The two cut-offs below illustrate the magnetic field and velocity fluctuations for a chosen patch of slow and fast wind. The plots show a typical correlation for Alfvén waves [Bruno and Carbone (2005)].

heating, initiation of differential streaming between the different ion species and formation of ion beams. Pitch-angle scattering leads to perpendicular heating, which induces transverse anisotropies, thus producing non-thermal features in the particle velocity distribution functions as well. To treat those kinetic signatures we utilize a hybrid code and perform numerical analysis. We investigate low plasma β conditions with parallel wave propagation along homogeneous background magnetic field lines, typical for CHs and fast solar wind. We interpret the simulations in terms of parametric instabilities and compare the results with solar wind observations to infer information about the origin and cause for the deviations from thermal equilibrium.

Chapter 1 presented a general introduction to the nature and physical conditions in the solar corona and the solar wind. We described the plasma composition and discussed the role of the Coulomb collisions and the strength of the solar magnetic field for the relevant plasma processes, stressing on the importance of wave-particle interactions. We presented different observations of Alfvén waves and addressed their application for the plasma heating and acceleration.

In the following Chapter 2, we provide basic observational evidence for the common non-thermal features in CHs and the fast solar wind. Those can be seen both in the ion velocity distribution functions and in the temperature profiles, showing anisotropic heating, pref-

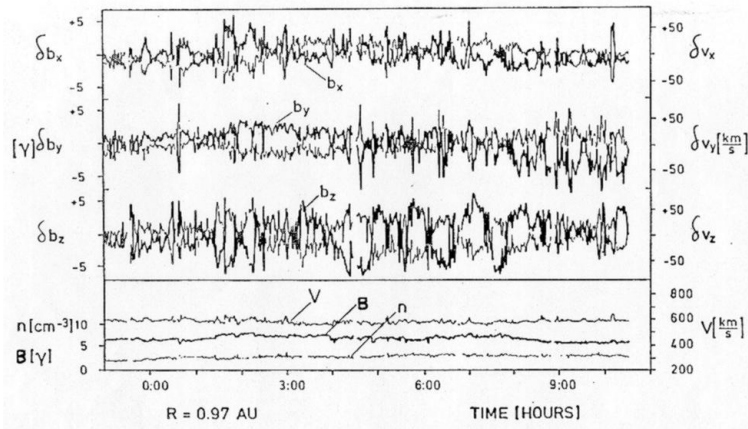


Figure 1.13: Alfvénic fluctuations in the solar wind seen by Helios 2 at 0.95AU [Neugebauer *et. al.* (1978)].

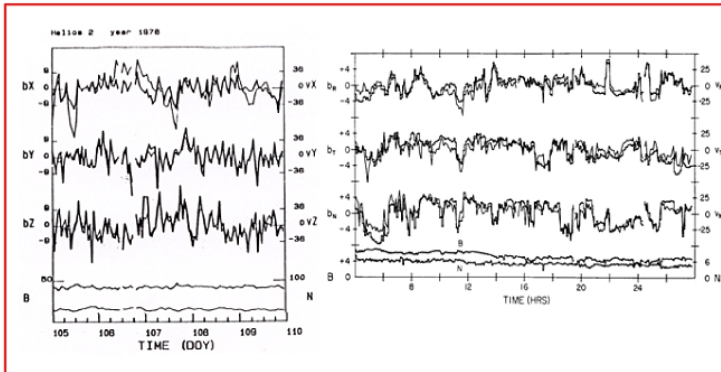


Figure 1.14: Typical Alfvénic correlations in the fast solar wind at about 0.3AU as seen by Helios 2. Both large (on the left) and small scales (to the right) Alfvénic fluctuations are present in the data [R. Bruno *et. al.* (1985); Belcher and Solodyna (1975)].

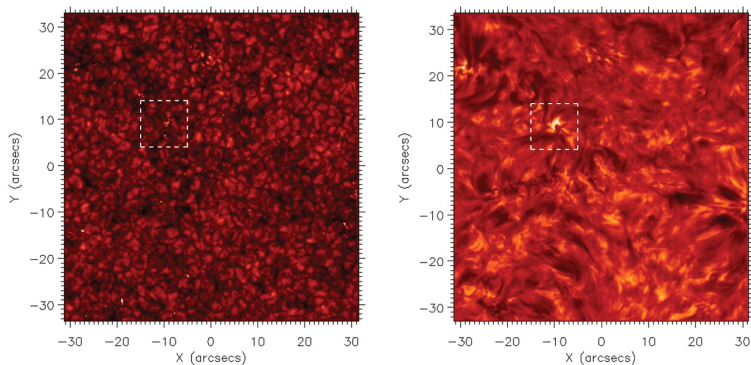


Figure 1.15: Indirect detection of Alfvén waves from photospheric and chromospheric spectroscopy [D. Jess *et al.* (2009)].

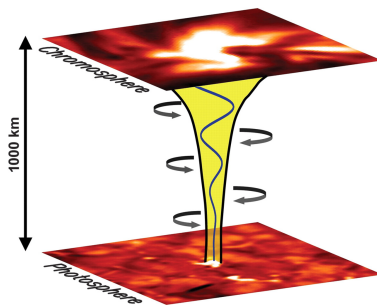


Figure 1.16: A sketch relating the photospheric motions with chromospheric features via parallel propagation of torsional Alfvén waves [Jess *et al.* (2009)]

entially for the heavy ions, with oxygen ions being much hotter than the protons, He ions (i.e. the α particles) sitting in between and the electrons being the coolest species. In situ profiles of the bulk velocities in the fast solar wind imply that minor ions are preferentially accelerated.

Chapter 3 provides analytical description of the different types of nonlinear couplings in a homogeneous magnetized multi-species plasma. It includes extensive analysis on parametric instabilities with a short discussion on Landau damping, cyclotron resonance and quasi-linear diffusion. It regards a derivation of the dispersion relations for the pump and the daughter waves, used for prediction and calculation of the instabilities wave-numbers range and growth rates. We generalize the scheme for analytical treatment of parametric decays and derive a complex dispersion relation, in the case when the plasma consists of fluid electrons, protons, α particles and oxygen VI ions.

Chapter 4 introduces the numerical methods involved in our analysis. It describes the na-

ture of the one-dimensional hybrid code, laying the basis for our simulation work, whose results are outlined in Chapters 5, 6 and 7. This Chapter includes a broad description of the physics behind the code, together with the numerical schemes, initial and boundary conditions. We enclose a short relation to the analytical parametric instability theory, used to analyse the results in the linear stage of the simulations. A comparison of the analytically predicted growth rate with the numerical data shows a good agreement between theory and simulations.

In Chapter 5 we consider the dissipation of nonlinear Alfvén-cyclotron waves and its impact on the ion velocity distribution functions in CHs and fast solar wind. We regard kinetic effects like particle trapping in the potential well of large-amplitude daughter ion-acoustic waves, as well as ion heating and acceleration by the consequent wave-particle interactions like Landau damping and pitch-angle scattering. The main part of our analysis is done for solar wind protons and α particles. Research on the behavior of heavy ions is included in Chapter 7.

Chapter 6 investigates the role of parametric decays of nonlinear Alfvén-cyclotron waves for the heating and acceleration of fast solar wind ions. A statistical simulation study on the kinetic behavior of protons and α particles is performed. We follow the evolution of the relative drifts and ion anisotropies and examine their regulation by parametric instabilities under different plasma β initial conditions.

Finally, the concluding remarks with an outlook for a future research take place in Chapter 8.

2 Plasma kinetics in the corona and the solar wind

As mentioned in the previous chapter, the solar wind has a rather complex and dynamic structure, which makes its modeling a challenge. In this chapter we shall present observational signatures for the non-thermal character of CHs and fast solar wind plasma. We will start with the ion velocity distribution functions, as derived from “in situ” measurements in the fast solar wind and continue with the temperature profiles, ion anisotropies and differential streaming. The aim of this PhD research is to combine all these features, relate them to the IAWs and Alfvén-cyclotron waves activities in a self-consistent manner and try to explain the observed plasma behavior. For this sake we need to have simultaneous information about the nature of the waves and the plasma properties. We already learned that both Alfvén-cyclotron and ion-acoustic are observed in the fast solar wind. Now let us say a few words about the plasma kinetics. Let us first shortly discuss the conditions in the solar corona and the slow solar wind. We have no information about the particles distributions in the solar corona, but regarding the collisional conditions derived from its density and temperature, we can deduce that the corona as a whole is weakly collisional and some deviations from thermal equilibrium can be expected even in dense coronal loops, though the collisions there might still be sufficient to maintain Maxwellian distributions as a whole. On the contrary, the dilute CHs are practically collisionless and the kinetic effects there play an important role. This reasoning is supported by spectroscopic modeling, suggesting preferential heating with strong anisotropies for the heavy ions (see Fig. 2.4). Similar to the corona, the slow solar wind is slightly collisional and the few collisions are enough to avoid strong anisotropies. Unlike the fast wind features, the slow wind has a less puzzling nature. The electrons (the lightest species) there are fastest, followed by the protons and the heavies as in an exospheric model scenario; the velocity distributions are almost isotropic and the proton and electron temperatures are comparable. The waves activity in the slow wind is different as well – it is more turbulent with large-scale structures and no prominent separate nonlinear waves. On the other hand, the conditions in the CHs and the fast solar wind are completely different. They are dominated by small-scale structures and exhibit large-amplitude waves.

Although the behavior of electrons, their heating, acceleration and non-thermal distributions have been extensively studied in the solar wind, in this chapter we will barely touch these light and abundant species, as their kinetics is explicitly excluded from both our analytical and numerical analysis. Instead, we will rather concentrate on the characteristics of protons and α particles with some input on the heavy ions as well.

The following sections provide observational evidence for strong non-thermal features

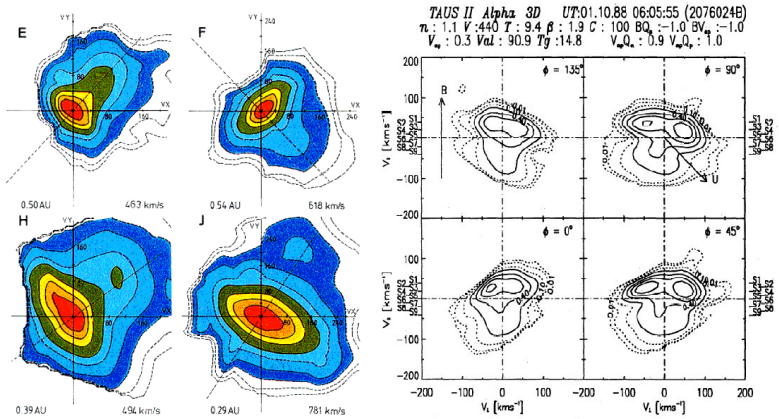


Figure 2.1: 2D contours of exemplary ion velocity distribution functions (VDFs) measured *in situ* in the fast solar wind. Left panel: Proton VDFs reconstructed from Helios 2 measurements at 4 different heliocentric distances: 0.29, 0.39, 0.5 and 0.54 AU [Marsch (2006)]. The straight lines show the direction of the magnetic field. Right panel: Non-gyrotropic VDFs for α particles based on 3D interpolation of the data collected at 1.3 AU by the Proton and Alpha Particle Spectrometer (TAUS) on board of Phobos 2 mission to Mars [Astudillo *et al.* (1996)]. The orientation of the magnetic field and the parallel velocity lay on the ordinate, whereas the transverse component of the velocity is shown along the horizontal axis.

in the ion distribution functions, shedding light on the ion temperature, anisotropy and velocity profiles in CHs and fast solar wind.

2.1 Common features, observed in the corona and the fast solar wind

As the fast solar wind is believed to arise from open field lines in CHs, it is not strange that the plasma in those two areas shows similar kinetic features. First we will present Helios 2 and Phobos 2 observations of the ion velocity distribution functions, then we will go on with reconstructed temperature profiles in the solar corona and close to the Sun, including various modeling of combined data from the Solar Heliospheric Observatory (SOHO), Ulysses, the Interplanetary Monitoring Platform (IMP), Helios and Voyager missions. We will review the “*in situ*” measurements of the kinetic temperature ratios as obtained by Wind and Ulysses spacecrafts and discuss the behavior of ion anisotropies versus different relative drifts and parallel plasma β regimes as revealed by the Advanced Composition Explorer (ACE) on board of Wind. We will end up with evidence for the preferential acceleration of α particles in the fast solar wind as discovered by Helios, Ulysses and Wind.

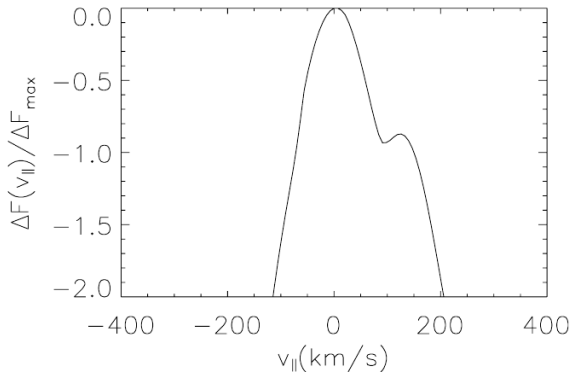


Figure 2.2: 1D reduced VDF as a function of the parallel velocity, obtained by integration of the 3D distributions along the vertical direction and normalized to its maximum value [Tu and Marsch (2004)]. The data was taken by Helios 2 at 0908:33 on day 70 in 1976. The horizontal axis shows the parallel velocity component in km/s. The little bump on the right side indicates the presence of a proton beam in parallel direction, similar to the ones seen on the left panel of Fig. 2.1.

2.1.1 Velocity distributions

Despite the many years of continuous space research on the the solar wind, there are not many measurements allowing unambiguous reconstruction of the ion velocity distribution functions. Early investigations on the proton distribution functions (left panel of Fig. 2.1) were presented by [Marsch *et al.* (1982a)], who made an intense study on the nature of protons and α particles in the solar wind near the Sun, based on Helios 2 data between 0.29 and 0.98 AU. Research on the α particles further out in the solar wind was done somewhat later by [Astudillo *et al.* (1995)], who presented evidence for nongyrotropic velocity distributions at 1.3 AU (see the right panel of Fig. 2.1). The data was collected by TAUS/Phobos 2 and belongs to an event with a spike in the ion density and temperature ratios, $n_\alpha/n_p = 0.03$, $T_\alpha/T_p = 12$, shortly after a discontinuity in the interplanetary magnetic field. The authors indicated a possible close relation between the non-gyrotropy of the distributions and the large temperature anisotropies (with $T_\perp > T_\parallel$) observed in this event.

Fig. 2.1 shows the nonthermal velocity distribution function in the fast solar wind. The left panel displays 2D contour plots of the 3D proton velocity distributions reconstructed from Helios 2 measurements of the fast solar wind at 0.29, 0.39, 0.50 and 0.54AU [Marsch (2006)]. The axes denote the components of the proton velocity, whereas the colour indicates the number density counts. The straight dashed line in the middle sets the direction of the interplanetary magnetic field. All proton distributions persistently show formation of beams (accelerated fraction of the protons with bulk speed $V_b \sim 1.5V_A$, traveling faster than the main “core” population, drawn in red and orange) along the magnetic field lines. In addition, the core of the distributions is prolonged in transverse direction, implying

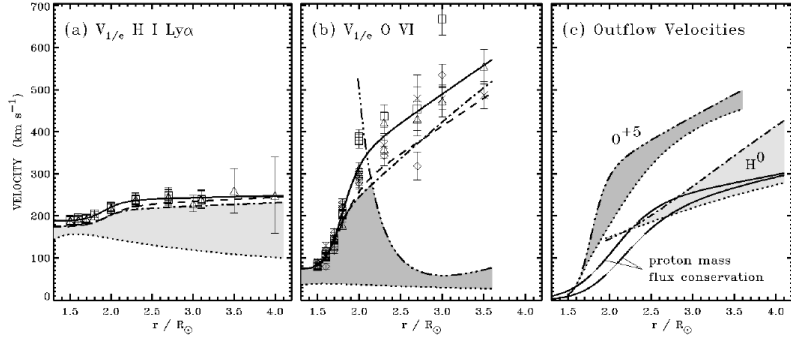


Figure 2.3: Constraints on the outflow velocities of neutral hydrogen and oxygen VI ions in the corona and the fast solar wind based on modeling of UVCS/SOHO data [Kohl *et al.* (1998)]. See the text for details.

temperature anisotropies of about $T_{\perp,c}/T_{\parallel,c} \in [2, 3]$. The right panel shows cuts of velocity distribution functions for α particles based on 3D data, taken by TAUS/Phobos 2 [Astudillo *et al.* (1996)]. The measurements were done with a high time resolution of 8 s. The cuts are given in the center of mass of the α particles. On this panel the velocity components were calculated with respect to the direction of the external magnetic field with a parallel propagation along the y-axis. The plots show 4 different cases, depending on the gyro-phase angle ϕ . Apart from the non-gyrotropic effects, we can see non-thermal features similar to those of the protons: α beams are formed along the magnetic field lines, whereas the anisotropic core is preferentially heated in transverse direction. The main population (the core) of the α particles sits in between the proton core and beam and the α particles drift velocity is $V_{\alpha p} = 0.3V_A$. The plasma parameters below the title show the number density N in cubiccentimeters, the bulk velocity V in km/s, the temperature T in kelvins, the gyration time T_g in seconds, the count rate of the channel with the highest measured count rate, C , the cosines of products of the magnetic field and the drift velocity, and the proton and alpha particle heat flux vectors. $V_{al} = 90,9$ is the Alfvén speed in km/s.

Fig. 2.2 shows an exemplary 1-D reduced VDF in the fast solar wind, $\Delta F(v_{\parallel})$, obtained by integration of the full three dimensional proton beam velocity distribution along the vertical direction for 2 fixed gyration angles $\phi = 0$ and $\phi = 180$. The distribution is centered at the null of the parallel velocity component v_k , given in km/s along the horizontal axis, with the proton beam being preferentially accelerated up to $V_b = 200$ km/s. We can see that the beam constitutes a substantial part of the protons (still less than 10%, though). The plasma parameters for this data set were $V = 680$ km/s, $V_A = 89$ km/s, $n_b/n_e = 0.08$, $V_d/V_A = 1.5$, with V_A being the local Alfvén speed, V – the solar wind bulk speed, n_b, n_e – the number densities of the proton beam and the electrons, and V_d – the drift speed between the proton core and beam.

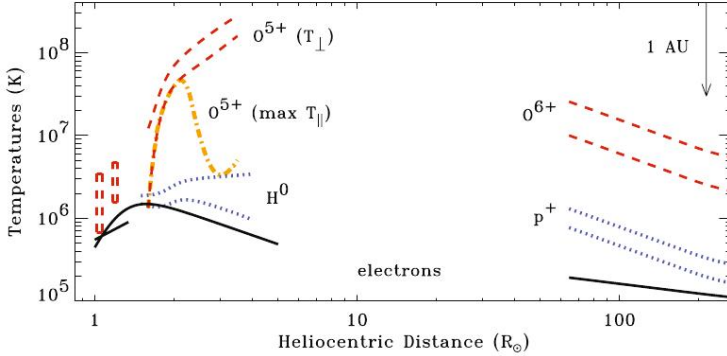


Figure 2.4: Radial dependence of the kinetic temperatures in polar CHs and high-speed wind at solar minimum, based on remote-sensing and in situ measurements [Kohl *et al.* (2006)]. Detailed description can be found in the text.

2.1.2 Temperature profiles and kinetic temperature ratios

There are different ways to deduce the ion temperature in the corona and the solar wind. One can use means of spectroscopy to sense the corona remotely looking at the Doppler dimming and pumping and at spectral lines thermal widths. One can measure *in situ* the kinetic temperatures from spacecrafts in the solar wind or use the freezing-in conditions of the detected ion species with different ionization state to extract information about the coronal temperature profiles and outflow speeds. Under the assumption that the ions are in collisional equilibrium with the surrounding electron gas one can derive a coronal temperature from the relative abundances of the ion species. Then measuring the charge states of the different species makes it possible to derive constraints on the electron temperature and the ion outflow velocities in the corona. This has been done for different elements in fast speed streams (at about $V = 750$ km/s) using data from the Solar Wind Ion Composition Spectrometer (SWICS) on board of Ulysses spacecraft [R. Schweingruber *et al.* (1998)]. The analysis shows preferential acceleration of the five-times-ionized oxygen ions O^{5+} , followed by C^{4+} , O^{6+} and He^{2+} . That is to say, that not simply the heavy ions are faster than the helium nuclei, but they seem to be ordered with respect to their charge to mass ratio, which has been used as an indicator that cyclotron effects might be important for the preferential acceleration of fast solar wind ions [Tu and Marsch (1997); Hollweg and Isenberg (2002); Marsch *et al.* (2003)]. Observational signatures for cyclotron effects in the solar wind have also been considered in [Cranmer *et al.* (1999)], [Dolla *et al.* (2004)] and [Gary *et al.* (2002)]. Another procedure based on Doppler dimming was applied to UVCS/SOHO data to reconstruct the O^{5+} and neutral hydrogen outflow velocities [Kohl *et al.* (1998)] as presented on Fig. 2.3. Panel (a) shows UVCS measurement of $V_{1/e}$ and the most probable speeds for H I Ly_α in CHs. $V_{1/e}$ is the $1/e$ half-width of the Gaussian coronal components of H I Ly_α lines over the poles, expressed in units of Doppler velocity: $V_{1/e} = c\Delta\lambda_{1/e}/\lambda_0$. The squares and triangles in the plot de-

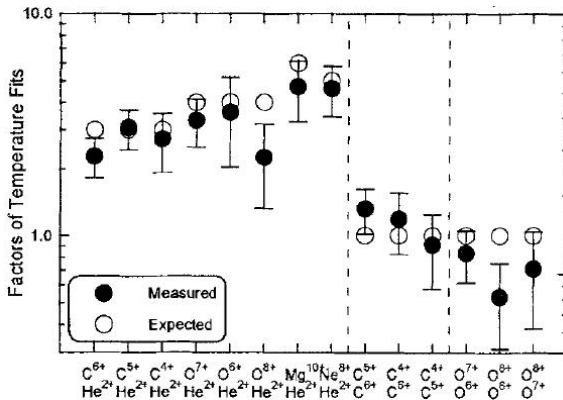


Figure 2.5: Heavy ions kinetic temperature ratios derived from Ulysses measurements in the solar wind [von Steiger *et al.* (1995)].

note the line widths from CHs at the north and south poles, respectively. The solid line gives a fit to the data, and the dotted lines represent the most probable speed of electrons w_e corresponding to thermal distributions at T_e . The dashed and dot-dashed lines give the most probable perpendicular speed of the neutral hydrogen for 2 different models: assuming thermal equilibrium with the electrons and assuming isotropic distributions. Panel (b) is similar to (a) (diamonds denoting measurements over the north pole, crosses – over the south), but for O VI λ 1032 with an overplotted empirical upper limit for the O⁵⁺ parallel speed (dash-triple-dotted line). Panel (c) shows empirical model of the O⁵⁺ and neutral hydrogen outflow velocity over the poles. The gray regions correspond to lower and upper limits on the parallel velocity with respect to the superradiantly diverging magnetic field lines (assuming anisotropic bi-Maxwellian distributions). The solid lines denote proton mass flux conservation for 2 solar wind expansion models. The result of this modeling is to show that remote sensing suggests preferential acceleration for the heavy ions in CHs as well. As visible on the next figure 2.4 spectroscopy analysis of coronal lines indicates that O⁵⁺ ions are not only faster than the neutral hydrogen H⁰, but they are hotter as well. Fig 2.4 shows the kinetic temperature profiles for different ion species in polar CHs and the fast solar wind at solar minimum [Kohl *et al.* (2006)]. Coronal curves are empirically derived from spectroscopy based on Doppler dimming and pumping, whereas the solar wind temperatures are constructed from an overview of Helios, IMP (Interplanetary Monitoring Platform), Ulysses, and Voyager particle data. The solid lines denote the electron temperatures, T_e , in polar CHs estimates from SUMER/SOHO (Solar Ultraviolet Measurements of Emitted Radiation) line widths and freezing-in models of in situ charge states measured by Ulysses. The dotted lines – neutral hydrogen and proton temperatures, and dashed lines mark the ionized oxygen temperatures. The paired curve sets in the extended corona, $1.5 < r < 10R_s$, refer to different empirical models derived from UVCS/SOHO emission line properties (statistical uncertainties are excluded). Dashed regions in the low corona at $r < 1.5R_s$ correspond to lower and upper limits on the O⁵⁺ ki-

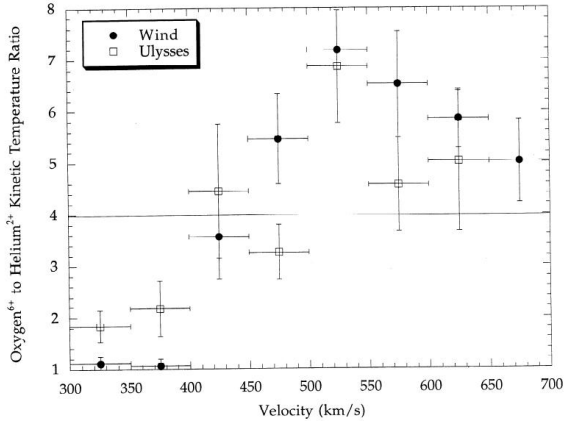


Figure 2.6: Heavy ions kinetic temperature ratios derived from Wind&Ulysses measurements in the solar wind [Cohen *et. al.* (1996)]

netic temperature, based on SUMER spectroscopy. The observed difference between the O^{5+} and proton temperatures suggests that there is preferential heating of heavy ions in coronal holes, and that the amount of heating leads to a temperature ratio which exceeds the oxygen-to-proton mass ratio $T_{O^{5+}}/T_p > m_{O^{5+}}/m_p = 16$, as observed also *in situ* in the solar wind (see Fig. 2.5 and Fig. 2.6). This is another signature that the heating process depends on the ion gyration frequencies (i.e. on their charge to mass ratios). The plot also indicates anisotropic heating for the O^{5+} ions. For more information on the anisotropic heating and preferential acceleration of O^{5+} ions see Ref. [Telloni *et. al.* (2007)].

Fig. 2.5 shows the kinetic temperature ratios for different heavy ion species as measured by Ulysses in the fast solar wind [von Steiger *et. al.* (1995)]. The graph shows many cases where the measured temperature ratios of the heavies (the black dots) exceed their charge-to-mass ratios (the empty circles). If the different ions in solar wind were to fly at the same thermal speeds, then we would expect the ion temperature ratios to be equal to their mass ratios. The fact that in many cases $T_i > (m_i/m_p)T_j$ in the past has been widely considered as an indirect signature for cyclotron heating, as, unlike the quasilinear diffusion, it is not restricted by an upper velocity limit, given by the phase speed of the more abundant low frequency waves. As we will see later however, the observed high temperature ratios can be explained also by a nonlinear diffusion of an initial coherent state, which consists of a large-amplitude Alfvén-cyclotron wave, restricting the motion of the ions. The electromagnetic field and the Lorentz force associated with the wave force the whole ion distribution to attain a bulk perpendicular drift. Once the nonlinear wave fades away, due to parametric decays for example, the particles start to diffuse and fill in the velocity space occupied by the initial perpendicular drift. This results in strong perpendicular heating of the particles, which is often combined with acceleration due to Landau damping of the acoustic fluctuations, born in the course of the parametric decay. Detailed explanation on parametric instabilities is presented in Chapter. 3.

speed (km/s)	days	$n_{4\text{He}}/n_{20\text{Ne}}$	$n_{16\text{O}}/n_{20\text{Ne}}$	$n_{4\text{He}}/n_{16\text{O}}$	$T_{20\text{Ne}}/T_{4\text{He}}$	$T_{16\text{O}}/T_{4\text{He}}$
315-350	10	397 ± 20	7.9 ± 0.7	50 ± 4	1.04 ± 0.11	1.11 ± 0.13
350-400	27	473 ± 21	7.4 ± 0.6	63 ± 5	0.99 ± 0.08	1.06 ± 0.13
400-450	27	609 ± 69	8.2 ± 1.4	74 ± 10	2.52 ± 0.69	3.56 ± 0.82
450-500	12	908 ± 176	11.2 ± 3.2	81 ± 8	1.71 ± 0.79	5.46 ± 0.88
500-550	8	637 ± 127	7.7 ± 1.6	83 ± 10	3.07 ± 1.48	7.18 ± 0.76
550-600	8	502 ± 167	6.5 ± 2.3	79 ± 10	10.6 ± 6.50	6.52 ± 1.02
600-650	19	536 ± 141	7.5 ± 2.0	72 ± 6	10.4 ± 5.77	5.85 ± 0.57
650-700	10	—	—	62 ± 7	—	5.02 ± 0.81

Figure 2.7: Density and temperature ratios for different speed solar wind. Data taken by Ulysses spacecraft after [Cohen *et al.* (1996)].

Fig. 2.6 shows the same result as Fig. 2.5, but based on data from both Ulysses and Wind spacecrafts. Additionally it allows us to analyse the dependence on the solar wind speed. The straight line corresponds to a mass ratio proportionality heating rate, $T_i = (m_i/m_j)T_j$, in the case when the ions move at the same thermal speed. The graph clearly shows the different kind of heating, operating in the slow and fast solar wind. The temperature ratio for only oxygen O^{6+} to helium He^{2+} ions is included. Similar information is presented on table 2.7, which shows the variation of ion abundances and kinetic temperature ratios, including Ne ions.

2.1.3 Ion anisotropies and differential streaming

In situ measurements show that the nature and the magnitude of the ion anisotropies in the solar wind strongly differs with the heliocentric distance, or equivalently with the value of plasma β . Thus in the fast solar wind close to the Sun (at Helios perihelion near 0.3 AU) the core of the protons shows larger temperature in the direction, perpendicular to the surrounding background solar magnetic field. For the range of Helios measurements between 0.3 and 0.54 AU [Marsch *et al.* (1982a)], the typical values of the proton core anisotropy are $(T_{\perp}/T_{\parallel})_p \in [2, 3]$. The same direction of the anisotropy is observed for the α particles, but at somewhat lower values $(T_{\perp}/T_{\parallel})_{\alpha} \in [1.2, 1.5]$, see [Marsch *et al.* (1982b); Marsch *et al.* (1991)]. Unlike the protons, though, no α beams were clearly resolved, which could also be a reason for the lower value of the temperature anisotropy for the α particles. Further out, in the solar wind close to the Earth (at 1 AU), the nature of the anisotropies changes and we can observe differential heating for both protons and α particles, predominantly in parallel direction as visible on Fig. 2.8 from [Kasper *et al.* (2008)]. Apart from the plasma β , the ion anisotropies depend also on the relative streaming between the ion species. The protons seem to possess parallel anisotropy at all values of the relative drift speed, whereas the heating of the α particles varies, with dominant perpendicular anisotropies $((T_{\perp}/T_{\parallel})_{\alpha} \sim 1.7)$ when the two species move at similar speeds and higher parallel temperatures for relative drifts in the range $V_{ap} \in [0.15, 0.85]V_A$. Fig. 2.8 shows the temperature anisotropies for protons and α particles and their dependence on the module of the relative drift velocity, ΔV_{ap} , normalized to the local Alfvén speed C_A . The research was done for fast solar wind ions near the Earth and the authors interpreted it as an enhanced parallel heating of α particles for a large range of relative drifts. As we will see later in chapter 6, though, this result can be well explained in terms of reduced perpendicular heating, that leads to the same values of the temperature anisotropies. We

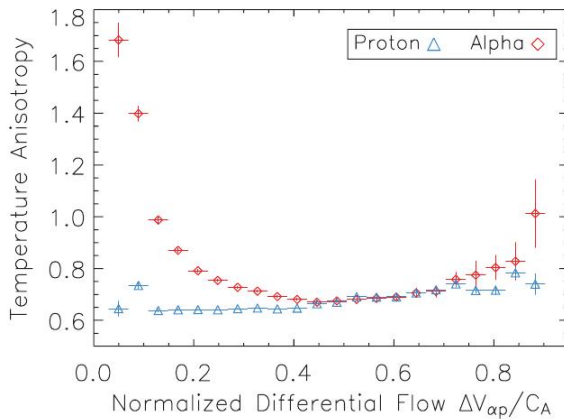


Figure 2.8: Temperature anisotropies versus normalized relative drift derived from ACE/Wind measurements around 1AU, courtesy of [Kasper *et. al.* (2008)].

should note that Fig. 2.8 was constructed without splitting the proton species into a core and beam (as done by [Marsch *et. al.* (1982a)]) and since proton beams are rather persistent in the fast solar wind, they might be the reason for the persistent parallel proton anisotropy, $T_{\perp p}/T_{\parallel p} < 1$, as detected by *Wind* spacecraft near the Earth.

There are many early detections of ion anisotropies and modeling of their variability with heliocentric distance, based on remote measurements in the corona, or taken in situ in the solar wind close to [Marsch *et. al.* (1982a); Marsch *et. al.* (1982b)] or further away from the Sun [Gary *et. al.* (2000a); Gary *et. al.* (2000b)]. Only recently though, in hope of enlightening the underlying physical processes, scientists started to analyse statistically the dependence of those anisotropies on other characteristic plasma parameters like waves activity, collisional age, relative drifts and thermal speeds [Bale *et. al.* (2009)]. Fig. 2.9 shows an example of the proton temperature anisotropies in the fast solar wind as a function of the parallel proton plasma β . The color code describes the wave activity (via the magnetic field intensity fluctuations) with purple meaning least and green meaning most active. The dotted lines give the theoretically calculated thresholds for 3 different linear kinetic instabilities. The mirror and the firehose instabilities are caused respectively by a high value of the perpendicular and parallel temperatures, and hence they regulate the temperature anisotropies both from above and below. Large part of the detected ions seem to be unstable with respect to the Alfvén-ion-cyclotron instability (AIC), whose threshold lays below that of the mirror instability. We should note, though, that in the presence of large-amplitude waves the linear instability analysis is no longer valid and one should rather study parametric instabilities or perform direct numerical simulations to investigate how nonlinear waves couple to the particles motion and affect such thresholds. Another ubiquitous feature observed in the solar wind, is the differential streaming. That is to say that the different ion species travel at different speeds. Like the temperature anisotropies, the differential streaming also depends on the type of solar wind and the

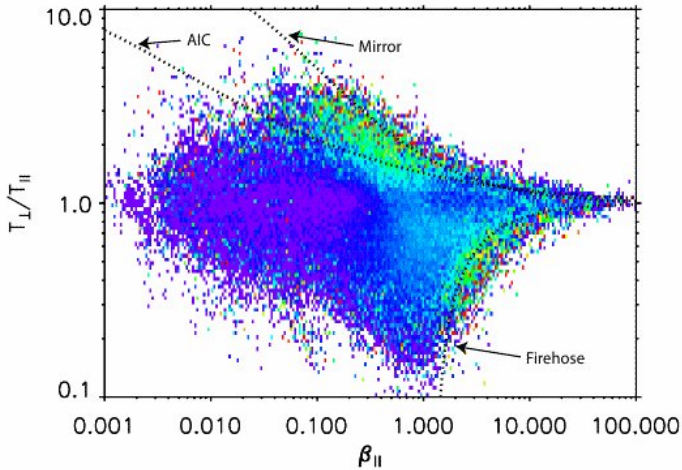


Figure 2.9: Dependence of the proton temperature anisotropy on the parallel proton plasma β , obtained from ACE/Wind measurements in the fast solar wind [Bale *et al.* (2009)]. Many of the protons appear above the threshold for Alfvén-ion-cyclotron instability (AIC) and the data seems to be constrained by the firehose and mirror instabilities.

heliocentric distance. In the fast solar wind at Helios perihelion near 0.3 AU the relative drift speed between protons and α particles is typically observed to be of the order of the local Alfvén speed, mostly with $V_{ap} < V_A$, and it generally decreases with increasing heliocentric distance as shown on Fig. 2.10 and Fig. 2.11. The proton core-beam stream at about $V_d \sim 1.5V_A$. The α core-beam drift is less known, as the α beam is more difficult to resolve (the α particles themselves are minor species, with a number density much less than that of the protons).

Fig. 2.10 shows the differential streaming of protons and α particles in the solar wind. The left panel demonstrates the dependence on heliocentric distance (in astronomical units) and the solar wind speed as observed by Helios 2 during its flyby to the Sun [Marsch (1982a); Marsch (1982b)]. The relative drift ΔV_{ap} is given in km/s and in fast streams it decreases as we go further away from the Sun. In the slow wind the streaming seems to be more stable on its way to the Earth. The right panel shows the variation of the relative drift V_{ap} with the solar wind travel time as measured by Ulysses further above 2.3 AU, and in a higher β region. The relative drift is a substantial fraction of the local Alfvén speed and also decreases as the wind flows further away from the Sun [Neugebauer *et al.* (1996)]. Fig. 2.11 presents the bulk velocities and differential streaming of protons and alphas along the interplanetary magnetic field for half a day in the fast solar wind near the Earth. Comparison of the relative drift direction with the orientation of the interplanetary magnetic field gives an estimate of how well the measurements have been performed. The

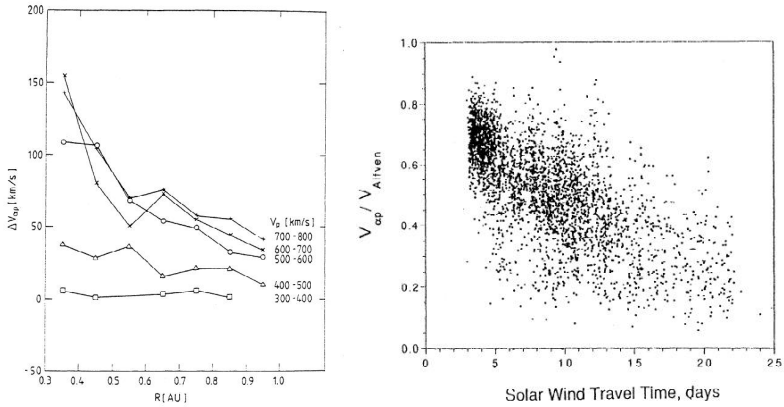


Figure 2.10: Left panel: Differential streaming between protons and α particles detected by Helios during its flyby to the Sun [Marsch (1982a); Marsch (1982b)]. The graph gives another perspective to the different behavior of ions in the slow and fast solar wind. Right panel: Relative drifts between protons and α particles, normalized to the local Alfvén speed, as measured much further away from the Sun by Ulysses [Neugebauer *et. al.* (1996)]. Results are plotted versus solar wind travel time, given in days.

magnetic field \mathbf{B} is measured by Magentic Field Investigation (MFI) fluxgate magnetometer on board of Wind. The first raw draws the proton and α particle bulk velocities in km/s, whereas the second raw plots their relative drift together with the local Alfvén speed. In most of the cases for this data set the differential streaming is lower than and at rare occasions it reaches the Alfvén speed V_A . The last two raws show the difference in the geocentric solar ecliptic (GSE) longitude ϕ and latitude θ between the magnetic field and the α -proton drift. As the ions are streaming along the interplanetary magnetic field lines, the comparison of the relative drift direction with the orientation of the interplanetary magnetic field gives an estimate of how well the measurements have been performed. Now that we have passed through the observations, in the next chapter we will present an analytical description of nonlinear couplings in a multi-species plasma in the presence of large-amplitude waves. Later on, in Chapters 5 and 6, we will use those theoretical tools to try to explain the above-introduced non-thermal features in CHs and fast solar wind.

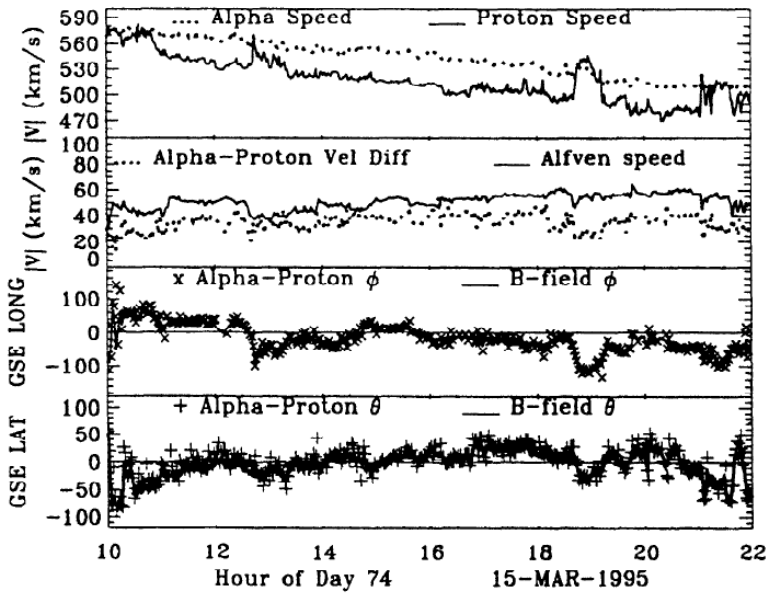


Figure 2.11: Relative drifts between protons and α particles and differential streaming versus the local Alfvén speed, as detected by Wind in the fast solar wind near the Earth [Steinberg *et. al.* (1996)]. Results are plotted versus solar wind travel time, given in hours.

3 Analytical description of nonlinear couplings in multi-species plasmas

In this chapter we will discuss the different types of nonlinear processes that naturally occur in collisionless magnetized non-relativistic plasmas. First we will consider nonlinear wave-wave couplings, described in terms of parametric instabilities of large-amplitude Alfvén-cyclotron waves. Then we will turn to basic wave-particle interactions like Landau damping and cyclotron resonance, and quasi-linear diffusion of the ion distribution function in velocity space. While the parametric decays can be also described in magneto-fluid or multi-fluid terms, wave-particle interactions are pure kinetic processes, that require knowledge of the particle velocity distribution functions. Evidence for all those processes can be found in the non-thermal ion velocity distributions present in the solar corona and the fast solar wind.

3.1 Parametric instabilities

In this subsection we derive the dispersion relation for parametric instabilities of “pump” Alfvén-cyclotron waves with frequencies lower than the lowest ion-cyclotron (associated with the heaviest ion species present in the system), far below the electron gyration frequency and still ways above the pure MHD low-frequency Alfvén modes. This provides us with information about the excitation and growth rates of secondary (so called “daughter”) waves via three-wave processes, governed by the selection rules:

$$\omega_0 = \omega \pm \omega_s, \quad k_0 = k \pm k_s. \tag{3.1}$$

From quantum mechanical point of view those rules correspond to the energy and momentum conservation laws in the photon-plasmon scattering diagrams. In practice they restrict the space of all possible wave excitations at a given time. In other words it tells us what kind of ion-acoustic waves (IAWs, characterized by ω_s and k_s) might grow out of the thermal noise in the system and how they are related to the excitation of “daughter” electromagnetic waves (ω , k), when a given pump, or also called a “mother” wave, (ω_0 , k_0) is provided. Parametric instabilities describe the wave-wave coupling between a finite-amplitude EM pump wave and the acoustic fluctuations caused by the thermal motion of the plasma. As a result, we end up with a set of daughter EM waves, characterized by different frequencies and wavenumbers as compared to the initial pump. Depending on the kind of daughter waves involved, their wavelengths and direction of propagation, we can distinguish 3 types of parametric instabilities, which are described in the subsection below. They depend on the initial state of the plasma and the different instabilities

naturally interchange in the course of evolution, generating both acoustic and EM micro-turbulence. For a comprehensive review on parametric instabilities of monochromatic Alfvén-cyclotron waves see, for example, [Hollweg (1994)] or [Araneda *et. al.* (2007)]. We should note that the parametric instabilities theory itself involves nonlinear wave-wave couplings and allows for a large amplitude pump. However, this theory is linear with respect to the generated daughter EM and IA waves and if we are to compare with results from numerical simulations, for instance, we can use it for predictions and interpretation of the data only for the linear stage of the simulations, before the daughter transverse wave amplitude becomes a substantial part of the steady external magnetic field. Such a comparison between theory and simulations will be presented at the end of the next Chapter 4.

In what follows we are going to present the different types of parametric instabilities and derive their dispersion relation for several different cases, depending on the ion composition of the plasma considered.

3.1.1 Nonlinear nature and different types

In our analysis we investigate the parametric instabilities of parallel-propagating large-amplitude circularly-polarized Alfvén-cyclotron waves. Even though they constitute an exact nonlinear solution of both MHD [Baumjohann and Treumann (1996)] and collisionless kinetic plasmas [Sonnerup and Su (1967)], those waves are well-known to couple to the acoustic fluctuations, produced by the thermal motion of the particles and therefore be parametrically unstable [Derby (1978); Goldstein (1978)]. Investigation of parametric instabilities using a multi-fluid approach was done by [Hollweg, Esser and Jayanti (1993)], who analyzed the nature of parametric instabilities when a differential streaming of α particles is present. Studies on parametric decays for a plasma consisting of electrons, protons and non-drifting α particles have been conducted in the framework of plasma kinetics [Kauffmann and Araneda (2008)], to further examine the kinetic effects like collisionless Landau damping on the dispersion relation.

One can encounter 3 different types of parallel-propagating parametric instabilities, namely **decay**, **modulational** and **beat**. In terms of an inviscid multi-fluid including Hall effect those types were extensively described by [Hollweg *et. al.* (1994)]. Earlier a gyrokinetic approach was used by [Inhester (1990)] and more recently a hybrid (fluid-kinetic) description was introduced by [Araneda (1998); Araneda *et. al.* (2007)]. Finite ion temperature effects are also studied in [Nariyuki and Hada (2007)], incoherent wave structure in a finite ion plasma β was considered in [Nariyuki and Hada (2007)] and parametric instabilities in the presence of proton beams was investigated by [Araneda *et. al.* (2008); Nariyuki and Hada (2009)]. Kinetic effects in the presence of 2 ion species (protons and α particles) were taken into account in [Araneda *et. al.* (2009); Maneva *et. al.* (2009)]. Circularly-polarized Alfvén waves were first found to be parametrically unstable by [Galeev and Oraevskii (1963)] and [Sagdeev and Galeev (1969)], who investigated the decay instability within the framework of an ideal MHD. The **decay** instability results from a nonlinear interaction between forward propagating (with respect to the direction of propagation of the parent wave) ion acoustic waves (IAW) with backward propagating daughter Alfvén waves. Or we can say that the parent (i.e. the pump) Alfvén wave “decays” into a pair of an IAW and another daughter Alfvén wave. Within the fluid approach for a left-hand

polarized Alfvén-cyclotron pump wave this instability exist in the range $0 < c_s^2/V_A^2 < 1$, where c_s is the sound speed and V_A is the Alfvén speed, which we will define later. When, for a left-hand polarized pump, the upper ratio exceeds unity, $c_s^2/V_A^2 > 1$, the decay process is replaced by the beat instability, which involves a nonlinear interaction between one forward propagating and one backward propagating daughter Alfvén wave, each coupled respectively to a corresponding IAW, according to the selection rules Eq. (3.1). The **beat** instability then occurs when there is an interaction between a sound wave and the pump, during which lower frequency (with respect to the initial pump) forward propagating and higher frequency backward propagating (with respect to the homogeneous background magnetic field orientation) waves are formed. Since forward propagating IAW with larger wave numbers than those of the parent Alfvén waves are excited by both decay and beat, in the kinetic regime those instabilities behave practically identical, so we will call them “decay-like instabilities”. The last type, the **modulational** instability, involves interaction between forward propagating IAWs and two forward propagating Alfvén waves (sidebands), with a higher and lower frequency with respect to the initial pump. It is characterized by daughter waves with smaller wave-numbers in comparison to the pump $k < k_0$. For a left-hand polarized pump wave the modulational instability appears in the same low β regimes, $c_s^2/V_A^2 < 1$, where the decay instability operates. Our simulation analysis is basically bound to low β regimes, thus in the course of evolution we encounter mainly modulational and decay instabilities. This issue will be discussed again in the following chapters.

3.1.2 Pump wave dispersion relation – setting up the ground state

There are several different ways that one can arrive at the same pump wave dispersion relation for a parallel propagation in a homogeneous quasi-neutral plasma with constant background magnetic field $B_z = \text{const}$ and relative drifts between the different species. One can derive it as an exact nonlinear kinetic solution of a hot collisionless homogeneous plasma (as done by [Sonnerup and Su (1967)]), for more details refer to sec. 4.2 of the next chapter 4). One can obtain it from the cold plasma perturbation analysis [Galeev and Sudan (1989); Davidson (1972)] and it comes as a direct result in a multi-fluid dynamics description as showed by [Goldstein (1978); Hollweg (1994)]. In any of those cases to derive the dispersion relation one needs to supplement either the moments of the Vlasov equation (in the kinetic description)

$$\frac{\partial f_s}{\partial t} + \mathbf{v} \cdot \frac{\partial f_s}{\partial \mathbf{x}} + \frac{q_s}{m_s} \left(\mathbf{E} + \frac{\mathbf{v} \times \mathbf{B}}{c} \right) \frac{\partial f_s}{\partial \mathbf{v}} = 0, \quad (3.2)$$

or the momentum (in case of a MHD fluid)

$$\frac{\partial \mathbf{V}_s}{\partial t} + \mathbf{V}_s \cdot \nabla \mathbf{V}_s - \frac{q_s}{m_s} (\mathbf{E} + \mathbf{V}_s \times \mathbf{B}) + \frac{\nabla P_s}{m_s n_s} = 0 \quad (3.3)$$

and continuity equations

$$\frac{\partial n_s}{\partial t} + \nabla \cdot (n_s \mathbf{V}_s) = 0 \quad (3.4)$$

with the Maxwell equations for the electromagnetic fields. For a parallel propagation in a 1D simplified geometry, the transverse and longitudinal wave motions are decoupled.

Then the pressure gradient force ∇P_s has only a parallel component and does not influence the characteristic wave equations. For a non-relativistic and quasi-neutral plasma for low-frequency waves within the ion-cyclotron domain, the displacement current in Ampère's law can be neglected and there are no density and electric field fluctuations along the background magnetic field.

For a parallel propagating monochromatic Alfvén-cyclotron wave in a charge and current-conserving multi-species plasma the dispersion relation reads

$$k_0^2 - \frac{\omega_0^2}{c^2} + \frac{1}{c^2} \sum_s \omega_{ps}^2 \frac{\omega_0 - k_0 V_s}{\omega_0 - k_0 V_s - \Omega_s} = 0, \quad (3.5)$$

where for low-frequency waves (ion-cyclotron waves regime) the second term can be neglected. The notations are the same as given in Appendix A, namely $\omega_{ps}^2 = n_s q_s^2 / \epsilon_0 m_s$ is the plasma frequency for the s species, $\Omega_s = q_s B_z / m_s$ is the cyclotron frequency and V_s is the parallel drift speed.

In both kinetic and multi-fluid approaches the entire plasma in perpendicular direction is obliged to follow the electromagnetic field of the wave with a transverse bulk velocity, given by

$$V_{\perp,s} = \alpha_s B_{\perp}, \quad \alpha_s = -\frac{(\omega_0/k_0 - V_s)}{(1 - \omega_0/\Omega_s + k_0 V_s/\Omega_s) B_z}. \quad (3.6)$$

3.1.3 Ground state perturbations – instability analysis

Now let us take this solution, which self-consistently couples the monochromatic pump wave of an arbitrary amplitude to the different particle species and use it as a ground state for a further perturbation analysis. For that sake we will investigate the effect of small density fluctuations δn_s on the global stability of the coupled wave-particles system. This leads to the parametric instabilities analysis, describing daughter waves generation via wave-wave interactions.

3.1.3.1 General derivation – Equation of motion

As a starting point we will perform a survey within the multi-fluid framework. Later on, we shall extend previous works on the kinetic effects, related to Landau damping in parallel direction, and allow for arbitrary drift speeds between the different ion species. Finally, we will discuss the consequences on the stability conditions.

Together with the density and pressure fluctuations we assume slight deviations from the steady parallel and perpendicular bulk speeds, the electric and the magnetic fields as well

$$n_s = n_{0s} + \delta n_s, \quad V_s = V_{0s} + \delta V_{zs}, \quad V_{\perp} = V_{\perp 0} + \delta V_{\perp}, \quad (3.7)$$

$$P_s = p_{0s} + \delta p_s, \quad E_{\perp} = E_{\perp 0} + \delta E_{\perp}, \quad B_{\perp} = B_{\perp 0} + \delta B_{\perp}, \quad (3.8)$$

where the zeroth quantities belong to the ground state. As we consider parallel propagation of transverse waves, the parallel magnetic field stays unchanged, but the fluctuations introduce an additional electric field in parallel direction E_z , which is to be taken into account. Assuming a plane wave form for the fluctuations (in particular $\delta V_{sz} = u_s \exp(ikz -$

$i\omega t$) and linearizing the continuity equation with respect to the small-amplitude wave for the density fluctuations we obtain

$$\delta n_s = n_{0s} \Re \left[\frac{k u_s \exp(ikz - i\omega t)}{\omega - kV_{0s}} \right]. \quad (3.9)$$

To incorporate collisionless damping effects we can perform an analysis, using a kinetic description in parallel direction. Let us consider as a zeroth order a one-dimensional plasma composed of massless electrons and different ion species (indicated by s) in equilibrium with a circularly polarized electromagnetic wave. The corresponding distribution function has the form

$$F(z, \mathbf{v}, t) = n_{0s} \delta(\mathbf{v}_\perp - \mathbf{V}_\perp) f_s(z, v_z, t), \quad (3.10)$$

where the perpendicular velocity is given by Eq. (3.6). We assume small deviations

$$f_s(z, v_z, t) = f_{0s}(v_z) + \delta f_s(z, v_z, t) \quad (3.11)$$

from an equilibrium velocity distribution function, chosen to represent a drifting Maxwellian

$$f_{0s}(v_z) = \frac{1}{\sqrt{\pi} v_{\text{th},s}} \exp \left(-\frac{(v_z - V_{0s})^2}{v_{\text{th},s}^2} \right), \quad (3.12)$$

where $v_{\text{th},s} = \sqrt{2k_B T_{\parallel,s}/m_s}$ is the thermal speed related to the parallel temperature $T_{\parallel,s}$. If we consider a wave form for the spatial and temporal parts of the fluctuations of the distribution function $f(z, v_z, t) \sim \exp(ikz - i\omega t)$, neglecting second order terms we can apply the Fourier-Laplace method and linearize the Vlasov equation. If we then take the first moment of the perturbed Vlasov equation and integrate over the velocity space, we obtain the kinetic expression for the density fluctuations

$$\delta n_s = n_{0s} u_s \omega'_s \left[1 - \frac{k^2 c_s^2}{\omega_s'^2} \right] \frac{Z'(\xi'_s)}{k v_{\text{th},s}^2}, \quad (3.13)$$

where $c_s^2 = p_s/n_s m_s$ is the sound speed, $\omega'_s = \omega - kV_{0s}$ is the Doppler shifted frequency and $Z'(\xi'_s)$ is the first derivative of the plasma dispersion function $Z_s(\xi'_s)$

$$Z'_s(\xi'_s) = -2[1 + \xi'_s Z_s(\xi'_s)], \quad Z_s(\xi'_s) \equiv \frac{1}{\sqrt{\pi}} \int_{-\infty}^{\infty} \frac{e^{-x^2}}{x - \xi'_s} dx, \quad \xi'_s \equiv \frac{\omega'_s}{k v_{\text{th},s}}. \quad (3.14)$$

Further on, assuming a polytropic equation of state $\delta p_s/p_{0s} = \gamma_s \delta n_s/n_{0s}$, we find a kinetic expression for the polytropic index

$$\gamma_{s,\text{kin}} = 2 \left[\xi_s'^2 - \frac{1}{Z'(\xi_s')} \right]. \quad (3.15)$$

Thus, under the approximations mentioned above, the transition from multi-fluid approach to kinetics can be achieved simply by substituting the fluid plasma β

$$\beta_s \equiv \frac{p_s}{p_B} = \frac{n_s m_s v_{\text{th},s}^2}{n_e m_p V_A^2} \quad (3.16)$$

with its kinetic equivalent

$$\beta'_s \equiv \frac{\gamma_{s,\text{kin}} v_{\text{th},s}^2}{2V_A^2} = \xi_s'^2 - \frac{\beta_s}{Z(\xi_s')}, \quad (3.17)$$

where p_s and p_B stand for the plasma and the magnetic pressure of the s species and the mass and density normalization coefficients come from the definition of the Alfvén speed $V_A \equiv B_z / \sqrt{4\pi n_e m_p}$. Such an analysis was performed earlier by [Kauffmann and Araneda (2008)], who investigated the effects of Landau damping on the parametric instabilities dispersion relation for the case of a plasma, consisting of massless fluid electrons, warm protons and non-drifting α particles.

In analogy to the way we derived the density fluctuations from the continuity equation, we can perform Fourier transform and linearize the momentum equation (or, in the kinetic regime, take the first moment in Fourier space of the linearized Vlasov equation for a drifting Maxwellian background distribution) to obtain an expression for the velocity fluctuations

$$\omega'_s \left[1 - \frac{k^2 v_s^2}{(\omega'_s)^2} \right] u_s = \frac{q_s}{m_s} [i\epsilon + B(\alpha_s b_+ - \alpha_s b_-^* + v_{-s}^* - v_{+s})], \quad (3.18)$$

where the following notations have been used

$$\begin{aligned} \delta n_s &= \frac{1}{2} n_{0s} \left[\frac{u_s k}{\omega'_s} e^{i\Phi} + \frac{u_s^* k^*}{\omega'_s} e^{-i\Phi^*} \right], & \Phi &= kz - \omega t, & \Phi_0 &= k_0 z - \omega_0 t, & (3.19) \\ \delta B_{\perp} &= \frac{1}{2} (b_+ e^{i\Phi_+} + b_- e^{i\Phi_-}), & \delta E_{\perp} &= \frac{1}{2} (\epsilon_+ e^{i\Phi_+} + \epsilon_- e^{i\Phi_-}), & \Phi_{\pm} &= \Phi_0 + \Phi, \\ \delta v_{\perp} &= \frac{1}{2} (v_+ e^{i\Phi_+} + v_- e^{i\Phi_-}), & \delta E_z &= \frac{1}{2} (\epsilon e^{i\Phi} + \epsilon^* e^{-i\Phi^*}), & \Phi_- &= \Phi_0 - \Phi^*, \\ \delta v_z &= \frac{1}{2} (u_s e^{i\Phi} + u_s^* e^{-i\Phi^*}), & B_{\perp 0} &= B_x + iB_y = B e^{i\Phi_0}, & E_{\perp 0} &= -\frac{i\omega_0}{k_0 c} B_{\perp 0}. \end{aligned}$$

Next we apply charge and current conservation to eliminate the electron density and velocity fluctuations. Since we treat the electrons as a massless isothermal ideal fluid, their contribution to the pressure and density fluctuations depends on the temperature and their polytropic index as

$$\lim_{m_e \rightarrow 0} m_e v_{se}^2 = \lim_{m_e \rightarrow 0} m_e \frac{\gamma_e p_{0e}}{\rho_{0e}} = \gamma_e k_B T_e. \quad (3.20)$$

We use the massless assumption for the electrons to eliminate the electric field ϵ in Eq. (3.18) and obtain

$$\begin{aligned} i\epsilon &= \frac{Bb^*}{B_z} \left(\frac{\omega^*}{k^*} - \frac{\omega_0}{k_0} \right) - \frac{Bb_+}{B_z} \left(\frac{\omega_+}{k_+} - \frac{\omega_0}{k_0} \right) \\ &+ \frac{\gamma_e k_B T_e k^2}{e} \sum_{i \neq e} (1 + Q_i \eta_i)^{-1} \left(\frac{u_p}{\omega - kV_{0p}} + \frac{Q_i \eta_i u_i}{\omega - kV_{0i}} \right). \end{aligned} \quad (3.21)$$

Now we are ready to substitute this expression back in Eq. (3.18) and derive the momentum equation for the velocity fluctuations. To do so, however, it is convenient to work with dimensionless units. In order to facilitate the computations and for the sake of direct

comparison with the numerical simulations (see Sec. 4.2 and 4.3 of the next Chapter 4) we introduce dimensionless variables, using the proton gyrofrequency Ω_p and the Alfvén speed V_A , to normalize our units

$$X'_{0s} \equiv X_0 - Y_0 U_s, \quad X_0 \equiv \frac{\omega_0}{\Omega_p}, \quad Y_0 \equiv \frac{k_0 V_A}{\Omega_p}, \quad (3.22)$$

$$\Psi'_{0s} \equiv 1 - R_s X'_{0s}, \quad R_s \equiv \frac{\Omega_p}{\Omega_s}, \quad U_s \equiv \frac{V_{0s}}{V_A}. \quad (3.23)$$

We can also express the mass ratio in terms of the charge Q_s and cyclotron frequencies R_s ratios and use normalized densities

$$\frac{m_s}{m_p} = Q_s R_s, \quad Q_s \equiv \frac{q_s}{e}, \quad \eta_s \equiv n_s/n_p \quad (3.24)$$

to rewrite the pump wave dispersion relation Eq. (4.24) in the dimensionless form

$$Y_0^2 = \eta_e^{-1} \sum_{s \neq e} \eta_s \frac{Q_s R_s X'_{0s}}{\Psi'_{0s}}. \quad (3.25)$$

Similarly we can introduce dimensionless units related to the daughter fluctuations

$$X'_s \equiv X - Y U_s, \quad \Psi'_{\pm s} = 1 - R_s X'_{\pm s}, \quad X'_{\pm s} = X'_{0s} \pm X'_s, \quad r_s = \Psi'_{0s} \Psi'_{+s} \Psi'_{-s}. \quad (3.26)$$

Then plugging the upper expression for the electric field Eq. (3.21) into the momentum equation Eq. (3.18), the equation of motion for the velocity fluctuations finally reads

$$D_s \frac{u_s}{V_A} = \frac{B_{+s} b_+ + B_{-s} b_-}{B} - C_s, \quad (3.27)$$

where the multipliers in front of the magnetic fields are

$$B_{\pm s} \equiv \pm \frac{A X'_s \Psi'_{\mp s}}{R_s Y_0 Y_{\pm}} \left[(X'_{0s} - X_0 \Psi'_{0s}) \Psi'_{\pm s} Y_{\pm} + (X_{\pm} \Psi'_{\pm s} - X'_{\pm s}) \Psi'_{0s} Y_0 \right]. \quad (3.28)$$

We introduced also the coefficients

$$D_s \equiv r_s \beta_e Y^2 \frac{\eta_s Q_s}{\eta_e R_s} - X_s'^2 \Delta_s \quad (3.29)$$

and

$$C_s \equiv \frac{\beta_e r_s X'_s Y^2}{\eta_e R_s V_A} \sum_{j \neq e, s} \frac{\eta_j Q_j \mu_j}{X'_j}, \quad (3.30)$$

together with the auxiliary variable

$$\Delta_s \equiv A + r_s \left(1 - \beta_s' \frac{Y^2}{X_s'^2} \right), \quad A \equiv \frac{B^2}{B_z^2}. \quad (3.31)$$

In the presence of relative drifts, the last term C_s in the momentum equation Eq. (3.27) couples the velocity fluctuations of the different species u_s and makes them dependent on each other.

3.1.3.2 General derivation – Maxwell's equations

In order to close the system for the velocity fluctuations and proceed with the parametric instabilities dispersion relation we need to describe the fields fluctuations, provided by the Maxwell equations. The Ampère law in our simple 1D geometry reads

$$i\partial_z B_\perp = 4\pi j_\perp + \partial_{ct} E_\perp. \quad (3.32)$$

We take into account that $B_\perp = B_{\perp 0} + \delta B_\perp$ and $j_\perp = j_{\perp 0} + \delta j_\perp$, apply the definition of the currents: $j = \sum_s n_s q_s V_s$ and remember that $n_s = n_{0s} + \delta n_s$. Further we linearize with respect to the small-amplitude fluctuations (i.e. neglect the $\delta n_s \delta v_\perp$ term) and take into account that the Maxwell's equations should be valid both for the perturbed and the unperturbed quantities. The Ampère law for the perturbations then yields

$$i\partial_z \delta B_\perp = \sum_s 4\pi q_s (n_{0s} \delta v_\perp + \delta n_s v_{\perp 0}) + \partial_{ct} \delta E_\perp. \quad (3.33)$$

In terms of the electromagnetic fluctuations the Faraday law takes the form

$$\varepsilon_\pm = -i \frac{\omega_\pm b_\pm}{k_\pm c}. \quad (3.34)$$

Next we can apply the definitions for the density fluctuations, the electric and magnetic fields Eq. (3.19) and separate the independent exponents. As we are interested in a hybrid approach, where the electrons only act as a neutralizing background fluid, we invoke again the charge and current conservation laws to eliminate their contribution

$$\omega_{pe}^2 R_e X'_e = - \sum_{s \neq e} \omega_{ps}^2 R_s X'_s. \quad (3.35)$$

We also assume parallel propagation of low-frequency waves (with frequencies much lower than the electron gyration Ω_e) in a dilute plasma, which fulfils

$$\Psi'_{+e} = 1 - R_s X'_{+e} = 1 - \frac{\omega_0 + \omega'_e}{\Omega_e} \approx 1. \quad (3.36)$$

Then we substitute the explicit form of the density fluctuations Eq. (3.13) and combine the Maxwell equations to obtain the missing relation between the magnetic field and the velocity fluctuations. For the “positive” and “negative” modes we obtain

$$L_{+s} b_+ + \sum_{s \neq e} \frac{\omega_{ps}^2 V_A^2}{\Omega_s^2 c^2} \frac{u_s}{V_A} B R_{+s} = 0, \quad (3.37)$$

$$L_{-s} b_-^* + \sum_{s \neq e} \frac{\omega_{ps}^2 V_A^2}{\Omega_s^2 c^2} \frac{u_s}{V_A} B R_{-s} = 0, \quad (3.38)$$

where the coefficients are given by

$$L_{\pm s} \equiv Y_\pm^2 - \frac{X_\pm^2 V_A^2}{c^2} - \sum_{s \neq e} \frac{\omega_{ps}^2 V_A^2}{\Omega_s^2 c^2} \frac{X'_{\pm s}}{\Psi'_{\pm s}} \quad (3.39)$$

and

$$R_{\pm s} \equiv \frac{Y_{\pm}}{2\Psi'_{0s}} \left(X'_{0s} - \frac{X'^2_{0s}}{X'_s} \frac{Y}{Y_0} + \frac{X'_{\pm s}}{\Psi'_{\pm s}} \right). \quad (3.40)$$

We should note that the second term in Eq. (3.39) $X'^2_{\pm} V_A^2 / c^2$ comes from the displacement current. Therefore in case of non-relativistic plasmas, as typical for coronal holes and fast solar wind, its influence is insignificant and it can be neglected. Furthermore, it is useful to express the ratio of the plasma to cyclotron frequencies in terms of the dimensionless variables

$$\frac{\omega_{ps}^2}{\Omega_s^2} \frac{V_A^2}{c^2} = \frac{n_{0s}}{n_{0e}} \frac{m_s}{m_p} = \eta_e^{-1} \eta_s Q_s R_s. \quad (3.41)$$

Now equations Eq. (3.27) and Eq. (3.37), supplemented by the definitions Eq. (3.28)-(3.30) and Eq. (3.39)-(3.40) lay the ground to the parametric instability analysis for a parallel-propagating low-frequency (much lower than the electron and ion gyrofrequencies to preserve the validity of the self-consistent exact nonlinear kinetic pump-wave dispersion relation, but still higher than the MHD Alfvén mode) linear fluctuations in a warm hybrid plasma. This means that the electrons are considered as a charge and current-neutralizing massless fluid, whereas the ions are treated fully kinetically. The final form of the dispersion relation then depends on the kind of plasma to be investigated. In our analysis we mainly consider a hot plasma, consisting of fluid electrons, kinetic protons and α particles, relatively streaming to each other with a bulk speed $V_{\alpha p}$ in the center of momentum framework. What follows below are a couple of examples of the parametric instabilities dispersion relation calculated for several different types of plasmas.

3.1.4 Dispersion relation for electron-proton plasma case

Let us derive the wave dispersion relation, describing parametric instabilities in the simple case, when the plasma consists of fluid electrons and kinetic protons. Since only one ion species is present in the system, we can apply the charge neutrality $n_e = n_p$, and assume that the total net current is zero, to verify that $u_e = u_p = u$. For purely e^- , p plasma the summation in the equation for the magnetic field fluctuations Eq. (3.37) is to be truncated at the very first term. If we keep in mind that in the case of proton and electron plasma the ratio Eq. (3.41) becomes unity, the relation between the magnetic field and the velocity fluctuations simplifies to

$$BR_{+p} \frac{u_p}{V_A} + L_{+p} b_+ = 0, \quad (3.42)$$

where, for the nonrelativistic plasmas considered here,

$$L_{+p} = Y_+^2 - \frac{X'^2_{+p}}{\Psi'^2_{+p}} \quad (3.43)$$

and a similar formula is valid for the complex conjugate b_-^* . To proceed the derivation of the dispersion relation (for this simple $e^- - p$ plasma case) we need to recall the other relation between the velocity and the magnetic field fluctuations coming from the momentum equation, together with the charge and current conservation laws (see Eq. (3.27))

$$\frac{u_p}{V_A} = \frac{B_{+p} b_+ + B_{-p} b_-^*}{BD_p}. \quad (3.44)$$

Note that in this particular case $C_s = 0$. If we substitute the upper equation in Eq. (3.42) and its complex conjugate we have

$$\begin{aligned} (B_{+p}b_+ + B_{-p}b_-^*)\frac{R_{+p}}{D_p} + L_{+p}b_+ &= 0, \\ (B_{+p}b_+ + B_{-p}b_-^*)\frac{R_{-p}}{D_p} + L_{-p}b_-^* &= 0. \end{aligned} \quad (3.45)$$

Finally, after a simple algebra for the dispersion relation describing parametric instabilities of a hybrid warm plasma, consisting of fluid electrons and kinetic protons we obtain

$$B_{+p}R_{+p}L_{-p} + B_{-p}R_{-p}L_{+p} + L_{-p}L_{+p}D_p = 0. \quad (3.46)$$

This dispersion relation was used by [Araneda *et al.* (2008)] to explain the proton core anisotropy and beam formation by Landau damping of daughter ion-acoustic waves, produced by parametric instabilities of large-amplitude Alfvén-cyclotron wave. A good agreement was found between the wave growth rates predicted by the theory and the data obtained from the linear stage of hybrid simulations.

3.1.5 Electron-proton-alpha particles

Let us now proceed with the most relevant for our analysis case, namely a hot nonrelativistic hybrid plasma, consisting of fluid electrons and discrete protons and α particles, counterstreaming in the center of momentum frame at different drift speeds. Keeping in mind Eq. (3.41) and taking into account the charge and mass ratios, Eq. (3.37) and its complex conjugate read:

$$L_{+\alpha}b_+ + \eta_e^{-1}B\left(R_{+p}\frac{u_p}{V_A} + 4\eta_\alpha R_{+\alpha}\frac{u_\alpha}{V_A}\right) = 0, \quad (3.47)$$

$$L_{-\alpha}b_-^* + \eta_e^{-1}B\left(R_{-p}\frac{u_p}{V_A} + 4\eta_\alpha R_{-\alpha}\frac{u_\alpha}{V_A}\right) = 0, \quad (3.48)$$

with

$$L_{\pm\alpha} = Y_\pm^2 - \frac{X_\pm^2}{1 + 2\eta_\alpha} \left(\Psi_{\pm p}^{-1} + 4\eta_\alpha \Psi_{\pm\alpha}^{-1} \right). \quad (3.49)$$

To derive the dispersion relation we use the momentum equation Eq. (3.27) for protons and alpha particles

$$D_p \frac{u_p}{V_A} = \frac{B_{+p}b_+ + B_{-p}b_-^*}{B} - C_p, \quad (3.50)$$

$$D_\alpha \frac{u_\alpha}{V_A} = \frac{B_{+\alpha}b_+ + B_{-\alpha}b_-^*}{B} - C_\alpha, \quad (3.51)$$

where according to Eq. (3.30)

$$C_p = 2\eta_e^{-1}\eta_\alpha r_p \beta_e Y^2 \frac{X'_p}{X'_\alpha} \frac{u_\alpha}{V_A}, \quad C_\alpha = \frac{r_\alpha \beta_e Y^2}{2\eta_e} \frac{X'_\alpha}{X'_p} \frac{u_p}{V_A} \quad (3.52)$$

and D_p , D_α are defined by Eq. (3.29). If we combine Eq. (3.50)-(3.51) with Eq. (3.47)-(3.48) and manipulate them the dispersion relation for parametric instabilities takes the form

$$L_{+\alpha}L_{-\alpha} - C_{1+}L_{-\alpha} - C_{1-}L_{+\alpha} + C_{1+}C_{1-} - C_{2+}C_{2-} = 0, \quad (3.53)$$

where we have used the notations

$$C_{1\pm} \equiv \frac{R_{\pm p}\tilde{B}_{\pm p} + 4\eta_\alpha R_{\pm\alpha}\tilde{B}_{\pm\alpha}}{\eta_e\tilde{D}}, \quad (3.54)$$

$$C_{2\pm} \equiv \frac{R_{\mp p}\tilde{B}_{\pm p} + 4\eta_\alpha R_{\mp\alpha}\tilde{B}_{\pm\alpha}}{\eta_e\tilde{D}}, \quad (3.55)$$

and

$$\tilde{D} \equiv D_\alpha D_p - \eta_\alpha r_\alpha r_p \eta_e^{-2} \beta_e^2 Y^4, \quad (3.56)$$

$$\tilde{B}_{\pm\alpha} \equiv B_{\pm\alpha} D_p - r_\alpha \eta_e^{-1} \beta_e Y^2 / 2B_{\pm p} X'_\alpha / X'_p, \quad (3.57)$$

$$\tilde{B}_{\pm p} \equiv B_{\pm p} D_\alpha - 2\eta_\alpha r_p \eta_e^{-1} \beta_e Y^2 B_{\pm\alpha} X'_p / X'_\alpha. \quad (3.58)$$

Neglecting the kinetic effects this result reduces to the dispersion relation, used earlier by [Hollweg *et. al.* (1993)] within the multi-fluid approach to describe the effects of streaming α particles on the instability growth rates for a large-amplitude Alfvén-cyclotron pump wave. Recently, the same dispersion relation, but for non-drifting species, was used by [Kauffmann and Araneda (2008)] to stress the kinetic effects of collisionless damping on the stability conditions of nonlinear Alfvén-cyclotron waves in a multi-species plasma.

3.1.6 Inclusion of oxygen ions

If we follow the same procedure we can proceed and derive the parametric instabilities dispersion relation, describing the growth of daughter electromagnetic and IAWs, when the plasma consists of 3 different ion species, namely p, α, O^{5+} , together with the fluid electrons. The equation of motion Eq. (3.27) for the protons and α particles, together with the 5 times ionized oxygen O^{5+} gives

$$D_p \frac{u_p}{V_A} = \frac{B_{+p}b_+ + B_{-p}b_-^*}{B} - C_p, \quad (3.59)$$

$$D_\alpha \frac{u_\alpha}{V_A} = \frac{B_{+\alpha}b_+ + B_{-\alpha}b_-^*}{B} - C_\alpha, \quad (3.60)$$

$$D_{o5} \frac{u_{o5}}{V_A} = \frac{B_{+o5}b_+ + B_{-o5}b_-^*}{B} - C_{o5}, \quad (3.61)$$

where

$$C_p = \frac{r_p \beta_e Y^2}{\eta_e R_p} \left(\eta_\alpha Q_\alpha \frac{X'_p}{X'_\alpha} \frac{u_\alpha}{V_A} + \eta_{o5} Q_{o5} \frac{X'_p}{X'_{o5}} \frac{u_{o5}}{V_A} \right), \quad (3.62)$$

$$C_\alpha = \frac{r_\alpha \beta_e Y^2}{\eta_e R_\alpha} \left(\eta_p Q_p \frac{X'_\alpha}{X'_p} \frac{u_p}{V_A} + \eta_{o5} Q_{o5} \frac{X'_\alpha}{X'_{o5}} \frac{u_{o5}}{V_A} \right), \quad (3.63)$$

$$C_{o5} = \frac{r_{o5} \beta_e Y^2}{\eta_e R_{o5}} \left(\eta_p Q_p \frac{X'_{o5}}{X'_p} \frac{u_p}{V_A} + \eta_\alpha Q_\alpha \frac{X'_{o5}}{X'_\alpha} \frac{u_\alpha}{V_A} \right). \quad (3.64)$$

We chose O^{5+} as a typical representative of the heavy ion species in coronal holes. Looking back to the Ampere's law for the fluctuations in the presence of these oxygen ions, Eqs. (3.37)-(3.38) turn into

$$L_{+o5}b_+ + \eta_e^{-1} \left(BR_{+p} \frac{u_p}{V_A} + 4\eta_\alpha BR_{+\alpha} \frac{u_\alpha}{V_A} + 16\eta_{o5} BR_{+o5} \frac{u_{o5}}{V_A} \right) = 0, \quad (3.65)$$

$$L_{-o5}b_-^* + \eta_e^{-1} \left(BR_{-p} \frac{u_p}{V_A} + 4\eta_\alpha BR_{-\alpha} \frac{u_\alpha}{V_A} + 16\eta_{o5} BR_{-o5} \frac{u_{o5}}{V_A} \right) = 0. \quad (3.66)$$

It is now straightforward to obtain the dispersion relation describing parametric instabilities in the 4 ion species (e^- , p , α , O^{5+}) plasma

$$L_{+o5}L_{-o5} + L_{+o5}C_{-3} + L_{-o5}C_{+3} + C_{+3}C_{-3} - C_{+4}C_{-4} = 0, \quad (3.67)$$

where the following notations have been introduced

$$C_{\pm 3} \equiv \frac{1}{\eta_e \tilde{D}} \left(R_{\pm p} \tilde{B}_{\pm p} + 4\eta_\alpha R_{\pm\alpha} \tilde{B}_{\pm\alpha} + 16\eta_{o5} R_{\pm o5} \tilde{B}_{\pm o5} \right),$$

$$C_{\pm 4} \equiv \frac{1}{\eta_e \tilde{D}} \left(R_{\mp p} \tilde{B}_{\pm p} + 4\eta_\alpha R_{\mp\alpha} \tilde{B}_{\pm\alpha} + 16\eta_{o5} R_{\mp o5} \tilde{B}_{\pm o5} \right),$$

together with

$$\tilde{B}_{\pm o5} \equiv \tilde{D}/D_0 \tilde{B}'_{\pm o5} + D'_0/D_0 \tilde{B}_{\pm p}, \quad (3.68)$$

$$\tilde{B}_{\pm\alpha} \equiv \tilde{D}/D_0 \tilde{B}'_{\pm\alpha} + D''_0/D_0 \tilde{B}_{\pm p}. \quad (3.69)$$

In addition we have denoted

$$D_0 \equiv D_\alpha D_{o5} - \frac{25}{16} \eta_\alpha \eta_{o5} r_\alpha r_{o5} \eta_e^{-2} \beta_e^2 Y^4,$$

$$D'_0 \equiv \frac{5}{16} r_{o5} \eta_e^{-1} \beta_e Y^2 \left(\eta_\alpha r_\alpha \eta_e^{-1} \beta_e Y^2 - D_\alpha \right) \frac{X'_{o5}}{X'_p},$$

$$D''_0 \equiv \frac{1}{2} r_\alpha \eta_e^{-1} \beta_e Y^2 \left(\frac{25}{16} \eta_{o5} r_{o5} \eta_e^{-1} \beta_e Y^2 - D_{o5} \right) \frac{X'_\alpha}{X'_p},$$

$$\tilde{B}'_{\pm\alpha} \equiv D_{o5} B_{\pm\alpha} - \frac{5}{2} \eta_{o5} r_\alpha \eta_e^{-1} \beta_e Y^2 B_{\pm o5} \frac{X'_\alpha}{X'_{o5}},$$

$$\tilde{B}'_{\pm o5} \equiv D_\alpha B_{\pm o5} - \frac{5}{8} \eta_\alpha r_{o5} \eta_e^{-1} \beta_e Y^2 B_{\pm\alpha} \frac{X'_{o5}}{X'_\alpha},$$

and

$$\tilde{B}_{\pm p} \equiv D_0 B_{\pm p} - 2\eta_\alpha r_p \eta_e^{-1} \beta_e Y^2 \tilde{B}'_{\pm\alpha} \frac{X'_p}{X'_\alpha} - 5\eta_{o5} r_p \eta_e^{-1} \beta_e Y^2 \tilde{B}'_{\pm o5} \frac{X'_p}{X'_{o5}},$$

$$\tilde{D} \equiv D_p D_0 + D_1, \quad D_1 \equiv 2\eta_\alpha r_p \eta_e^{-1} \beta_e Y^2 D''_0 \frac{X'_p}{X'_\alpha} + 5\eta_{o5} r_p \eta_e^{-1} \beta_e Y^2 D'_0 \frac{X'_p}{X'_{o5}}.$$

This dispersion relation is the first to address the parametric instabilities of large-amplitude Alfvén-cyclotron waves in a hot collisionless plasma, consisting of fluid electrons, kinetic

protons and heavy ions. We should note that incorporating the kinetic effects in all the calculations is implicitly done, hidden in the kinetic expression for the ion plasma β . We should keep in mind, however, that we have included the kinetics in parallel direction only, otherwise we keep the assumption for drifting Maxwellian distributions. This means that we keep only the collisionless damping effects of Landau damping on the growth rates of the daughter wave, but all cyclotron resonance effects (which, due to our simplified geometry, would occur in perpendicular direction only) are completely neglected.

Most of our analysis, both theoretical and simulations, were done for a two-ion-species plasma, consisting of fluid electrons and kinetic protons and α particles. Though we have also investigated the influence of the heavy species (see Chapter 7) from a simulation point of view, a concrete calculation of the growth rates, resulting from the derived parametric instabilities dispersion relation Eq. (3.67), is to be included in a future work and lays beyond the scope of the present analysis.

3.2 Kinetic damping mechanisms

In this section we will briefly describe the wave-particle interactions, which serve as kinetic damping mechanisms and hence attenuate or reduce the growth rate of the daughter waves, produced by the parametric decays. Landau and cyclotron resonances are pure kinetic effects, that attenuate (in case of damping) or amplify (in case of instability) the pure acoustic and longitudinal electromagnetic, or transverse electromagnetic waves respectively. The specific thing about those damping mechanisms is that they act only on waves that fulfill the so-called resonance conditions (see the subsection below). This means that only few waves from a broad spectrum participate in these processes. Quasilinear diffusion, on the contrary, involves a broad spectrum of waves, which can in principle be far away from resonance with the particles and still lead to wave-particle exchange of momentum and reshaping of the particle velocity distributions.

3.2.1 Landau damping and cyclotron resonance

One of the kinetic effects that might arise in a collisionless thermal plasma, affecting the propagation of longitudinal electromagnetic or pure electrostatic fluctuations is the Landau damping. Under equilibrium conditions all waves in a plasma system tend to damp out and in the final stage only thermal fluctuations survive. If the thermal motion creates small-scale electric fluctuations, they are immediately damped out by the Landau damping. Derivation of the Landau damping and description of its physics are given for example by [Boyd and Sanderson (1969); Melrose (1986); Baumjohann and Treumann (1997a)]. If we perform a Fourier-Laplace transform and integrate to solve the Vlasov equation for longitudinal fluctuations in a thermal plasma, where the particles obey Maxwellian velocity distribution f_0 , when a certain relation between the wave-frequency ω and the parallel velocity of the particles $v_{\parallel i}$ is satisfied,

$$\omega - kv_{\parallel i} = 0, \quad (3.70)$$

a wave-particle interaction occurs and energy and momentum can be exchanged. The upper relation gives the resonance condition for Landau damping, which in general depends

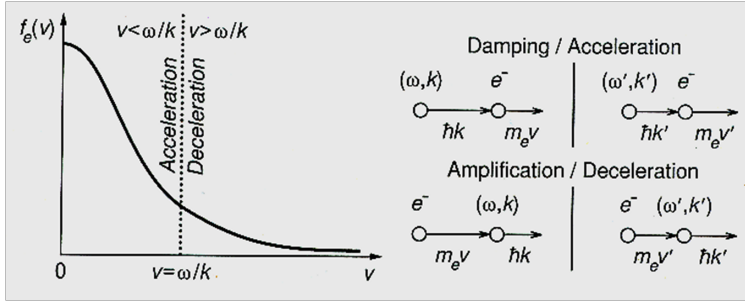


Figure 3.1: Schematic representation of the Landau damping leading to acceleration or deceleration of thermal electrons, depending on the phase speed of the wave and the electron velocity. If the electrons move slower than the wave, they extract energy from the wave and get accelerated and vice-versa, if they move faster, then they are forced to slow down. In the first case the wave attenuates and we have the classical Landau damping, whereas in the second case an instability occurs and the wave starts to grow. We should note that when the resonance condition is met, for ion beam formations the Landau damping is more significant at the tail of the Maxwellian distribution, where there are less particles and therefore it is easier to move them.

on the velocity gradient of the distribution function $\partial f_0 / \partial v$, as shown for a pure electron plasma on Fig. 3.1.

Apart from the Landau damping, which operates on longitudinal fluctuations, in an thermal plasma there exist a collisionless mechanism for dissipation or amplification of transverse electromagnetic waves, called cyclotron damping. It is very similar to the Landau damping, but takes into account the fact that in a magnetized media, apart from the parallel motion, due to the Lorenz force the particles are forced to gyrate around the magnetic field, thus following spirals. The gyration rate is different for each species i and is given by their gyro-frequency Ω_i . The resonant condition for cyclotron damping of transverse fluctuations then becomes

$$\omega - kv_{\parallel i} = n\Omega_i, \quad n = \pm 1, \pm 2, \dots \quad (3.71)$$

The resonant phase speed of the waves in this case also depends on the parallel velocity of the particles $v_{\parallel i}$, but this time the resonant frequency is shifted by the cyclotron frequency of the given species Ω_i . Again, we can have acceleration and wave damping, or particles deceleration and associated wave growth. The number n takes positive values for ions and negative ones for the gyration of electrons. For a parallel wave propagation $n = \pm 1$ only.

3.2.2 Quasilinear diffusion

The quasilinear diffusion theory assumes a very slowly changing (on long terms, with zero short time average) homogeneous background ion distribution function $f_0(\mathbf{v}, t)$ on top of which a small rapidly varying fluctuation is superimposed. It presumes also that

the space average of the rapidly varying part equals the background distribution. Then we linearize the Vlasov equation (given below, see Eq. (4.1)) for the rapidly varying part, perform Fourier-Laplace transformation (for both the distribution function and the electromagnetic fields) and take the space average. This brings us to a diffusion equation for the slowly varying background distribution in the velocity space

$$\frac{\partial f_0}{\partial t} = \frac{\partial}{\partial \mathbf{v}} D \frac{\partial f_0}{\partial \mathbf{v}}, \quad (3.72)$$

where the diffusion coefficient D is a function of the particles velocity \mathbf{v} , the waves spectra (i.e. the spectral density of the electromagnetic fields) and the frequencies and wave-numbers coming from the Fourier-Laplace transforms. Thus in general the quasi-linear diffusion equation describes self-consistently the respond of the global background distribution to some small rapid local variations and its interaction with the electromagnetic waves (as the electromagnetic fields are expressed as a superposition of waves). In this sense it describes the nonlinear plasma dynamics and wave-particle interactions in terms of their global effect on the velocity distribution function for all kinds of waves (unlike the Landau and cyclotron dampings that are related only to waves, restricted by the resonance conditions). We should note however, that the quasi-linear diffusion is restricted to small deviations from the background distribution and one should keep this in mind when applying it for large wave amplitudes.

Now, even though signatures of quasilinear diffusion are present in the simulation results (at the front of the distributions and at the backside of the beams), our work does not include an analysis based on quasilinear diffusion, but rather explains the physics in terms of parametric instabilities, nonlinear Landau damping and cyclotron resonance. For an introduction to the quasilinear diffusion see, for instance, Ref. [Galeev and Sagdeev (1989); Swanson (1989); Treumann and Baumjohann (1997b)].

4 Numerical modeling of nonlinear processes in multi-species plasmas - hybrid simulations

In order to investigate the kinetic behavior of low β ions and to better understand the origin of their non-thermal features as observed in the corona and the solar wind, we performed series of numerical simulations, utilizing a fully nonlinear one-dimensional hybrid code. It treats simultaneously parallel wave propagation, wave-wave and wave-particle interactions in a quasineutral initially homogeneous collisionless plasma, consisting of fluid massless electrons and kinetic ions.

In the first section we describe the numerical methods, followed by a detailed explanation on the initial setup and its relation to the solar wind plasma conditions. In the third section we refer to the applicability of parametric decays as a natural cascading mechanism, that provides channels for energy transfer via wave-wave couplings and generates micro-turbulence in space plasmas. In the end we provide few examples of growth rates for IAWs during the linear stage of the simulations that are well explained with the production of daughter waves via parametric instabilities.

4.1 Description of the code

4.1.1 From Vlasov to superparticles: the idea of PIC codes

To follow the evolution of the particle velocity distribution functions f_s under the collisionless low plasma β conditions in the solar corona and the fast solar wind we need to look at the kinetic Vlasov equation for each ion species separately

$$\frac{\partial f_s}{\partial t} + \mathbf{v} \cdot \frac{\partial f_s}{\partial \mathbf{x}} + \frac{q_s}{m_s} \left(\mathbf{E} + \frac{\mathbf{v} \times \mathbf{B}}{c} \right) \frac{\partial f_s}{\partial \mathbf{v}} = 0, \quad (4.1)$$

where the index s labels the different species and standard notations for the particles charge q_s , mass m_s , electric field \mathbf{E} , velocity \mathbf{v} and magnetic field \mathbf{B} have been used. To solve this equation we need information about the electromagnetic fields. The latter are

prescribed by the Maxwell equations

$$\nabla \cdot \mathbf{E} = \rho / \varepsilon_0, \quad (4.2)$$

$$\nabla \cdot \mathbf{B} = 0, \quad (4.3)$$

$$\nabla \times \mathbf{E} + \partial_t \mathbf{B} = 0, \quad (4.4)$$

$$\nabla \times \mathbf{B} - \varepsilon_0 \mu_0 \partial_t \mathbf{E} = \mu_0 \mathbf{J}. \quad (4.5)$$

Within a self-consistent description the net charge densities ρ and currents J themselves depend on the particles distribution function (being set by the first and the second moment respectively) which makes the Vlasov equation highly non-linear and very difficult for numerical (and analytical) treatment in general. A way to facilitate the numerical problem avoiding direct calculation of the Vlasov equation is to introduce the so-called Particle-In-Cell (PIC) method [Birdsall and Langton (2004)], which solves the Vlasov equation in an indirect manner. Instead of calculating the distribution functions for the real physical ions, PIC methods use the concept of computational particles and solve the corresponding equations of motion for them. Let us assume that the distribution function for a given s species is a superposition of several elements, called computational or superparticles

$$f_s(\mathbf{x}, \mathbf{v}, t) = \sum_p f_p(\mathbf{x}, \mathbf{v}, t). \quad (4.6)$$

Each superparticle represents a large number (a ‘‘cloud’’) of real physical particles that are near each other in phase space. The distribution of the superparticles

$$f_p(\mathbf{x}, \mathbf{v}, t) = N_p S_x(\mathbf{x} - \mathbf{x}_p(t)) S_v(\mathbf{v} - \mathbf{v}_p(t)) \quad (4.7)$$

is determined by the shape functions $S_x(\mathbf{x} - \mathbf{x}_p(t))$ and $S_v(\mathbf{v} - \mathbf{v}_p(t))$ (that depend on the superparticles position $\mathbf{x}_p(t)$ and velocity $\mathbf{v}_p(t)$) and is normalized by the number of physical particles N_p in the element of the phase space represented by the superparticle. We should note that at each time step the total number of particles for each species is conserved $N = \text{const}$, so that we do not allow the plasma to leave the computational volume. Thus the distribution of each computational particle has a specific functional form with a number of free parameters whose time evolution will determine the numerical solution of the Vlasov equation. By definition the shape functions need to have compact support, to be normalized, and additionally we assume them to be symmetric. The shape function in velocity space is assumed to be a simple δ -function

$$S_v(\mathbf{v} - \mathbf{v}_p) = \delta(\mathbf{v} - \mathbf{v}_p), \quad (4.8)$$

whereas for the shape function which determines the space dependence of the superparticle distributions we use a second order polynomial, i.e. a second order b-spline function:

$$S_x(\mathbf{x} - \mathbf{x}_p) = b_1 \left(\frac{\mathbf{x} - \mathbf{x}_p}{\Delta p} \right), \quad (4.9)$$

where Δp is the length-scale of the support of the superparticle and

$$b_l(\xi) = \int_{-\infty}^{+\infty} d\xi' b_0(\xi - \xi') b_{l-1}(\xi) \quad (4.10)$$

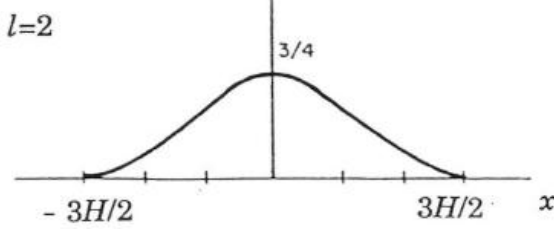


Figure 4.1: Second order b-spline used as an interpolation function to relate the particles position to the grid and to weigh the fields back to the particles [Lapenta (2008)].

with b_0 being the top-flat function

$$b_0(\xi) = \begin{cases} 1, & \text{if } \xi < 1/2 \\ 0, & \text{elsewhere} \end{cases} \quad (4.11)$$

If we now take the first moments of the Vlasov equation using the concept of the superparticles and take into account their distribution (determined by the shape functions) we can derive the equations of motion for the computational particles and the effective electromagnetic fields that they feel. The relation between the position of the superparticles in their own frame and on the grid (where all the physical quantities like densities, currents, electromagnetic fields, etc. are computed) is given by the interpolation function as we will see below. The same is true for the relation between the electromagnetic fields and the force exerted on the superparticles.

1. Equations of motion for the superparticles

Taking moments of the Vlasov equation (i.e. integrating the Vlasov equation in the entire phase-space over the velocities and spatial coordinates) provides a set of constraints for the superparticle species. The zeroth order moment leads to a conservation law for the number of physical particles, present in the phase-space volume, occupied by a single computational superparticle

$$\frac{dN_p}{dt} = 0. \quad (4.12)$$

This means that each computational particle is represented by a cloud with the same (fixed) number of real particles and the total number of physical particles in the entire computational box is conserved. The first moment of the Vlasov equation (with respect to the spatial coordinates) gives the general equation of motion for the computational particles

$$\frac{d\mathbf{x}_p}{dt} = \mathbf{v}_p. \quad (4.13)$$

The first moment in velocity space results in the complementary Newton law used to advance them

$$\frac{d\mathbf{v}_p}{dt} = \frac{q_s}{m_s} \left(\mathbf{E}_p + \frac{\mathbf{v}_p \times \mathbf{B}_p}{c} \right), \quad (4.14)$$

where \mathbf{E}_p and \mathbf{B}_p are the electric and magnetic fields

$$\mathbf{E}_p = \int S_x(\mathbf{x} - \mathbf{x}_p)\mathbf{E}(\mathbf{x})d\mathbf{x}, \quad (4.15)$$

$$\mathbf{B}_p = \int S_x(\mathbf{x} - \mathbf{x}_p)\mathbf{B}(\mathbf{x})d\mathbf{x}, \quad (4.16)$$

calculated in the frame of reference of the superparticles (see the next item for a regorous explanation).

2. Equations for the electromagnetic fields

Now that we know how do the superparticles evolve in time, in order to advance them we need to look at the field equations to see how the electric and magnetic fields (that depend on the real space coordinates and are set on the grid) are related to the computational particles. To do this, however, first we need to set the continuous electromagnetic fields on the grid. If we assume that the fields are constant at each cell and their magnitudes are given by the cell averaged values \mathbf{E}_i and \mathbf{B}_i , we can reconstruct the continuous field in the following way

$$\mathbf{E}(\mathbf{x}) = \sum_i E_i b_0 \left(\frac{\mathbf{x} - \mathbf{x}_i}{\Delta x} \right). \quad (4.17)$$

Then the relation between the electromagnetic fields on the grid $\mathbf{E}_i, \mathbf{B}_i$ and the corresponding ones in the superparticles reference frame $\mathbf{E}_p, \mathbf{B}_p$ is

$$\mathbf{E}_p = \sum_i \mathbf{E}_i W(\mathbf{x}_i - \mathbf{x}_p), \quad (4.18)$$

$$\mathbf{B}_p = \sum_i \mathbf{B}_i W(\mathbf{x}_i - \mathbf{x}_p), \quad (4.19)$$

given by the so-called interpolation function

$$W(\mathbf{x}_i - \mathbf{x}_p) = \int_{-\infty}^{\infty} S_x(\mathbf{x} - \mathbf{x}_p) b_0 \left(\frac{\mathbf{x} - \mathbf{x}_i}{\Delta x} \right) d\mathbf{x}. \quad (4.20)$$

If we apply the definition of the b-splines Eq. (4.10) under the assumptions that the size of the superparticle equals the cell size ($\Delta p = \Delta x$) and the shape function is a first order bi-spline (see Eq. (4.9)), we will see that the interpolation function (for both fields and particles) is given by a second order polynomial, the so-called second order quadratic b-spline $b_2(\xi)$, visualized on Fig. (4.1). This means that for each grid point x_i (where the physical quantities are computed) we compute the equivalent force exerted on the associates three computational particles. That is to say, the electromagnetic fields at each grid point create effective fields that influence three superparticles, the closest one to the grid point, the one before and the one after. There is also a weighting scheme to assure that the closest superparticle is most affected by the force exerted at that given grid point. Once we know the force we can continue to advance the superparticles in time according to Eq. (4.13) and Eq. (4.13). In order to make an iterative scheme though, we need

to self-consistently advance the electromagnetic fields, associated with the new position of the particles. For this reason we need to solve the field equations that depend on the charge densities and the currents. The latter ones themselves depend on the superparticles positions and velocities, which have already been advanced using the previous electromagnetic fields. Then to calculate the densities and the currents (that are evolved on the grid) we need another interpolation, similar to the one used for the fields. This time we have to interpolate from the superparticles reference frame to the physical grid. To do so we use the same weighting scheme and second order interpolation function Eq. (4.20), only that this time each position of a superparticle gives a contribution to the charge density at 3 grid points (with greatest weight given to the closest grid cell). In the same manner the velocity of each superparticle contributes to the calculation of the current at 3 grid points. The formal relations are similar to Eq. (4.18)

$$\rho_i = \sum_p \frac{q_s N_p}{\Delta x} W(\mathbf{x}_i - \mathbf{x}_p) \quad (4.21)$$

and the normalization factor comes from the fact that we work with cell averaged quantities.

Now our next step is to see how exactly the equations of motion for the superparticles are solved and how the electromagnetic fields are advanced. As there are many different ways to do so, the particular schemes used in our code will be further explained in the next subsection, where we introduce the main concept of hybrid codes.

To summarise, the main message of this subsection is as follows: instead of explicitly solving the Vlasov equation for the whole distribution function for each species, we follow the equations of motion for each single superparticle, then determine its position on the grid, collect the moments (compute the mass and charge densities, temperatures, bulk velocities and currents), use those moments to calculate the electromagnetic fields, see how those fields act on the particles (through the Lorenz force) and then advance the particles position again (see Fig. 4.2). This is done in an iterative manner and the information about the computed moments at regular times is saved for later diagnostics. Then we can reconstruct the velocity distribution functions of the real (physical) particles just by counting the number of superparticles with a given velocity at a given position (see Eq. (4.6)). This general computational cycle is valid for the ion species (whose kinetics we are interested in) in both PIC and hybrid codes. The following subsection introduces the one-dimensional hybrid code used for our simulations and explains the main difference between it and the PIC codes.

4.1.2 1D hybrid code

There are different types of hybrid codes according to the ultimate purpose they serve, that is to say depending on the physical problem to be solved. In our case the term hybrid code [Winske and Omid (1993)] is used in the sense that it is a mixture between MHD (that solves the magnetohydrodynamic set of equations) and a PIC code (that includes

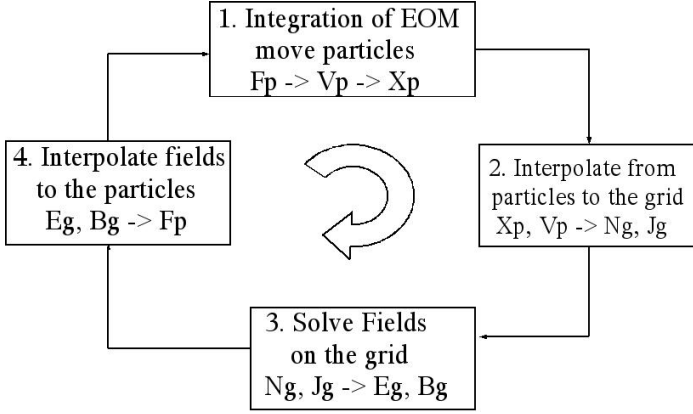


Figure 4.2: Computational cycle for PIC and hybrid codes.

information on the particles kinetics as described above). Furthermore we use that type of hybrid codes that treats the electrons as a single magnetized fluid, whereas the ions are depicted fully kinetically, using the PIC method. This means that we do not resolve the kinetic nature of the electrons (like full PIC or direct Vlasov codes do), but rather describe them in fluid terms and in principle can get information about their moments. In order to facilitate the interpretation of the results and to have a gain in computing time, our research is based on a one dimensional hybrid code. That is to say that all physical quantities depend only on one space coordinate z (in radial direction), but nevertheless all three components of the velocities are retained (as a function of this space coordinate). Furthermore we are not interested in the electron dynamics and treat this specie as a massless, $m_e \approx 0$, isothermal, $T_e = \text{const.}$, and inviscid $\eta = 0$ fluid, with an ideal gas equation of state $p_e = n_e k_B T_e$. Now the main difference between the full PIC code described above and the hybrid code used for our simulations is in the way we compute the electromagnetic fields. Instead of solving the Gauss equation, in the hybrid code the evolution of the electric field is derived from the momentum equation for the fluid electrons

$$m_e \frac{d\mathbf{v}_e}{dt} = 0 = -en_e \mathbf{E} + \frac{\mathbf{J}_e \times \mathbf{B}}{c} - \nabla p_e, \quad (4.22)$$

where no artificial viscosity has been *ab initio* included. Thus the electrons only contribute to the electric field through their pressure gradient and the current in the Lorentz force. In addition we assume that the plasma is quasi-neutral, (which guarantees that the Gauss law is preserved) and that the total current is conserved. Once given the electric field at the beginning, the magnetic field is computed following Faraday's law. Then, given the magnetic field, the electric current is calculated from the ion currents via Ampere's law

$$\mathbf{J}_e = \frac{c}{4\pi} \nabla \times \mathbf{B} - \mathbf{J}_i, \quad (4.23)$$

where we consider non-relativistic plasma and neglect the displacement current $\varepsilon_0 \mu_0 \partial_t \mathbf{E}$ as well justified in the solar corona and the solar wind. The ion currents are determined

from the superparticles velocities in the PIC part of the hybrid code. Finally the electric field is advanced according to the electron momentum equation, with the Lorenz set by the above values of the electric current and the magnetic field, and with the same (constant) pressure gradient, as set by the electron plasma $\beta_e = 2n_e k_B T_e / m_p V_A^2$.

In order to solve this closed system for the fields numerically we need to discretize not only the spatial coordinate (as done by the interpolation function for both particles and fields), but also in time. The time discretization for the fields and currents is done using the method of functional iteration, meaning that for each time step several iterations of the field equations are done until convergence is reached. And the time derivatives are computed with a time-centered finite difference scheme. The space derivatives for the fields are computed using a fourth order finite difference approximation [Watanabe and Sato (1993)] and the particles are advanced in time by a leap-frog algorithm. The leap-frog scheme applies a staggered grid for the time levels of the velocity and the positions in the Newtonian equations of motion for the ions. Then in Eq. (4.13) the position at time level $N + 1$ (in terms of the fixed time step $dt = 0.03$) is calculated from the position at time level N and the velocity at time level $N + 1/2$. Similarly in Eq. (4.14) the velocity at time level $N + 3/2$ is computed from the velocity at time level $N + 1/2$ and the electromagnetic fields at time level N (i.e. the fields associated with the position z given at the time level N). We should note that the leap-frog scheme is generally stable and is of second order accuracy, unlike the explicit Euler scheme, which is first order accurate only. In this staggering algorithm we assume that the ion currents do not change during the half a time step off-set $\mathbf{J}_i^{N+1} = \mathbf{J}_i^{N+1/2}$, i.e. from the ion velocities at time level $N + 1/2$ we calculate the currents at the same level and then use them to calculate the corresponding electromagnetic field at level $N + 1$.

Finally, we should note that we assume periodic boundary conditions for both particles and fields (which means that no plasma is allowed to leave the box), no adaptive mesh refinement is implemented and the code is not parallelized. In the next subsection we explain specific technical and physical details related to the initial setup for our simulations.

4.2 Initial setup

To initialize the code we need to supplement information about the electromagnetic fields and the corresponding velocities at the beginning. For this reason we have to explain the physical background behind the simulations and to consider its numerical implementation.

4.2.1 Physical considerations

We construct the initial configuration for the magnetic field as a superposition of a static homogeneous background $\mathbf{B}_0 = B_0 \hat{z}$ along the spatial coordinate (that is a measure for the radial distance from the Sun) and a transverse part, that corresponds to a large-amplitude left-hand circularly polarized Alfvén-ion-cyclotron wave. The background magnetic field in our investigations represents the typical locally open solar magnetic field lines within a coronal hole region or further out in the fast solar wind. The fluctuating part, given by the finite-amplitude Alfvén-cyclotron wave, is not arbitrarily chosen, but is rather an

exact nonlinear solution of the hot kinetic collisionless plasma dispersion relation and is self-consistently coupled to the ion species. Therefore its frequency ω_0 and wave-number k_0 depend on the plasma composition, the gyro- and the plasma frequencies of the different species s . For frequencies much lower than the electron gyration ($\omega_0 \ll \Omega_e$), the non-relativistic dispersion relation for the wave (that will play the role of a pump wave in our analysis, cf. Chapter 3, Sec. 3.1) resembles the cold plasma dispersion relation [R. Davidson (1972)]

$$k_0^2 c^2 + \sum_{i \neq e} \frac{\omega_{pi}^2}{\Omega_i} \left[\frac{(\omega_0 - k_0 V_i)^2}{\omega_0 - k_0 V_i - \Omega_i} \right] = 0, \quad (4.24)$$

with $\omega_{pi}^2 = 4\pi n_i q_i^2 / m_i$ being the plasma frequency, $\Omega_i = q_i B / cm_i$ – the gyrofrequency and V_i – the parallel drift speed of the i -th ion species in the center of mass frame of reference. More details on the dispersion relation for a plasma composed of different ion species are given in Appendix A.

Now, even though mathematically this dispersion resembles the cold collisionless plasma linearized kinetic dispersion relation for parallelly propagating low amplitude waves, Eq. (4.24) is valid for a large set of ion distributions, considering nonlinear parallel wave propagation in a hot collisionless homogeneous plasma. This solution was found in the late 1960s by Sonnerup, who initially investigated propagation of large-amplitude whistler modes with right-hand polarization [Sonnerup and Su (1967)]. He showed that in a hot homogeneous collisionless plasma nonlinear whistler waves can coexist with the particles, given that the ion velocity distributions have specific shapes, that can be used as characteristics of the waves. If no waves are present in the system, the ion distributions would look like normal Maxwellians (that might be drifting or not). In the presence of even small amplitude waves though, Sonnerup's solution to the Vlasov equation implies that the ion distributions acquire “apparent” anisotropies, μ ,

$$f_i(v_x, v_y, v_z, z, t) = f_i \left[\mu (v_x - V_{xi})^2 + \mu (v_y - V_{yi})^2 + (v_z - V_i)^2 \right], \quad (4.25)$$

related to the waves in the following way: $\mu = 1 - \omega_0 / \Omega_i + k_0 V_i / \Omega_i$. Thus each wave brings its characteristic anisotropies and we might call them “apparent” as they are only caused by the coherent motion of all particles in the wave-associated electromagnetic fluctuations (and not related to a random motion). Then we can say that (in the standard sense) the velocity distributions are actually isotropic and the “apparent” anisotropies appear only when a wave is present and they vanish if for some reason the wave is depleted or damped. As clear from Eq. (4.25), the magnitude of the apparent anisotropy depends on the characteristic parameters of the wave (wave-number and frequency), as well as on the gyrofrequency and the bulk speed of the ion species. We should however point out that the relation Eq. (4.25) holds for a monochromatic wave only and so far has not been generalized for a broad wave spectrum.

The “apparent” anisotropies reflect the behavior of the ions in response to the electromagnetic field of the wave. Namely, the particles are forced by the wave to follow certain orbits in perpendicular (with respect to the wave propagation and the ambient magnetic field) direction, that are both characteristic for the wave and depend on the particle species. This results in a transverse bulk motion

$$\mathbf{V}_{\perp i} = - \frac{\omega_0 / k_0 - V_i}{1 - (\omega_0 - V_i k_0) / \Omega_i} \delta \mathbf{B} / B_0, \quad (4.26)$$

bound to the pump wave amplitude $\delta\mathbf{B} = \delta B [\cos(k_0 z - \omega_0 t)\hat{x} + \sin(k_0 z - \omega_0 t)\hat{y}]$, which is typically chosen to be a substantial fraction of the external magnetic field $\delta B/B_0 = 0.25$. Now we include this drift as part of the initial velocity field for the superparticles. There are three independent components that build up the velocity field used to initialize the code: the thermal speed, a parallel bulk velocity in the direction of propagation and a perpendicular drift (caused by the wave induced bulk motion of the whole ion distributions described above; takes a characteristic value for each individual particle species, according to Eq. (4.26)). The thermal speed is a free parameter given by the initial plasma β of the ions. The parallel drift is also a free parameter, whereas the transverse drift is fixed by the amplitude of the initial pump wave, its frequency, wave-number and the gyrofrequency of the given species. That means that all species react to the pump wave in a different manner and acquire diverse transverse bulk speeds, which result in different “apparent” anisotropies.

Now let us look at the numerical implementation of the initial conditions.

4.2.2 Numerical issues

To initialize a run we need to load the particles with a given distribution. To do this properly (in accordance with Sonnerup’s solution Eq. (4.25)), we consider that the ions are homogeneously distributed and initiate them with a random bi-Maxwellian (that is implemented by the so-called “random start”, realized by an intrinsic fortran random function), drifting in both parallel and transverse direction. The width of the Maxwellian distributions (i.e. the temperature of the ion species) is given by the ion plasma beta as determined by the squared ratio of the thermal to Alfvén speed $\tilde{\beta}_i = 2k_B T_i / (m_i V_A^2)$. Though in principle we can allow for all kinds of anisotropies, our entire analysis was made assuming initially isotropic distributions. The reason for this is that the dispersion relation, used to determine the frequency and the wave number of the pump wave Eq. (4.24), is valid only for isotropic distributions. If we include anisotropies we have to search for another proper exact nonlinear solution of the Vlasov-Maxwell set of equations, that would describe the particle behavior and the plasma oscillations in a hot anisotropic plasma, which is beyond the scope of this work. Another reason to avoid initializing the code with anisotropic distributions is that we would like to study the origin of the non-thermal features in solar plasmas and hence we want to investigate the formation of ion anisotropies and relative drifts. Moreover, anisotropies affect also the plasma instabilities and thus represent an additional free energy source for ion heating and acceleration, which we will try to avoid (more details will be given later in Chapters 5, 6 and 7).

The wave amplitude and the wave-number of the pump in our simulations are fixed to $\delta B/B_0 = 0.25$ (as given above) and $0.4\Omega_p/V_A$, respectively, and all units are normalized by the Alfvén speed $V_A \equiv B_0^2 / (4\pi n_e m_p)$ (as determined by the magnitude of the external magnetic field B_0 , the electron density n_e and the proton mass m_p) and the proton gyration frequency $\Omega_p = eB/cm_p$. The pump wave-frequency is given by the solution of Eq. (4.24) given the concrete value of the parallel drifts and the number density of the particles. For the minor alphas we use $n_\alpha = 0.05n_e$, whereas for the heavy ions we assume even smaller densities as derived on average *in situ* in the solar wind at distances up to 1 AU: $n_O = 0.0003n_e$ – for oxygen and $n_C = 0.00023n_e$ – for carbon ions respectively. We have used variable plasma $\tilde{\beta}_i$ throughout our research. Typically we analyse low β

regimes with $\tilde{\beta}_i < 0.1$ as they represent characteristic conditions in coronal holes and the fast solar wind. The concrete values will be given in each chapter separately. We assume the fluid electrons to be warmer than the ions $\beta_e = 0.5$, as this facilitates the onset of the parametric instabilities, but does not have a direct influence on the consequent ion heating and acceleration.

The number of superparticles per cell N_p (that determines the level of the numerical noise) varies between 200 and 800, depending on the ion composition. Typically we take $N_p = 400$ for a plasma consisting of protons and α particles (together with the fluid electrons) and $N_p = 200$ if we include heavy ions (like oxygen or carbon) as well. We should note though that further increasing the number of particles per cell practically does not change the simulation outcome.

The length of the computational box depends on the wave-length $\lambda = 2\pi/k_0$ of the pump wave and is fixed to be $L = 32\lambda$, which in case of $k_0 = 0.4\Omega_p/V_A$ reads $502, 4V_A/\Omega_p$. The number of grid points is set to 2048, whereas the resolution can be changed, depending on the time step (usually $dt = 0.03\Omega_p^{-1}$). All the moments are regularly saved up at a fixed interval and the simulation time is controlled by the number of iterations multiplied by the fixed time step dt . Further specific details will be provided later in the chapters on the simulation results (Chapters 5, 6 and 7).

In the next section we will present two examples how the simulation outcome can be well interpreted within the parametric instabilities theory.

4.3 Application to parametric instabilities of Alfvén-cyclotron waves

Now that we have learned how the code works and how to initialize it in a meaningful way we can apply it as a test of the parametric instabilities analysis. If the theory is correct we should be able to predict the regimes for individual parametric instabilities that occur in a plasma for a fixed set of initial conditions. We can compare the predicted growth rates for the daughter waves with the ones calculated for the linear stage of the simulations (while the daughter wave-amplitudes are still small enough in comparison with the background magnetic field and the pump wave itself). Then we can check how relevant the parametric instabilities theory is for the analysis of plasma instabilities, driven by wave-wave couplings. We should note that different physics is included in the analytical analysis and in the direct numerical simulations, as the parametric instabilities theory presented above includes the ion kinetics only partially. It means that it allows only for Landau damping (as it retains information about the kinetics only in parallel direction) and smears out the effects of cyclotron damping (which in our simple 1D geometry with a homogeneous ambient magnetic field appear only in perpendicular direction). How significant that difference exactly is depends on the initial conditions, so that we can try to inverse the problem and infer some information about the relevance of the cyclotron damping effects for the ion heating in the system by comparing the difference in the predicted and simulated growth rates. We should stress, however, that this wave-wave coupling theory is still linear, in the sense that we linearize perturbations of an initially stable nonlinear state. Therefore a direct comparison with parametric instability analysis is meaningful only for the linear stage of the simulations. After that, the generated daughter waves may grow large enough

to play the role of a pump themselves, which results in additional nonlinear wave-wave couplings and wave-particle interactions. In what follows we will show an example of the growth rates of daughter ion-acoustic waves generated through modulational and decay-like (decay or beat) instabilities. In the given example cyclotron damping doesn't affect the ion-acoustic waves growth rates and hence there is a good comparison between the predicted and the simulated growth rates (compare Fig. 4.3 with Fig. 4.4). We should also note that the importance of the cyclotron damping might change in a higher dimensional picture, where the Landau and cyclotron damping might be strongly coupled. The situation can further get more elaborate if we allow for oblique propagation, which will bring additional wave-wave couplings and change the nature of the parametric instabilities. Such investigations, however, are in the scope of a future work and will not be included in the present analysis.

Fig. 4.3 shows the theoretically predicted growth rate (based on the solution of Eq. (3.53)) of the least damped ten daughter IAWs born by parametric instabilities of a large-amplitude Alfvén-cyclotron pump wave, parallel propagating in a plasma consisting of kinetic protons and α particles. Equal ion plasma β , $\beta_i \equiv 8\pi n_i k_B T_i / B_0^2$, for both species are used: $\beta_p = \beta_\alpha = 0.01$, and the number density of the alphas is taken to be 5% of the number density of the protons, $n_\alpha = 0.05 n_p$. The ions are assumed to be at rest in the center of momentum frame of reference, i.e. $V_{\alpha p} = 0$. The mother wave has a wave-number $k_0 = 0.408 \Omega_p / V_A$ and an amplitude $\delta B / B = 0.25$, therefore the peak on the left side of the growth rate denotes a modulational instability, which always involves daughter IAWs with $k < k_0$. The small peak in the middle and the last peak to the right correspond to decay-like instabilities (beat or decay), which involve excitation of backward propagating daughter Alfvén-cyclotron waves. For this set of parameters the decay-like instability is stronger than the modulational. Since Landau damping of the daughter IAWs, produced by the modulational instability is a way to accelerate the ions and create proton and α beams, in our model beam formation requires a strong modulational instability. On the contrary, depending on the relative drift between the ion species, the decay-like instability generates sunward daughter Alfvén-cyclotron waves, which can do pitch angle scattering on the beams and slow them down [Araneda *et al.* (2008); Araneda *et al.* (2009)]. This means that in case of a strong modulational instability we expect the ion distributions to form prominent beams, unless the decay-like instability is dominant like on Fig. 4.3, as the backward propagating daughter Alfvén-cyclotron waves push the ions on the back side of the beam, decelerate them and tend to destroy the beams.

Fig. 4.4 shows again the growth rate of daughter IAWs, but this time calculated from the hybrid simulation data, using a fast Fourier transform of the density fluctuations. The plasma parameters used to initialize the run are the same as on Fig. 4.3. We can see that there is a qualitatively good agreement between the theoretically predicted and the simulated growth rates. The additional peak in the IAWs growth rate from the simulations visible at $k \sim 1.5 \Omega_p / V_A$ on the far right side of Fig. 4.4 is probably due to nonlinear effects, causing additional instabilities. This can be related to a small bunch of fast growing daughter acoustic modes, whose amplitude quickly becomes very large during the stage, which for most of the other modes can be considered as still linear. Since the growth rate is calculated at a given time for all modes simultaneously it does not take into account the fact that some of the modes start to grow faster than the others and this can result in a slight discrepancy between the parametric instability theory and the simulations. Addi-

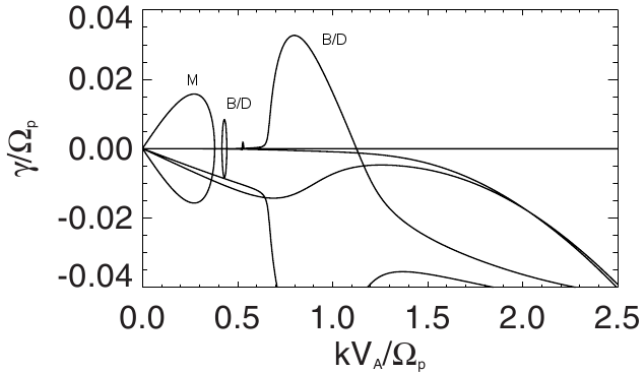


Figure 4.3: Theoretical prediction for the growth rate of daughter IAW generated via parametric instabilities of large-amplitude Alfvén-cyclotron wave in a plasma, consisting of kinetic protons and α particles, together with a charge-neutralizing fluid electrons. Adopted from [Kauffmann and Araneda (2008)].

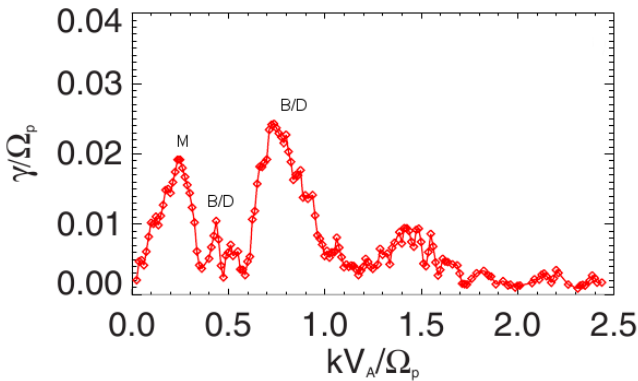


Figure 4.4: Simulation growth rates of the daughter IAWs, generated via parametric instabilities of a large-amplitude Alfvén-cyclotron wave, parallel propagating in a plasma, consisting of kinetic protons and α particles, together with a charge-neutralizing fluid electrons. Adopted from [Kauffmann and Araneda (2008)].

tionally we may have discrepancy due to cyclotron resonance effects, which are excluded from the theoretical calculations.

In the up-coming chapters we will present the results from different numerical simulations and when appropriate interpret them in terms of the parametric instabilities, following the theoretical description presented in Chapter 3.

5 Dissipation of nonlinear Alfvén-cyclotron waves – impact on ion distributions in multi-species plasma

In this chapter we will discuss the influence of nonlinear Alfvén-cyclotron waves and their dissipation on the ion velocity distribution functions in low plasma β conditions corresponding to CHs and fast solar wind. As shown by Sonnerup [Sonnerup and Su (1967)] for a warm kinetic plasma and already discussed in the previous chapter, monochromatic nonlinear waves and particles can coexist and be self-consistently coupled. In this case the ions cannot freely choose their path in the phase space, but their motion rather depends on the amplitude and phase speed of the wave, as well as on the ion drift and gyro-frequency, see Eq. (4.26). Then in the presence of a large-amplitude wave, the particles acquire additional transverse drift (with respect to the direction of the external magnetic field). Thus they obtain apparent transverse anisotropies and appear to be preferentially heated in perpendicular direction, due to the coherent motion of the entire distribution function as a whole. Those apparent anisotropies, however, probably do not last long enough to be observed, as the nonlinear Alfvén-cyclotron waves couple to the thermal fluctuations caused by the random motion of the particles and become parametrically unstable. How fast the parametric decays appear and how large is the amplitude of the daughter waves depend on the level of the acoustic fluctuations (i.e the thermal noise, which itself depends on the initial ion plasma β_i), as well as on other plasma parameters like the pump wave amplitude, frequency and the ion relative drift. In this chapter we present results from numerical simulation aimed to investigate the behavior of the ions in the presence of a nonlinear Alfvén-cyclotron pump wave and to see the resulting effect on ion heating and acceleration.

5.1 Trapping of particles in large-amplitude waves

When the daughter IAWs, born by parametric instabilities of a nonlinear Alfvén-cyclotron pump, grow sufficiently strong, they can trap particles in their potential well. The trapping involves particles whose kinetic energy is lower than the potential energy of the wave. For a monochromatic electrostatic wave that means

$$\frac{1}{2}mv_i^2 - e\phi_0 \cos kx', \quad (5.1)$$

where x' is the position of the particle into the wave frame $x' = x - (\omega/k)t$ [Treumann and Baumjohann (1997b)]. Most of the particles that get trapped are the ones whose velocity matches the phase speed of the wave $v = \omega/k$. Once they are trapped, the particles start oscillating back and forth around the potential trough with a frequency ω_{tr} , depending on their mass and the magnitude of the electric field of the electrostatic wave

$$\omega_{tr}^2 = |e\phi_0 k^2 / m|. \quad (5.2)$$

For electromagnetic waves, the trapping frequency does not depend on the electric potential, but rather on the ions density, the current and magnetic field. When the trapping frequency is much smaller than the Landau damping or growth rate, then the trapping can be neglected. And when the electric field of a monochromatic wave is strong enough to trap the particles, then the growth rate of the Landau damping is modulated by the trapping frequency and becomes a monotonically decreasing oscillatory function of time. When the particles are trapped near the resonant condition, $v = \omega/k$, Landau damping starts to accelerate the particles and deplete the wave. This leads to the formation of positive slopes on the velocity distribution function and thus ion beams are created. If we take a look at the ion velocities versus space, at the position of the trapping phase space holes will be formed, centered at the phase speed of the responsible for the trapping wave (see Fig. 5.6 for example). The thin layer of high-speed particles on top of the phase space holes are the ones, which were accelerated from the constant electric field of the wave at the resonant point and started to form the beam. That can be confirmed if we take a simultaneous look at the particles distribution functions in velocity space. On Fig. 5.1 we can see that at time $t = 530 \Omega_p^{-1}$, together with the trapping (right panel on the first row of Fig. 5.6) we have a clear signature for beam formation in the proton velocity distribution function.

5.2 Heating and acceleration of protons and alpha particles via wave-particle interactions

Beam formation is one of the signatures for ion heating and acceleration. Apart from it, in space weather we encounter evidence of continuous heating of the core of a given species both in parallel and perpendicular direction. Perpendicular heating, associated with parallel cooling was recently discussed by [Yoon and Fang (2009)]. There are many explanations for the preferential perpendicular heating of minor ions. Most of them invoke resonant absorption of ion-cyclotron waves, either locally generated by an instability [X. Li and S. Habbal *et al.* (2005)] or ab initio injected in the system [Ofman *et al.* (2002); Gary *et al.* (2005a); Gary *et al.* (2005b)]. Some works consider non-resonant scattering by Alfvén waves which could produce similar features in the ion distributions [C. Wu *et al.* (2009); S. Bourouaine *et al.* (2008)]. Most of the theories on this subject, however, are constructed under the assumption of small wave-amplitudes or lack self-consistency, using a test particle approach. In the present work we aim at understanding the importance of nonlinearities in space plasmas. For this sake we investigate the effect of finite-amplitude Alfvén-cyclotron waves on the ion heating and acceleration in the fast solar wind. We perform 1D hybrid numerical simulations, initialized with a

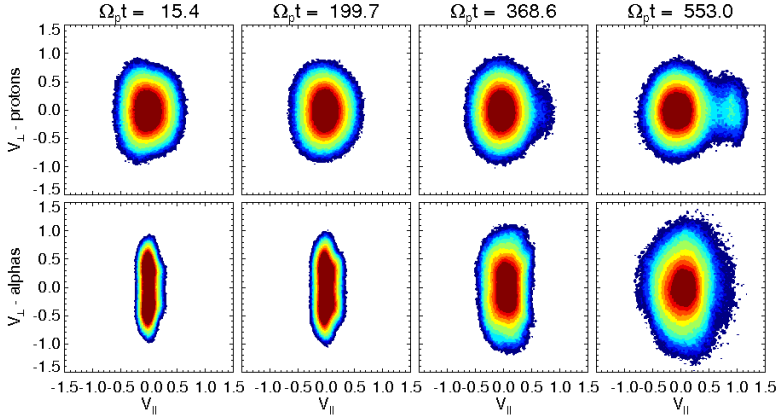


Figure 5.1: Snapshots with contour plots of the 3D velocity distribution functions for protons and α particles. The first 3 columns show the early distributions in the linear stage of the simulations. The last plot on the first row demonstrates the proton beam formation due to Landau damping of the daughter IAWs after the onset of the parametric instabilities.

nonlinear monochromatic Alfvén-cyclotron pump, as described in Chapter 3 and where appropriate analyse the results in terms of parametric instabilities, as presented in Chapter 4. As already discussed in Chapter 2, we are interested in the non-thermal features, typical for the ion velocity distributions in CHs and the fast solar wind. We will try to investigate the origin of the differential streaming between protons and α particles, as well as the origin of ion anisotropies, and preferential heating and acceleration of minor ions. Fig. 5.1 shows the 3D velocity distribution functions for protons and α particles. The parallel velocities are on the x-axis, the perpendicular ones – on the y-axis. The number of particles is given in different colors with dark red showing the densest population and dark blue – the lowest number counts. The simulation was initiated with equal temperatures for both ion species, i.e. $\tilde{\beta}_p = 0.08$ and $\tilde{\beta}_\alpha = 0.02$, where $\tilde{\beta}$ denotes the square ratio of the thermal to Alfvén speed: $\tilde{\beta}_i \equiv v_{th,i}^2/V_A^2$. The pump wave number was fixed to $k_0 = 0.4\Omega_p/V_A$ and the corresponding frequency, solution of the hot kinetic plasma dispersion relation Eq. (4.24), is $\omega_0 = 0.2995\Omega_p$. The number density for the alphas was $n_\alpha/n_e = 0.05$. The isothermal massless fluid electrons were supposed to be warmer than the ions, $\beta_e \equiv 4\pi n_e \gamma_e k_B T_e/B_0^2 = 0.5$. The number of particles per cell was 400 for each species, the grid points were 2048 and the total number of iterations was set to 65536. The pump wave amplitude was set to $a_0 = \delta B/B = 0.25$ and only parallel propagation was considered. As one of the aims is to show the origin of the differential streaming, no relative drifts were initially assumed. Both ion distributions were chosen to be initially isotropic Maxwellians with a different bulk drift in perpendicular direction, imposed by the presence of the nonlinear pump as discussed in Chapter 4.

The first snapshots on the left-hand side of Fig. 5.1 confer that the protons were initiated at

a higher plasma $\tilde{\beta}$ than the alphas. In addition the alphas are more prolonged in perpendicular direction due to their higher apparent anisotropy (see section 4.2 of the previous chapter). In the course of evolution each particle moves around in the constant external magnetic field, the electromagnetic field caused by the other particles and the electromagnetic field of the external wave, thus slowly increasing the thermal noise in the system. At some point the pump wave couples to the thermal fluctuations and a series of parametric instabilities occur, giving birth to a spectrum of both daughter electromagnetic (transverse) and IAW (longitudinal) waves. Depending on the type of instability the daughter IAWs have different phase speeds. The modulational instability leads to growth of IAWs with phase speed larger than the thermal speed of the particles, $v_{\text{ph}} = \omega/k > v_{\text{th}}$, whereas the decay-like instabilities result in daughter IAWs with $v_{\text{ph}} \sim v_{\text{th}}$. When the daughter IAWs fall into resonance with the particles of a given species, the latter are accelerated (or slowed down) via Landau damping. As the modulational instability generates fast daughter IAWs (the first acoustic peak to the left of the pump on Fig. 5.8), which fall in resonance with particles from the tail of the proton VDF, it leads to the formation of a prominent, though tenuous proton beams, as visible on the last snapshot of Fig. 5.1 at time $t = 553\Omega_p^{-1}$. On the contrary, the decay-like instability (the second acoustic peak after the pump on Fig. 5.8) acts more on the bulk of the proton distribution and therefore it leads to the formation of denser beams, which travel relative to the core at much lower drifts, than the fast beams, resulting from the modulational instability. The IAWs from both instabilities affect both particle species, but the larger mass of the α particles may make their beam formation weaker.

As the instabilities take place, the initial pump starts to deplete, and at $t > 400\Omega_p^{-1}$ it no longer dominates the system. This causes the initial perpendicular drift for both species to diminish and the apparent anisotropies, due to the initial coherent motion, disappear. Diffusion in phase-space takes place and real heating occurs. Once the α particles are initially heated like this they can also fall in resonance with the daughter IAWs and acquire additional parallel heating as visible on Fig. 5.2.

Fig. 5.2 shows the nonlinear evolution of the 3D ion distributions, when the daughter waves grow strong enough to compete with the pump and the linearized parametric instability theory no longer holds. We can see that in the nonlinear stage (at times $t > 400\Omega_p^{-1}$), the Landau damping of the daughter IAWs proceeds and the proton beam continues to grow. In the meantime, the protons from the core fill in the phase-space between the core and the beam, so that in the end the proton species are parallelly heated as a whole, though the core itself is slightly prolonged (i.e. heated) in transverse direction. At late times, $t > 1000\Omega_p^{-1}$, the α particles also start to resonate with daughter IAWs, accelerate in parallel direction and start to form a beam. Still, the parallel heating for the alphas in this case does not prevail, and the entire population as a whole remains preferentially heated in perpendicular direction. Similar to what is observed in the fast solar wind, the bulk of the α particles “lay” between the proton core and beam.

To extract easier the information about the plasma heating and acceleration hidden in the distribution functions, we may take a look at their bulk moments, like ion drifts and kinetic temperatures. Fig. 5.3 shows the evolution of the parallel relative drift speed between protons and α particles in the course of simulation. Initially we start with zero drifts along the external magnetic field lines, i.e. the bulk of the particles for each species stays at rest and the only motions come from the thermal noise and the perpendicular drift

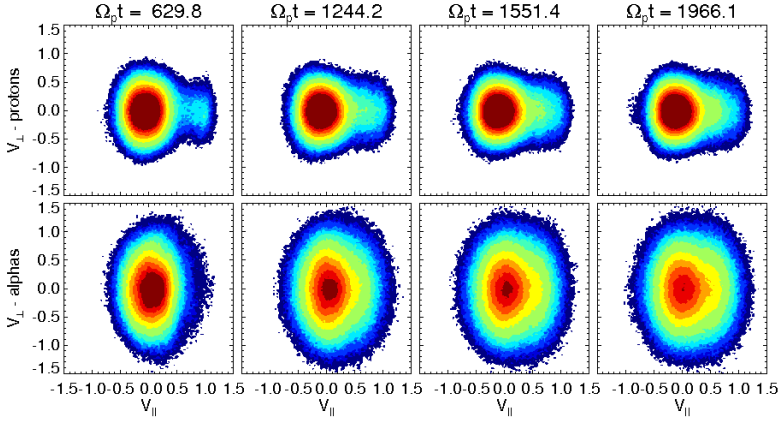


Figure 5.2: The same contour plots with 3D distributions as on Fig. 5.1, but at later time, during the nonlinear stage of the simulation. The figure shows continuous heating and acceleration for the protons, which keep on the beam formation via absorption of IAWs and additionally start filling in the phase space between the core and the beam. At this later stage the alphas have warmed up gradually and also start to fall into resonance with the IAWs and be accelerated in parallel direction.

imposed by the presence of the pump wave (see Eq. (4.26)). Due to this perpendicular drift, the parallel velocity also starts to oscillate as the transverse and the parallel motions are not independent. With the decay of the pump, the transverse drift diminishes and the oscillations of the parallel drift damp out. Due to the Landau damping the ions get accelerated (the alphas preferentially) and the relative drift starts to increase (at about $t > 250\Omega_p^{-1}$). After 500 gyroperiods nonlinear regime is reached and the alphas keep on being accelerated, so that at the end of the simulation their differential streaming reaches a substantial fraction of the local Alfvén speed, $V_{ap} > 0.15V_A$.

Fig. 5.4 shows the evolution of the ion temperature anisotropy for protons (in yellow) and α particles (blue lines). Initially the simulation was initialized with isotropic Maxwellian distributions for both ion species. The apparent anisotropies and their oscillation (much more visible in the α distributions) come from the bulk transverse motion in the presence of the pump, as discussed in section 4.2 of Chapter 4. With the depletion of the pump and the growth of the daughter waves, the apparent anisotropy decreases and the oscillations damp out until a saturation is reached in the nonlinear regime, at the late stage of the simulation. The figure shows that the bulk of the protons is slightly preferentially heated in parallel direction, whereas the alphas acquire preferential transverse anisotropy. This result is supplemented by figure 5.5, which shows the temporal evolution of both parallel and perpendicular components of the kinetic temperature for both ion species. The sharp initial increase in the perpendicular temperature of the α particles and its oscillations, just like the plot with the anisotropy, is due to the electromagnetic field of the pump. As it

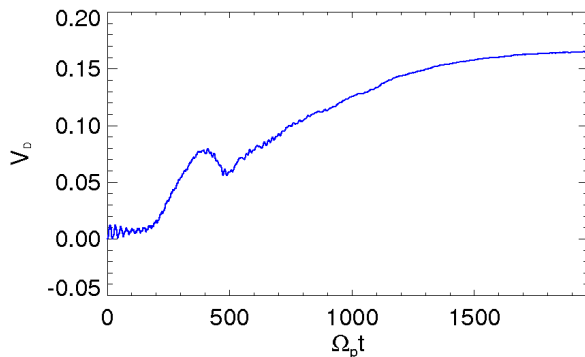


Figure 5.3: Parallel relative drift between protons and α particles as a function of time, showing the origin and growth of differential streaming. The initial oscillations are caused by the initial large-amplitude Alfvén-cyclotron wave. They disappear as the pump wave depletes and the α particles start to accelerate.

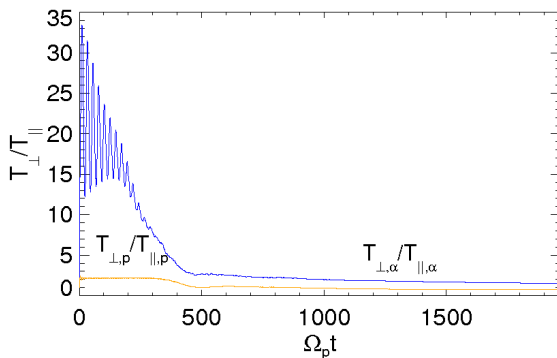


Figure 5.4: Temporal evolution of the kinetic temperature anisotropy for protons (yellow lines) and α particles (blue lines). Similar to Fig. 5.3, the initial oscillations are due to the presence of the pump wave and they vanish as it depletes.

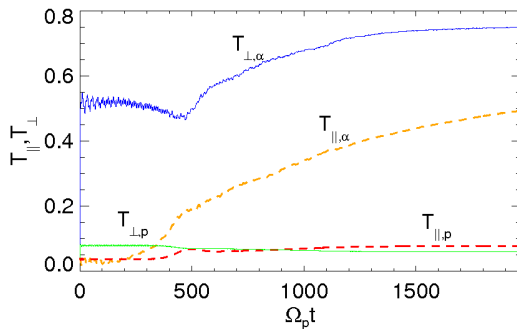


Figure 5.5: Simulated temperature profiles for protons and α particles. The parallel and perpendicular components with respect to the external magnetic field are plotted as a function of time.

depletes the amplitude of the oscillations decreases and the particles start to diffuse and fill in the phase-space occupied during the oscillations of the entire distribution function in the presence of the pump. In this way effective heating occurs and after $t \sim 500\Omega_p^{-1}$ the high perpendicular temperature is no longer the apparent one. The plot shows that simultaneous with the pump depletion due to parametric decays, the parallel temperature of both protons and α particles increases, though to a different amount. This means that the protons and the α particles fall into Landau resonance with different daughter IAWs. As we will see on Fig. 5.6, the proton beam in this case is formed due to a fast ion-acoustic wave, traveling with a phase speed of about $v_{ph} \sim 0.7V_A$. As there are no α particles moving at that high speed, the alphas do not show signatures of trapping, hence in parallel direction they are probably heated by scattering from a bunch of slower ion-acoustic waves, which do not affect the more abundant protons, but are strong enough to heat and accelerate the minor α species. We should note that a group of large-amplitude IAWs might not lead to formation of phase-space holes, unlike in the presence of a single large-amplitude monochromatic wave and hence the alpha particles in this case would not exhibit trapping, but rather be squashed in the electric field of the daughter waves. The proton beam starts to form later (see Fig. 5.1) and they are getting parallelly heated once a fast daughter IAW, which resonates with particles on the tail of the proton distribution, is generated by the parametric decays. The perpendicular temperature of the protons stays almost unchanged, while the perpendicular heating of the alphas up to 500 gyration periods is due to the non-resonant pitch-angle scattering and diffusion, that occur together with the generation of the electromagnetic micro-turbulence and the depletion of pump. Afterwards, at $t > 500\Omega_p^{-1}$, the slight additional heating is due to cyclotron resonance of the α particles with daughter Alfvén-cyclotron waves.

Fig 5.6 shows a partial phase portrait of protons and alpha particles. It plots the parallel ion velocities versus their position. We can observe the trapping of protons in the wave potential of fast daughter IAWs with a phase speed of $v_{ph} \sim 0.7V_A$, denoted by the charac-

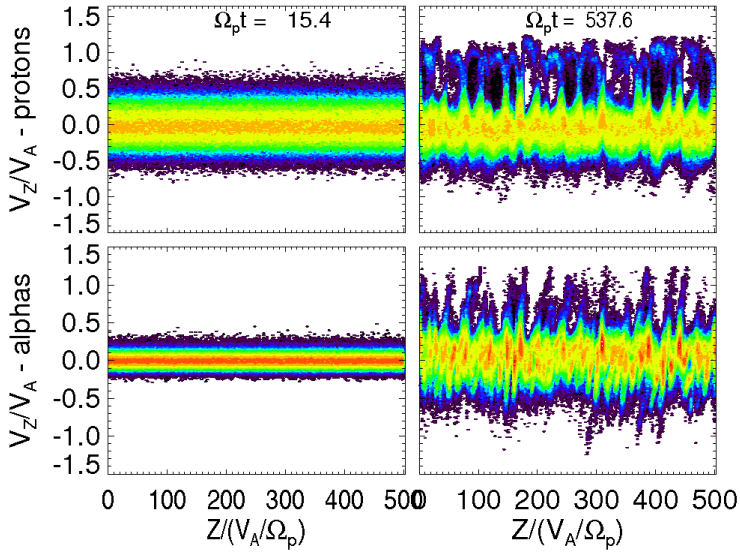


Figure 5.6: Parallel velocity of protons and α particles versus position at two different times. The left side of the figure shows the very early distributions (the first phase-space snapshot after the beginning of the simulation) with warm protons and colder α particles. The right side demonstrates the trapping of protons at later time, when the parametric instabilities gave birth to a fast large-amplitude resonant daughter IAW. Due to their lower initial plasma β and larger mass, the alphas appear initially colder and do not fall in the wave’s potential well. Note that, for the sake of clarity, the userlines for the initial alpha distribution are twice enhanced in comparison to the rest of the plots.

teristic phase-space holes. Consequent Landau damping results in formation of a proton beam, traveling close to the local Alfvén speed (as visible on fig. 5.1 as well). Due to the total momentum conservation, the bulk of the alphas has parallel velocity, ranging in between those of the proton core and beam. We should note, however, that apart from the plasma β , the trapping also depends on the relative drifts between the ion species. Thus, if we initialize a simulation with a relative drift about $V_{\alpha p} \sim 0.4V_A$, with the rest of the initial conditions staying the same, the alphas can be trapped as well and form beams from the front tail of their distribution. As we increase the initial relative drift we can trap either the whole the alpha population, for $V_{\alpha p} \sim 0.6V_A$, which results in a strong heating in parallel direction or form inverse beams by trapping alpha particles from the back side of their distribution as $V_{\alpha p}$ approaches $0.9V_A$. Fig. 5.7 shows an example of such a trapping for the alpha particles, related to an inverse beam formation. The same daughter IAWs simultaneously trap the protons from the tail of their velocity distribution function, so that they form a normal beam, oriented along the direction of the magnetic

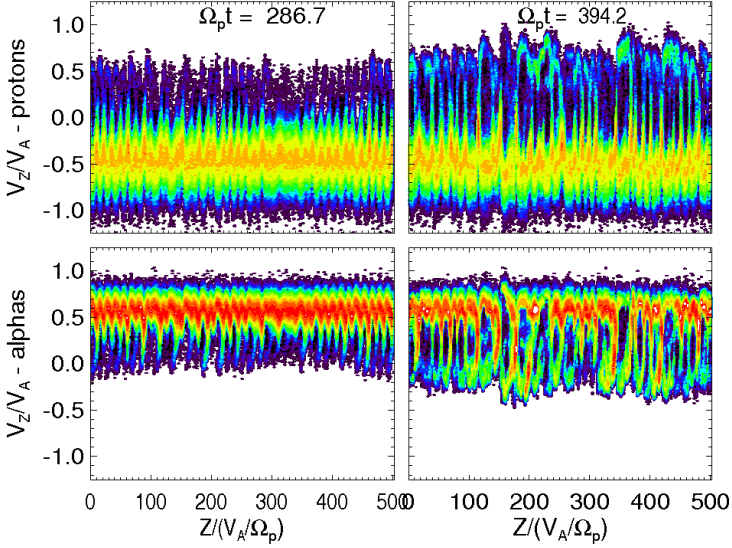


Figure 5.7: Simultaneous trapping of protons and inverse trapping of α particles in the potential field of intense daughter IAW with a phase speed of about $v_{ph} \sim 0.25V_A$. The simulation was initialized with a relative drift $V_{\alpha p, in} = 1V_A$. All the plasma parameters, the pump wave amplitude and the pump wave wave-vector were kept the same as in Fig. 5.6, only the pump wave frequency was changed according to Eq. (4.24).

field lines. More details on the evolution of ion distributions when a differential streaming of different magnitude exists in the system will be presented in the next section.

Fig. 5.8 shows the evolution of the square of the magnetic field and density fluctuations in Fourier space at different times during the same simulation run as on Figs. 5.1 to 5.6. The plots show the development of parametric instabilities when the mother Alfvén-cyclotron wave couples to the thermal fluctuations in the system. We can follow the growth of both strong decay-like and modulational instabilities. The decay is associated with the first peak on the left-hand side of the electromagnetic spectrum given in grey and the second peak of the acoustic spectrum painted in black, well visible on first and second plot during the early stage of the simulation. The modulational instability is related to the somewhat smaller amplitude electromagnetic peaks on both sides of the pump (at mode 32) and to the first peak in the density fluctuations, leftward from the pump. This instability generates fast daughter IAWs, with a phase speed $v_{ph} \sim 0.7V_A$, which trap the protons on Fig. 5.6. They are responsible for the parallel heating and initiate the differential streaming. The third peaks both in the magnetic and the acoustic spectra are probably due to a beat instability. As we advance the system in time both spectra steepen and an inverse cascade is observed. At late times, during the nonlinear stage of the simulations, there is an interplay between the modulational and the decay-like instabilities, as visible on

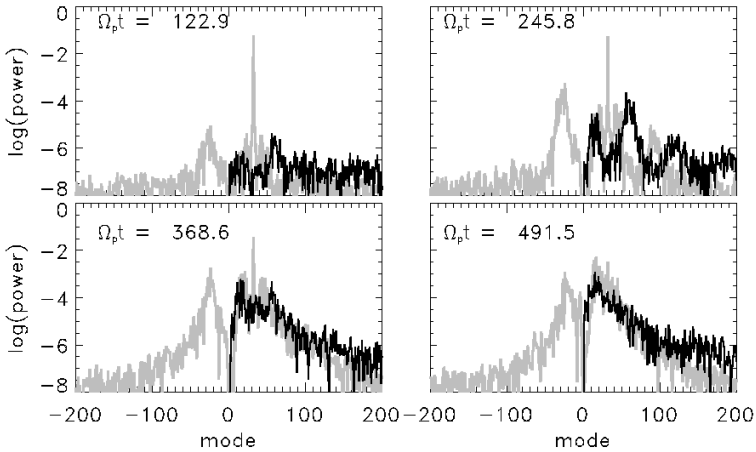


Figure 5.8: Snapshots with the power spectra of the daughter electromagnetic and IAWs, generated during the parametric decay of the initial Alfvén-cyclotron pump wave (drawn by the sharp peak at mode 32). The plots show the square of the Fourier transform of the magnetic field (given in grey) and density fluctuations (in black), normalized by the magnitude of the external magnetic field and the number density of protons, respectively. The plot demonstrates the parametric instabilities at the early stage of the simulation and the formation of both electromagnetic and acoustic micro-turbulence.

Fig. 5.9. The first one generated IAWs, which trap and accelerate the ions, whereas the second produces daughter Alfvén-cyclotron modes, which do pitch angle scattering on the front side of the proton beam and on the back of the alphas velocity distribution function, leading to plateau formations, whose signatures can be found on Fig. 5.2.

From all the plots above we can conclude that, if present in the system, high-frequency nonlinear Alfvén waves (with frequencies somewhat lower than the gyrofrequency of the heaviest ion species considered) can accelerate and heat the fast solar wind plasma (preferentially the minor ions), initiating differential streaming, temperature anisotropies and ion beam formations. This may explain the non-thermal features, observed in CHs and the fast solar wind. Those results were recently discussed and presented by [Araneda *et. al.* (2009)].

5.3 Heating and acceleration in the presence of relative drift

The previous section demonstrates how preferential heating and differential streaming can be generated. This section will provide several examples for the behavior of protons and

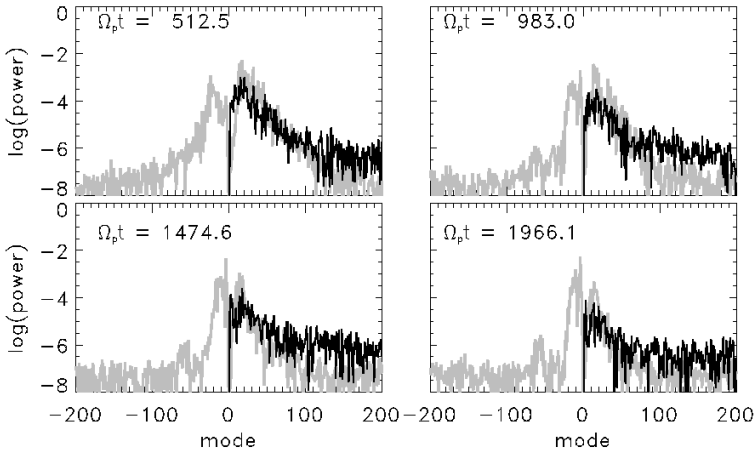


Figure 5.9: Evolution of the power spectra of the daughter electromagnetic and IAWs at later times, when the initial pump does no longer dominate the plasma motion.

alpha particles when a relative drift is initially inserted in the system. When present, the relative drift influences both the parametric decays and the apparent anisotropies of the ions (according to Eq. (3.53), Eq. (4.25) and Eq. (4.26)). It enhances the level of the acoustic fluctuations and can either facilitate the parametric instabilities and make them occur at an earlier stage, or it may form a quasi-stabile system, where the beginning of the wave-wave couplings is delayed. This reflects on the ion trapping, heating and their differential acceleration, as we will see from the upcoming figures below.

As we initialize the simulations with different values of the initial differential streaming, we can generally encounter 3 different situations. The first one corresponds to the case when the initial relative drift increases in the course of the simulation. The second is when the relative drift is preserved, and the third case is when the α particles are slowed down and the differential streaming decreases in the course of evolution. In our virtual experiments, in addition to these three cases, we encounter another situation, where the initial relative drift does not decrease at once, but there exists a short initial stage during which the differential streaming is conserved, before a nonlinear analogue of the magnetosonic instability sets in to reduce it. For the given choice of initial parameters ($n_\alpha/n_e = 0.05, \beta_p = 0.08, \beta_\alpha = 0.02, k_0 = 0.4\Omega_p/V_A, \beta_e = 0.5, a_0 = 0.25$, 400 particles per cell and 2048 grid points) and assuming isotropic distributions at the beginning, the different regimes look like this: for $V_{\alpha p, \text{in}} \in [0, 0.5V_A)$ the relative drift keeps on gradually increasing during the simulation run. For $V_{\alpha p, \text{in}} = 0.5V_A$ the differential streaming at the beginning and the end of the run stays practically unchanged. For all simulations with $V_{\alpha p, \text{in}} > 0.5V_A$ the initial drift decreases at the end of the runs. This last case is, however further divided into 2 different subcases. For initial drifts in the range

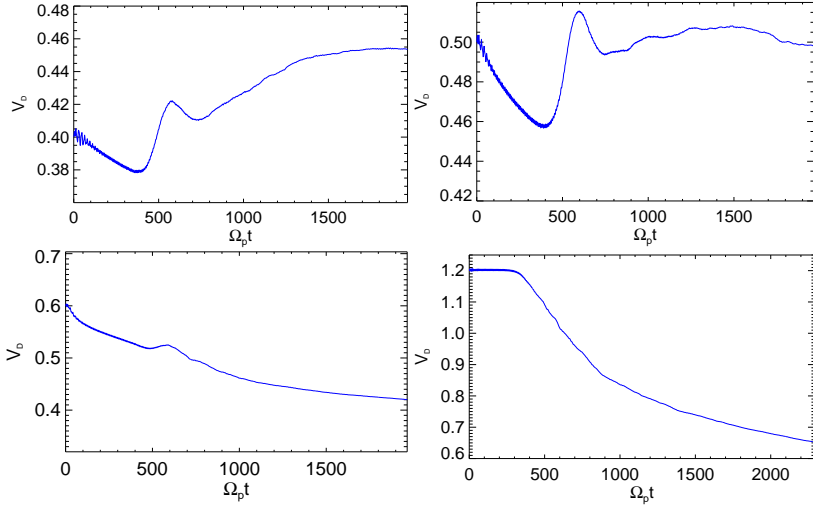


Figure 5.10: Relative drift speeds between protons and α particles for the 4 representative regimes described in the text. All values are normalized to the Alfvén velocity, set by the magnitude of the homogeneous background magnetic field.

$0.5V_A < V_{ap,in} < 0.9V_A$, the relative drift simply decreases in time. From $V_{ap,in} = 0.9V_A$ on till $V_{ap,in} = 1.8V_A$ (the last value for our analysis), we observe a short initial stage, typically between 300 – 350 proton gyroperiods, where the ion drifts remain stable. Thus we have in total 4 qualitatively different initial relative drift regimes, which have been illustrated on Fig. 5.10. The figure displays the time evolution of the relative drift velocity between protons and the α particles during the simulation run. It plots one representative example for each of the four regimes, described above, with an increasing value of the initial relative drift from top left to the bottom right. We can see that for $V_{ap,in} = 0.4V_A$ the relative drift at the end of the simulation keeps on increasing, whereas for $V_{ap,in} = 0.5V_A$ it is quasi-conserved. For $V_{ap,in} = 0.6V_A$ the drift gradually decreases all the time and for $V_{ap,in} = 1.2V_A$ the relative drift in the first 350 proton gyroperiods is conserved. This is the linear stage of the simulation, after which daughter waves (predominantly left-hand polarized modes) start to grow as visible on Fig. 5.13 and Fig. 5.14. It means that initially the particles are simply streaming at a constant relative drift, but once the pump wave starts to decay the α particles are being slowed down by the daughter IAWs, which simultaneously accelerate the protons. That is the reason for the proton beam and the inverse alpha beam formation in the ion distribution functions, as visible on Figs. 5.22 and 5.23. Then the relative drift between the two species naturally decreases. In this case the α particles also decelerate due to a pitch angle scattering by the backward propagating daughter Alfvén-cyclotron waves and quasilinear plateaus are formed, particularly prominent at the back side of their distribution (look at Fig. 5.22).

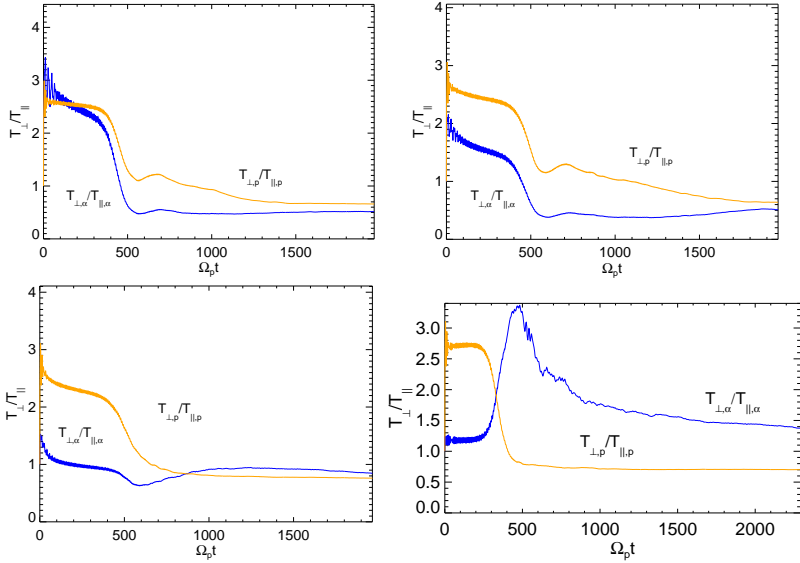


Figure 5.11: Temporal evolution of the ion anisotropies for protons and α particles for the selected examples of the 4 initial relative drift regimes, described above. The initial parameters are the same as in Fig. 5.10.

We should say that the transition between the third and the fourth regimes in the space of initial relative drift values depends on the individual bulk speed of the ions (whose difference sets the value for the relative drift) and the phase speed of the pump wave. All the first, second and third regimes occur when the phase speed of the mother Alfvén-cyclotron wave is larger than the individual bulk velocity of both species, i.e. $v_{\text{ph}} > V_p, V_\alpha$, where V_p and V_α are the first moments of the velocity distribution functions for the protons and for the α particles, respectively. The fourth regime, then, occurs when, for any reason, the alphas stream faster than the phase speed of the pump, $V_\alpha > v_{\text{ph}}$. The more the bulk speed of the α particles exceeds the phase speed of the pump wave, the longer the partial stabilization of the initial drift holds. We should note that in this situation if we move to the α particles reference frame, the waves will appear as backward propagating, whereas from the point of view of the protons they will still be spreading forward. This means that the protons and the α particles in this case will be out of phase. In the center of momentum framework for a given relative drift, the alphas stream faster and the protons move slower, being pushed in the opposite direction due to the conservation of total momentum. Thus, according to Eq. (4.26) the presence of drifts substantially reduces the initial anisotropies of the alpha particles, as illustrated below.

Fig. 5.11 shows the change in the evolution of the ion anisotropies with the increase of the initial relative drift. The snapshots are taken for the same initial conditions as on Fig. 5.10, the plots corresponding to $V_{\alpha p, \text{in}} = 0.4, 0.5, 0.6$ and $1.2V_A$, from top left to bottom right,

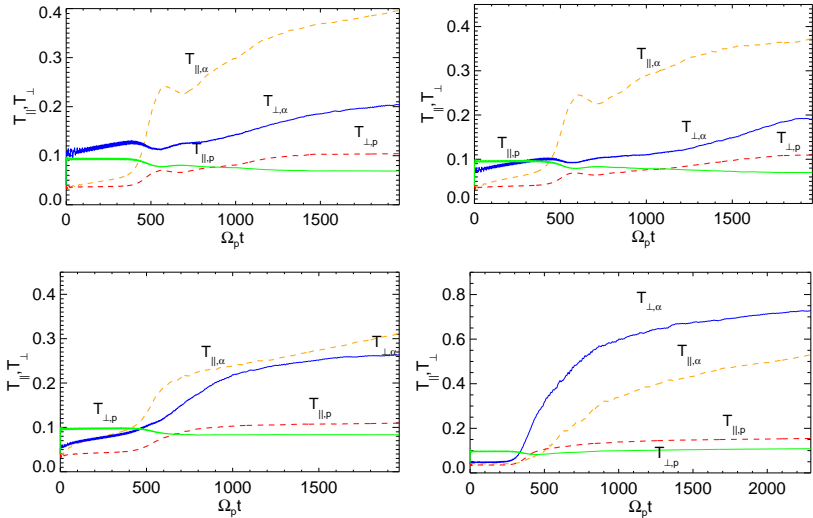


Figure 5.12: Parallel and perpendicular components of the kinetic temperatures for protons and α particles for the same initial conditions as on Fig 5.10. Note the completely different behavior of the perpendicular temperature of the α particles, suggesting that different heating processes operate at the 4 different initial drift speed regimes.

respectively. We can see that for $V_{\alpha p, \text{in}} = 0.4V_A$, the apparent anisotropy for the alphas is higher, but it decreases as we increase the relative drift, when the protons get relatively more influenced by the wave (in comparison to the alphas). The drop in the anisotropy for both species, visible on the first three plots at $V_{\alpha p, \text{in}} = 0.4, 0.5$ and $0.6V_A$, coincides with the decay of the pump wave, initially forcing the perpendicular bulk drift of the species and inducing the apparent anisotropies. Simultaneously at this stage heating occurs and afterwards, we can only speak of “real” and not any more “apparent” anisotropies. The peak of the alpha anisotropy around $450 \Omega_p t$ on the last plot (made for $V_{\alpha p, \text{in}} = 1.2V_A$), is due to the strong and continuous perpendicular heating of the α particles, better visible on Fig. 5.12.

The change in the initial relative drift reflects also on the perpendicular temperature components for both ion species. All simulations were initiated with initially isotropic drifting Maxwellian distributions with an additional perpendicular drift, imposed by the magnetic field of the pump wave (see Eq. (4.26)). As the moments are collected after the first simulation iteration, this perpendicular motion enhances the perpendicular components of the ion kinetic temperatures and results in an increase of the initial perpendicular temperatures, visible in the ion temperature profiles Fig. 5.12. The initial parallel temperature is entirely determined by the initial value of the parallel plasma $\tilde{\beta}_s$ for the given ion species and hence, does not depend on changes in the initial relative drift. The perpendicular temperature, however, is a sum of the initial value of the parallel plasma $\tilde{\beta}$ (as initially

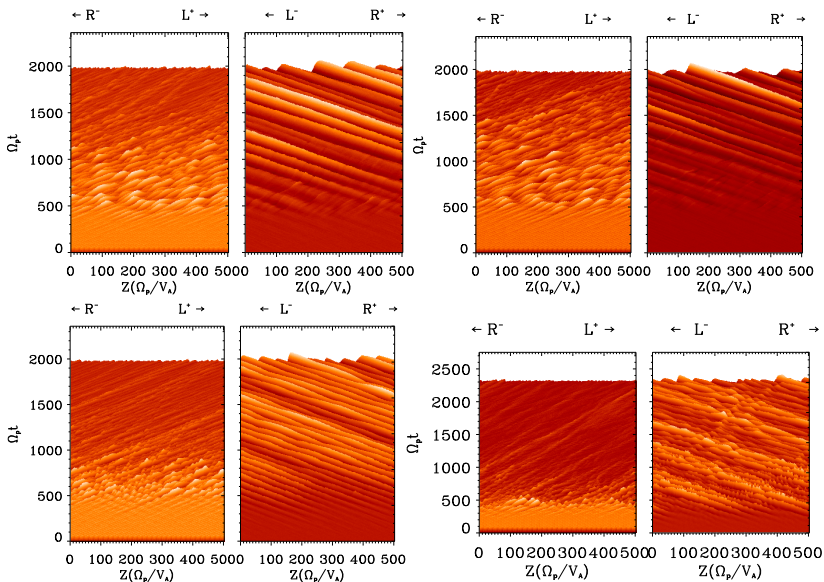


Figure 5.13: Shade-contours with the profile of the magnetic fluctuations in time versus the real space coordinate. The plots are grouped into two and show the relative amplitudes, polarization and wave propagation for the 4 different initial relative drift cases as shown on Fig. 5.10.

isotropic distributions are assumed) plus the normalized square of the pump-wave induced perpendicular drift and hence it implicitly depends on the value of the initial relative (parallel) drift $V_{ap,in}$. That is why for $V_{ap,in} = 0.4V_A$ the initial perpendicular temperature for the alpha particles is highest. As we increase $V_{ap,in}$, the protons response to the Lorentz force of the pump wave becomes stronger and their apparent initial perpendicular temperature exceeds that of the alphas, as seen on the last 3 plots of Fig. 5.12. The figure shows strong parallel heating for all cases and relatively increasing perpendicular heating with an increasing value of the initial relative drift speed. The little bumps at $\Omega_p t \sim 600$ in the parallel temperature for both species (better visible for the α particles, though) in the first two plots correspond to waves emission and associated cooling. Increased activity of the forward propagating left-hand daughter modes at this time can be seen on Fig. 5.13.

To better visualize the outcome from the parametric instabilities and the waves activity as a whole, one can look at the growth of the daughter electromagnetic waves in space and time. Fig. 5.13 reveals the evolution of the transverse daughter waves, depending on their polarization (L for left-handed modes and R for right-hand polarized ones) and orientation (forward or backward propagation, indicated with the arrows). To make the plot easier to read only the relative wave amplitude is given. The relative wave power can be extracted from Figs. 5.14 and 5.15. The average simulated time is about 2000 proton gyroperiods

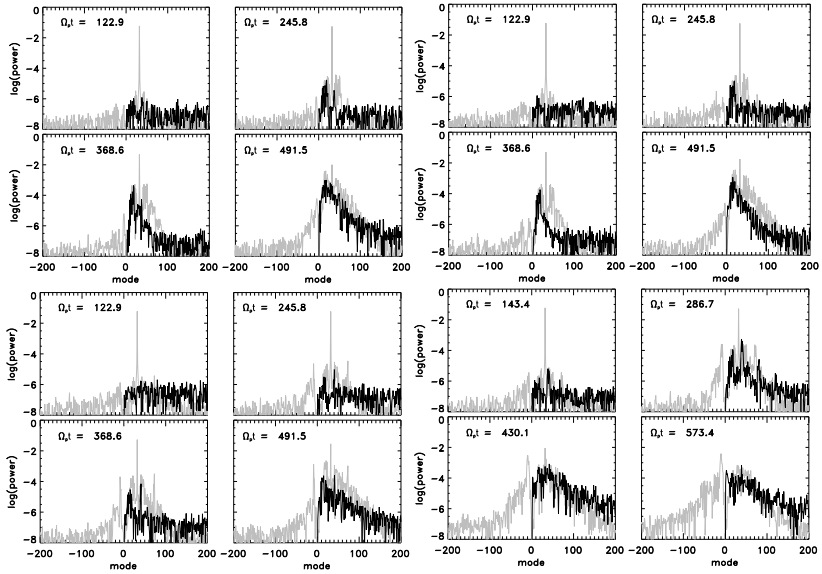


Figure 5.14: Power spectra of the Fourier-transformed magnetic field and density fluctuations at different times during the simulations. The 4 panels from left to right on the first and the second row correspond to the 4 values, chosen for the initial relative drift. Each panel additionally consists of 4 plots with snapshots of the power spectra at 4 different times. All plasma parameters were the same as on Fig. 5.10.

and the waves are propagating in the 1D simulation box with a length $z = 504V_A/\Omega_p$. The 4 grouped plots correspond to the same initial conditions as on Figs. 5.10-5.12 and the figure shows that there are almost only left-hand polarized waves propagating in the system for all values of the initial relative drift. At the early stage these modes propagate predominantly in outgoing direction, saying that they could have been born by modulational instability, whereas at the end of the simulation time Sunward propagation dominates, which is a typical signature for the decay-like instabilities.

Figs. 5.14 and 5.15 are complementary to Fig. 5.13 and similar to Figs. 5.8 and 5.9. Fig. 5.14 shows snapshots of the power spectra in wave-number space for the magnetic and density fluctuations at different times during the linear stage of the simulations, when the daughter waves are still growing. All conditions are the same as on Fig. 5.10 and the plots have been grouped in such a way, that for each value of the initial relative drift speed, 4 snapshots, showing the time evolution of the wave power, have been given. On the left and right panels on the first row, corresponding to $V_{ap,in} = 0.4$ and $0.5V_A$, the modulational instability dominates, therefore we can see predominantly forward propagating left-hand polarized waves on Fig. 5.13. The last two panels on the second row (corresponding to $V_{ap,in} = 0.6$ and $1.2V_A$) show signatures for decay-like instabilities as well

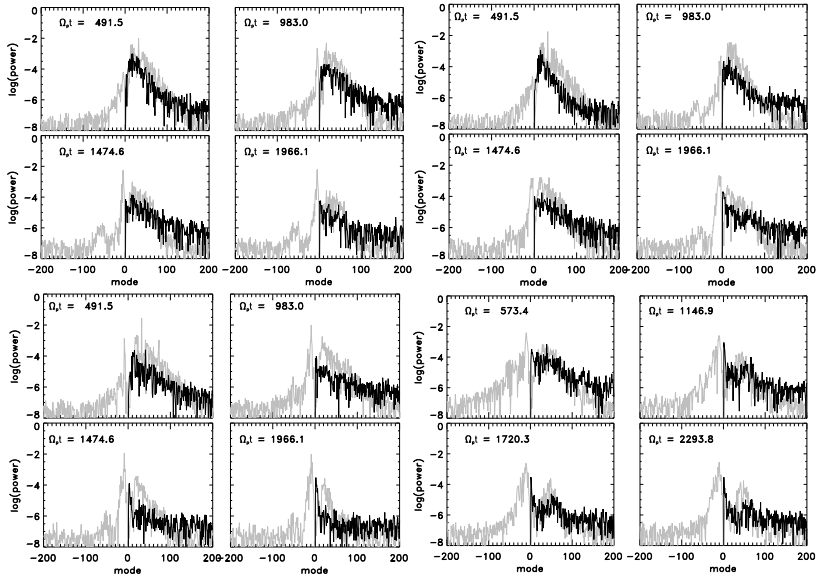


Figure 5.15: The same power spectra as presented on Fig. 5.14, but at later times for the nonlinear stage of the simulations.

and hence backward propagating waves are involved as well. Fig. 5.15 shows the same power spectra, but at the late, nonlinear stage of the simulations, when the mother wave has already decayed and the daughter fluctuations have grown stronger. At this stage for all initial relative drift cases we see the signatures for a decay-like instability, particularly strong (and involving wider range of wave-numbers) in the last two cases, for $V_{ap,in} = 0.6$ and $1.2V_A$, which determines the strong backward propagating left-hand waves at the late times of Fig. 5.13.

Figs. 5.16 to 5.23 show snapshots with the ion velocity distribution functions, corresponding to the same four initial relative drift regimes given above. Again, we can see the influence of the differential streaming on the initial apparent anisotropies of the ions and well as on their later evolution, regarding both parallel and perpendicular heating and beam formations. As mentioned before, the initial apparent anisotropies of the alphas tend to decrease with increasing values of the initial relative drift speed, therefore their initial distributions for large $V_{ap,in}$ look more isotropic. The apparent anisotropy for the protons for all simulated cases remains almost the same and their final anisotropy also does not change much.

If we were to look at the ion trapping (like on Fig. 5.7), we would see that for all the four representative cases both the protons and the alpha particles are being trapped in the wave potential of daughter IAWs with a phase speed of about $v_{ph} \sim 0.25V_A$. This reflects on the ion distributions and causes the prominent beam formations not only for the protons

(like in the case of non-drifting plasma, see Figs. 5.1 and 5.6), but for the α particles as well. Then, additionally, depending on the value of the initial relative drift, the α particles can be either accelerated in outward direction (when their initial parallel bulk speed is smaller than the phase speed of the pump wave in the center of momentum reference frame $V_\alpha < v_{\text{ph}}$), or they can be slowed down by the waves and start a relative motion backwards to the center of mass frame (when their initial parallel bulk speed exceeds the phase speed of the pump wave $V_\alpha > v_{\text{ph}}$). In both cases there is an accompanying prominent parallel heating associated with the acceleration process. The acceleration is related to the typical fast alpha beams (Figs. 5.16 – 5.21), whereas the deceleration leads to formation of slow inverse beams (Figs. 5.22 and 5.23). The core of the protons, on the other hand, always acquires small negative velocities in the center of momentum frame of reference, so that their bulk speed does not exceed the phase speed of the mother wave, i.e. $V_p < v_{\text{ph}}$ for all investigated values of $V_{\alpha p, \text{in}}$ (see Table 6.1 from the next Chapter 6), and hence their distributions exhibit only regular beams.

Signatures for the resonant absorption of daughter IAWs clearly reflect on the parallel heating for both species. As the alphas travel at a higher initial parallel drift speed, their bulk lays closer to the resonant condition and they get more heated and accelerated than the protons, whose beam forms from the few particles on the back of the velocity distribution. On the other hand, the α particles are much less abundant than the protons and that makes it easier for the waves to accelerate and heat many of them, without losing too much wave power. Another interesting feature in the distributions is the signature of quasi-linear diffusion plateau formations [Marsch and Tu (2001a); Marsch and Tu (2001b)], resulting from the pitch-angle scattering of ions by the forward and backward propagating left-hand polarized daughter Alfvén-cyclotron waves. Parts of the diffusion plateaus are visible both at the front and at the back side of the ion distribution functions.

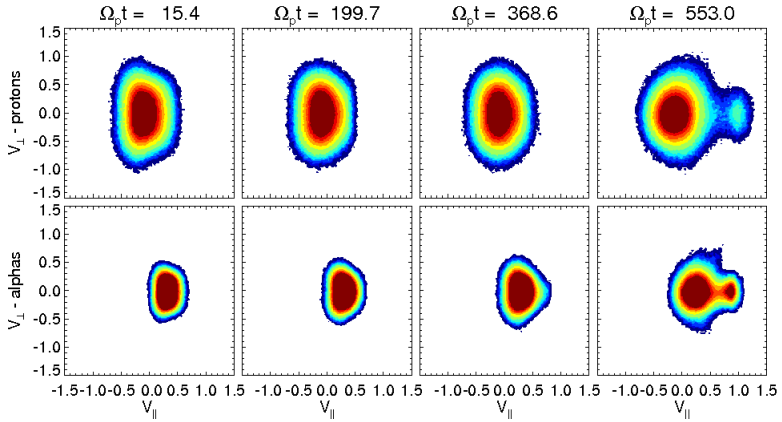


Figure 5.16: Early-time evolution of the velocity distribution functions for protons and α particles. The figure shows contour plots with snapshots of the ion distributions at 4 different times during the linear stage of the simulations. The colour shading denotes the number of particles of the given specie, with a fixed parallel and perpendicular velocities, drawn respectively along the abscisa and the ordinate. Similar to Fig. 5.1, the maximal counts are given in dark red and the dark blue represents only a few percents of the total number density for the given specie. This simulation corresponds to $V_{\alpha p, \text{in}} = 0.4V_A$ and all the other plasma parameters were the same as on Fig. 5.10

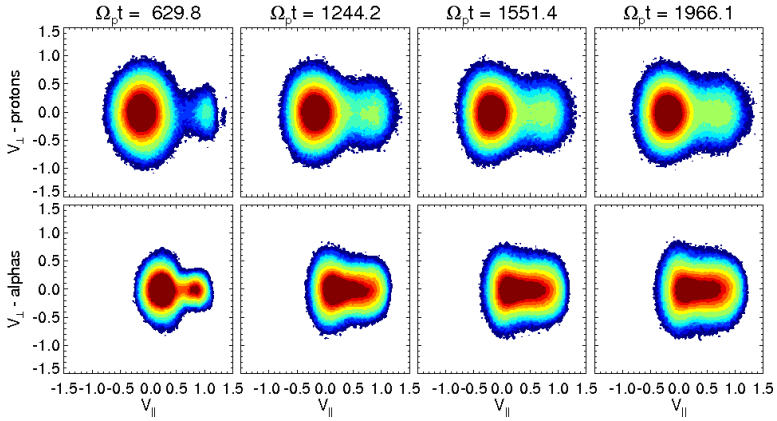


Figure 5.17: Late-time evolution of the same velocity distribution functions, presented on Fig. 5.16. At this stage a great percentage of the α particles get accelerated, resulting in an increase of their bulk drift speed and a strong parallel heating, as visible on Fig. 5.10 and 5.12. Strong ion beams for both species are persistently present for at least 1500 proton gyroperiods.

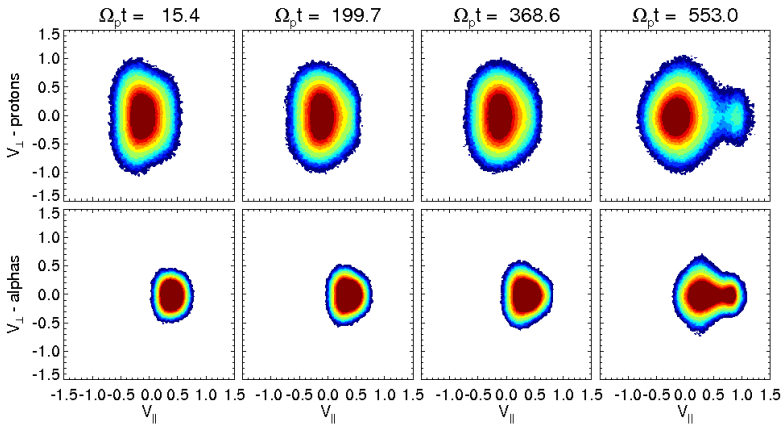


Figure 5.18: Early-time evolution of the VDFs for protons and α particles for $V_{\alpha p, \text{in}} = 0.5V_A$. Increasing the initial relative drift leads to a decrease in the apparent anisotropy for the alphas, therefore their initial distributions get closer to circular. Since similar daughter waves are excited the behavior of both species remains practically the same as the VDFs shown on Fig. 5.16. Only the alpha beam on the last panel is a little bit stronger.

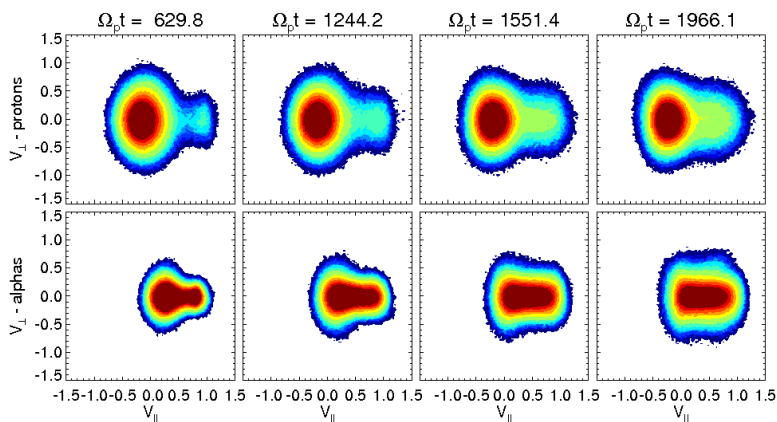


Figure 5.19: Late-time evolution of the VDFs shown on Fig. 5.18. There are strong beams for both protons and α particles, which in the case of the alphas merge with the bulk of the population to form a prolonged distribution and result in a substantial parallel heating.

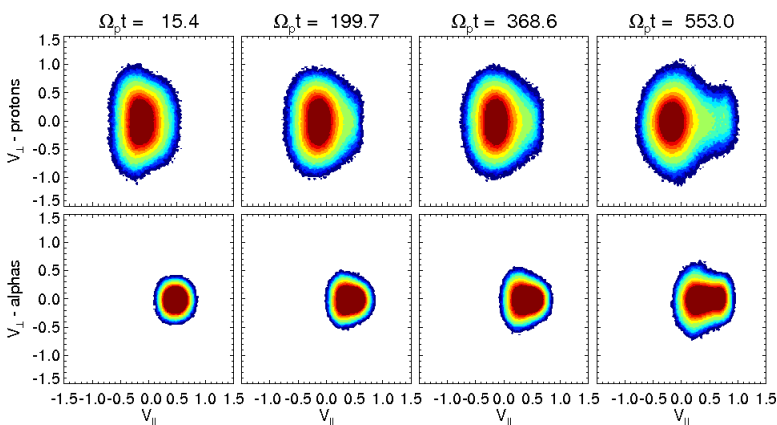


Figure 5.20: Early-time evolution of the VDFs for protons and α particles for $V_{\alpha p, \text{in}} = 0.6V_A$. The apparent anisotropy for the alphas continue to decrease. Proton beams are still formed and the α particles are parallelly heated, however this time the latter are slowed down and do not exhibit real beams, but rather the whole population of α particles is being trapped in the wave potential of the daughter IAWs, whose phase speed is close to the bulk speed of the alphas, so that the α particles get heated on both sides.

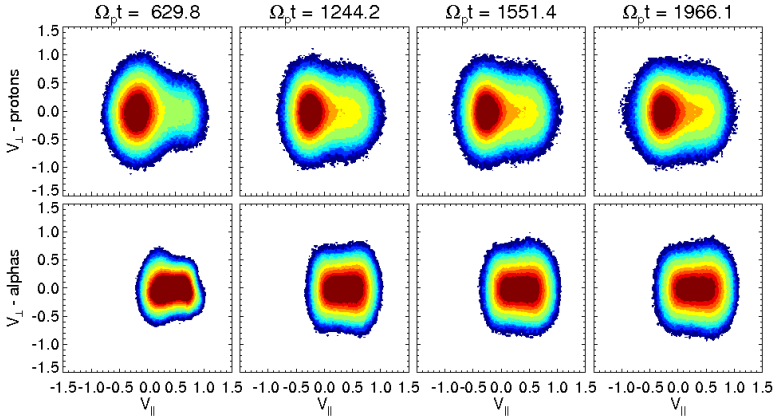


Figure 5.21: Late-time evolution of the VDFs from Fig. 5.20, showing the continuous increase of both parallel and perpendicular temperatures, particularly for the α particles. The proton beam grows stronger, constantly fed up by the wave power of the resonant IAWs.

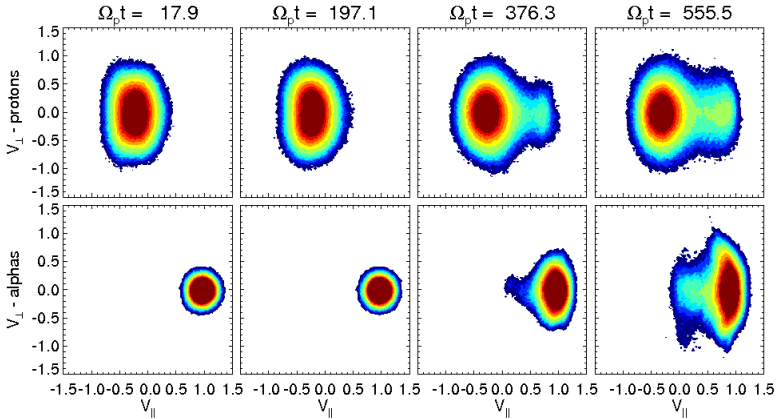


Figure 5.22: Early-time evolution of the VDFs for protons and α particles for $V_{\alpha p, in} = 1.2V_A$. The apparent anisotropy for the α particles as seen on Fig. 5.11 is very small and their initial distributions look isotropic. As the protons are slightly accelerated, the α particles slow down, while both species fall in resonance with the daughter IAWs. Since the phase speed of the resonant waves in this case is smaller than the bulk speed of the alphas, the latter are decelerated and form an inverse beam of slower α particles. In the same time the protons are accelerated and form the usual fast beam.

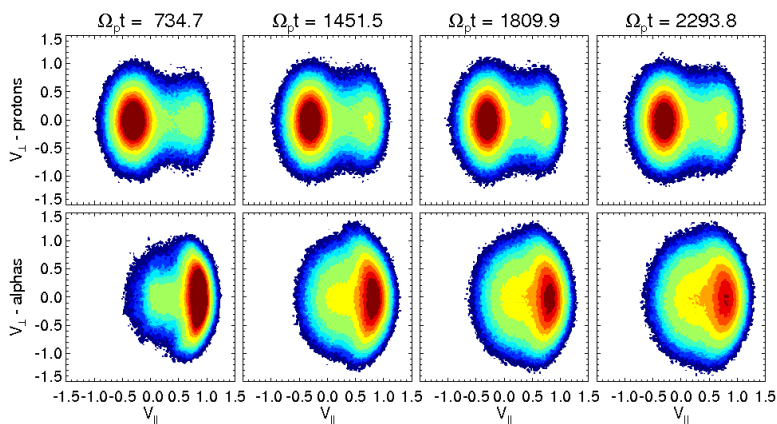


Figure 5.23: Late-time evolution of the VDFs from Fig. 5.22. Both α and the proton beams are continuously fed up by the waves. Together with the parallel one a strong perpendicular heating for the α particles is observed, which is probably associated with a cyclotron resonance by strong daughter Alfvén-cyclotron waves. Like on the rest of the figures above, both sides of the distributions for both particles species are shaped by the spectrum of the daughter ion-cyclotron waves. The ions seem to follow different quasi-linear plateaus, depending on the phase speed of the associated resonant cyclotron waves.

A different way to visualize the parallel heating and the ion beam formations is to look at the space-averaged 1D distribution functions, counting the number of particles at a given velocity in parallel direction, as presented on Fig. 5.24 and its complementary Fig. 5.25. Fig. 5.24 shows the initial and final states of the 1D ion distributions. From the difference of the full widths at half-maximum of the initial and the final distributions we can derive information about the parallel heating for both ion species. The secondary peaks at the end of the evolution represent the final state of the accelerated beams. We can see that the protons clearly form strong beams (about 10% of the core goes into the beam) for all 4 initial relative drift conditions, whereas an inverse beam in the distribution of the α particles is visible only for the high-relative drift regime $V_{\alpha p, \text{in}} = 1.2V_A$. In the other cases the alphas at the end appear just parallelly heated. If we take a look at Fig. 5.25 though, we can see that in the course of evolution the α particles do form ion beams, which, however, later connect to the core, resulting in a net parallel heating. Fig. 5.25 includes snapshots with intermediate stages from the evolution of the 1D ion distributions. There it is possible to see that in the first 2 cases of $V_{\alpha p, \text{in}} = 0.4V_A$ and $0.5V_A$, alpha beams were formed as well, but by the end of the simulation time more and more particles were accelerated by the waves, so that the alpha distribution in the end forms a small plateau as in the case of $V_{\alpha p, \text{in}} = 0.6V_A$. We should note that in most of the analyzed cases the formed ion beams are rather persistent and therefore stable with respect to the bump-on-tail instability. In some cases this is due to the low number densities of the beams and in general it is due to the fact that the electromagnetic ion-beam plasma instabilities can be stabilized in the presence of nonlinear Alfvén-cyclotron waves [Gomberoff (2003); Araneda and Gomberoff (2004)].

We may wonder what would happen if we further keep on increasing the magnitude of the initial relative drift. Then we reach a regime with more or less a stable pattern, where the drift speed is quasi-conserved for a relatively short time during the simulation run (in the first 300 to 500 proton gyroperiods) and later on starts to sharply decrease with an associated increase of the parallel temperatures for both protons and α particles (much higher for the alphas though). The results are shown on Figs. 5.26 – 5.28. We can see that the deceleration of the α particles is related to a strong heating, preferentially in parallel direction. The bumps in the parallel temperature follow nicely the associated patterns in the relative drift, suggesting absorption of IAWs, whose energy source comes from the relative drift motion. There is a short emission stage, indicated by the trough of the parallel temperature in the third picture of Fig. 5.27, followed by another absorption, until a saturation level is reached, at which the ions stream almost unperturbed by the waves. The steep parallel heating reflects also on the alpha anisotropies (see Fig. 5.28), which show a high peak, whose maximum denotes the beginning of the parallel heating for the alphas. Due to pitch angle scattering (probably by cyclotron resonance of the daughter ion-cyclotron waves), the alpha particles are initially heated in perpendicular direction, whereas their parallel velocities are still far from resonance with the IAWs and hence their parallel temperatures stay unchanged. Since the parallel and the perpendicular velocities are, however, not independent, at some point (close to the peak of the anisotropy for the alphas) the ions are trapped by the IAWs and their parallel temperature sharply increases. Later on the parallel heating exceeds the perpendicular one (so that the anisotropy goes below 1), the two components of the temperature continue to rise at a similar rate and the alpha anisotropy saturates at a low level.

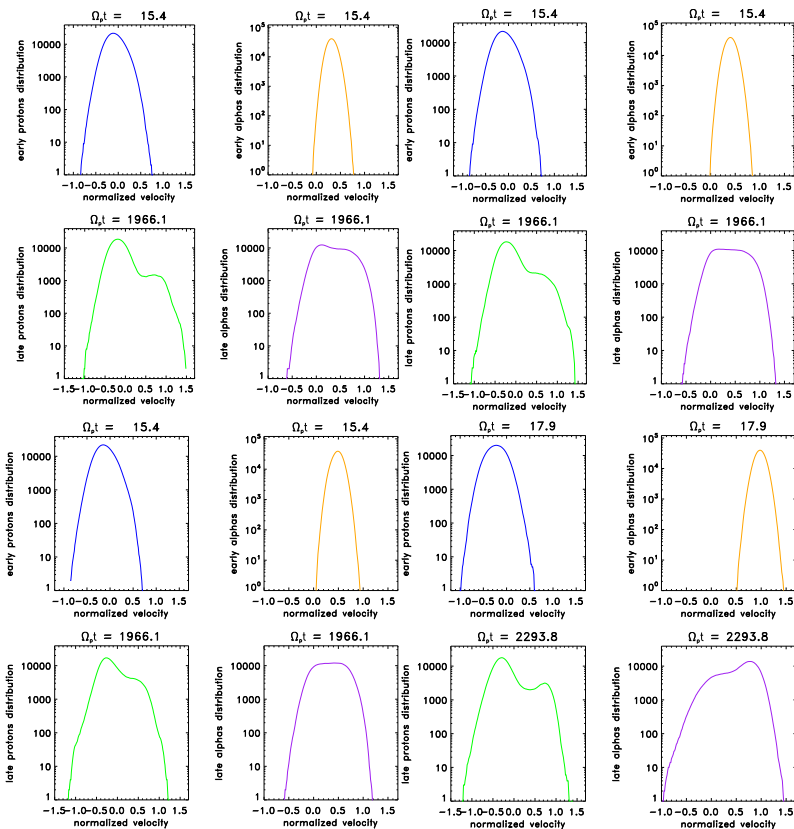


Figure 5.24: Initial and final 1D VDFs for protons and α particles, corresponding to the same initial conditions as shown on Figs. 5.16 – 5.23. The figure consists of 4 groups with 4 plots within each group. The 4 groups are situated in the 4 quadrants, counting from left to right on the first and on the second row, and represent the 4 different initial relative drift conditions, considered for the rest of the figures above (see Fig. 5.10). Then the 4 subplots inside each group describe the 1D VDFs for both species at the first and the last iteration of the simulation code. All velocities are normalized to the Alfvén speed V_A .

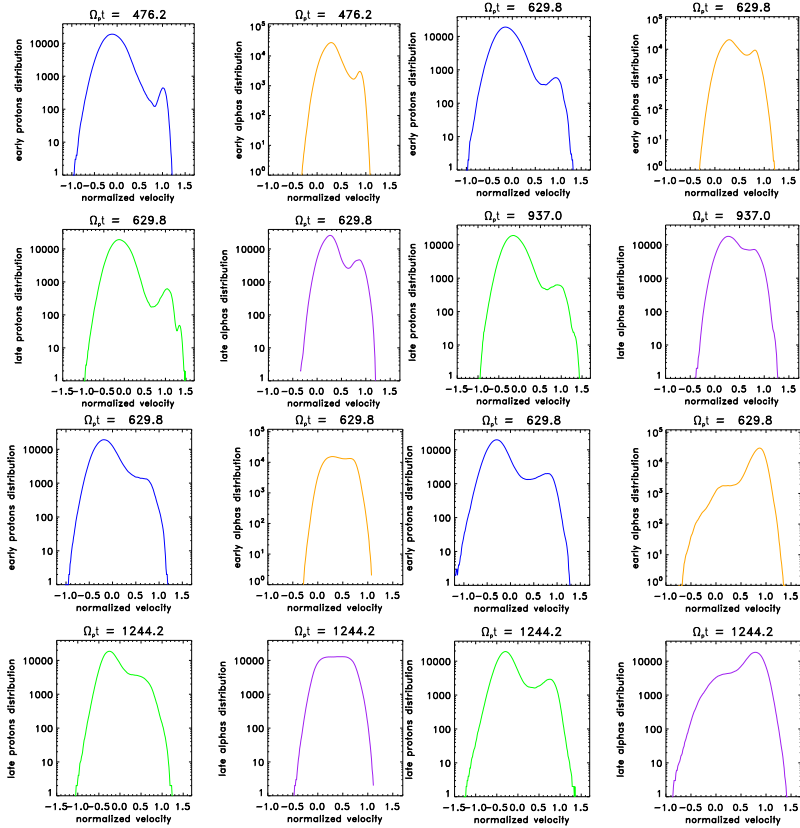


Figure 5.25: Snapshots with intermediate stages from the evolution of the 1D distribution functions described on Fig. 5.24. Random times for the different initial conditions were selected to best illustrate the presence of the beams. The different quadrants in the figure should be read in the same way as on Fig. 5.24.

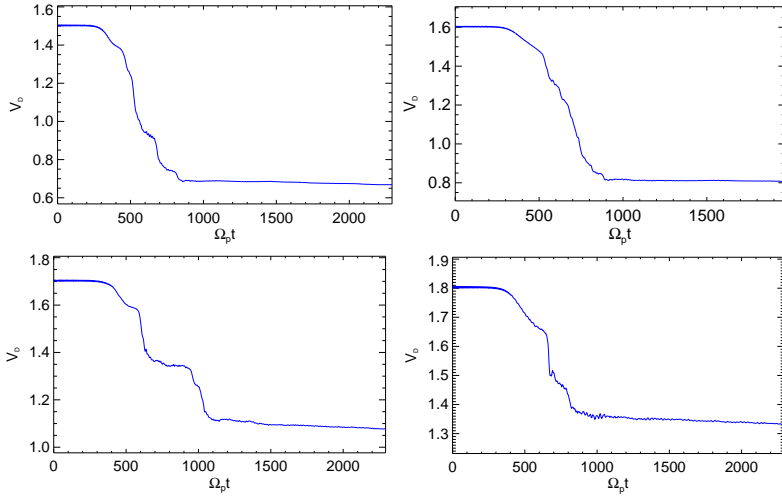


Figure 5.26: Temporal evolution of the relative drift speeds between protons and α particles for initial values $V_{\alpha p, \text{in}} = 1.5, 1.6, 1.7$ and $1.8V_A$. All the other plasma parameters were kept the same as on Fig. 5.10 with the pump wave-frequency accordingly changed, following the solution of the dispersion relation Eq. (4.24).

So far all the simulations were done for the case of equal initial parallel temperatures, $T_p = T_\alpha$, for both ion species, so that we investigated what happens if the plasma is taken from a low density CH region, if an initial thermal equilibrium is imposed. However similar processes occur if we slightly increase the initial temperature for the α particles (for instance up to $\tilde{\beta}_\alpha = \tilde{\beta}_p = 0.08$) and simulate the other important case observed in the solar wind, when the ion species have the same thermal speeds. In this case we observe rather similar behavior of the particles, with the same 4 situations of different initial relative drift regimes, associated strong parallel heating and beam formations. A statistical analysis on the bulk moments of the ion distributions for different initial relative drift and plasma $\tilde{\beta}_s$ regimes is presented in the following Chapter 6.

5 Dissipation of nonlinear Alfvén-cyclotron waves – impact on ion distributions in multi-species plasma

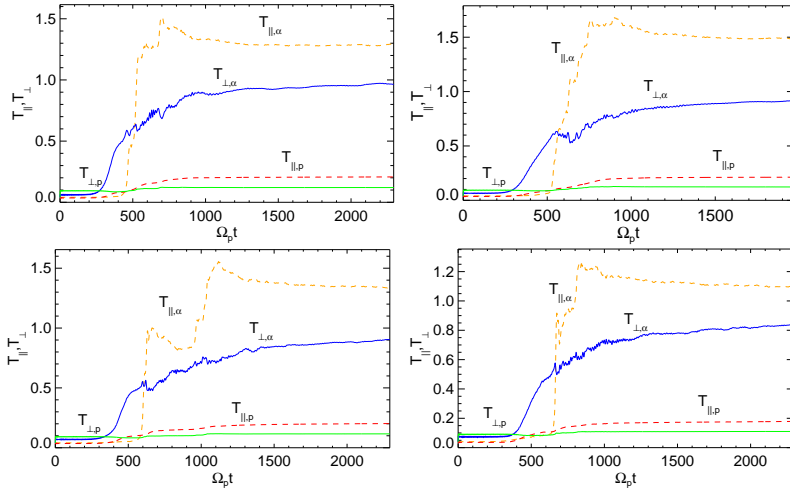


Figure 5.27: Parallel and perpendicular components of the kinetic temperatures for protons and α particles for the same set of parameters, as described on Fig 5.26. Note the completely different behavior of the perpendicular temperature of the α particles, suggesting that different heating processes operate at the 4 different initial relative drift cases.

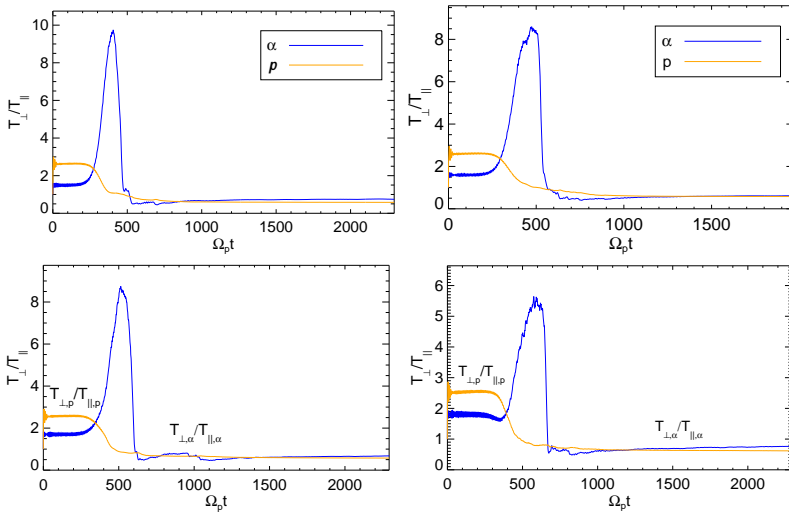


Figure 5.28: Temporal evolution of the temperature anisotropies for protons and α particles for the 4 cases, described on Figs. 5.26 and 5.27.

6 Regulation of ion drifts and anisotropies via parametrically unstable Alfvén-cyclotron waves

This chapter contains the results from a statistical simulation study on the regulation of ion drifts and anisotropies via parametrically unstable Alfvén-cyclotron waves. It investigates the dependence of ion heating and acceleration for an ensemble of different initial relative drifts and parallel plasma $\tilde{\beta}_s$ conditions to draw conclusions about how the heating and acceleration mechanisms possibly operate in the fast solar wind. The chapter provides an extended continuation of the previous Chapter 5, however it deals entirely with the bulk moments of the ion distributions and all the figures include only data points, calculated at the initial or final stages of the simulations. Additionally, only data corresponding to final states, which reach saturation in the course of their evolution is employed and all non-equilibrium states are excluded. The reason for that is to enable a comparison of our results with observed solar wind data. The section below describes the initial conditions used for the statistical study and presents the results from the numerical simulations.

6.1 Simulation study and numerical results

In the previous chapter 5 we showed that parametrically unstable Alfvén-cyclotron waves can be used to preferentially heat and accelerate the plasma species. In this chapter we want to extend this study to investigate up to what values of the relative drift we can keep on accelerating the plasma within the same scenario, and furthermore what happens to the ion temperature anisotropies if we change the initial thermal speeds of the species. That is to say, we want to see what is the impact of nonlinear Alfvén-cyclotron waves on the anisotropic ion heating and acceleration, and how could their parametric instabilities regulate the differential streaming and temperature anisotropies of the plasma species for different initial plasma $\tilde{\beta}_s$ regimes. If we think of the fast solar wind plasma coming from CHs, then higher plasma $\tilde{\beta}_s$ correspond to distances further away from the Sun. Then we can deduce some information not only on the possible heating mechanism, but also on the location, where the different solar wind ion species could acquire their high relative drifts. For this sake we perform series of simulations, keeping all plasma parameters the same, except for the initial relative drifts, $V_{ap,in}$, and respectively, according to Eq. (4.24), the wave-frequency of the pump Alfvén-cyclotron wave, ω_0 . We start with the case of zero relative drifts, already described in chapter 5, and keep on gradually increasing it up to the value of $V_{ap,in} = 1.8V_A$, as shown on Table 6.1. Additionally we vary the initial plasma

run #	ω_0	ω_0/k_0	$V_{\alpha p, \text{in}}$	V_α	V_p	$V_{\alpha p, \text{fin}}^a)$	$V_{\alpha p, \text{fin}}^b)$	$V_{\alpha p, \text{fin}}^c)$	$V_{\alpha p, \text{fin}}^d)$
1.	0.2995	0.7488	0	0	0	0.165	0.143	0.089	0.095
2.	0.3026	0.7565	0.05	0.041	-0.01	0.174	0.178	0.115	0.131
3.	0.3049	0.7623	0.1	0.082	-0.018	0.203	0.202	0.156	0.167
4.	0.3064	0.7660	0.15	0.123	-0.027	0.221	0.240	0.190	0.206
5.	0.3072	0.7680	0.2	0.164	-0.036	0.244	0.292	0.217	0.232
6.	0.3074	0.7685	0.25	0.205	-0.045	0.299	0.338	0.251	0.277
7.	0.3070	0.7675	0.3	0.246	-0.054	0.358	0.388	0.281	0.325
8.	0.3062	0.7655	0.35	0.286	-0.064	0.411	0.428	0.307*	0.344*
9.	0.3049	0.7623	0.4	0.327	-0.073	0.454	0.462	0.338*	0.385*
10.	0.3032	0.7580	0.45	0.368	-0.082	0.481	0.491	0.370*	0.404*
11.	0.3012	0.7530	0.5	0.409	-0.091	0.498	0.500	–	–
12.	0.2988	0.7470	0.55	0.450	-0.100	0.472*	0.498*	–	–
13.	0.2963	0.7408	0.6	0.491	-0.109	0.420*	0.496*	–	–
14.	0.2904	0.7260	0.7	0.573	-0.127	0.441*	0.489*	–	–
15.	0.2837	0.7093	0.8	0.655	-0.145	0.480*	0.546*	–	–
16.	0.2765	0.6913	0.9	0.736	-0.164	0.548*	0.588*	–	–
17.	0.2688	0.6720	1.0	0.818	-0.182	0.601*	0.671*	–	–
18.	0.2606	0.6515	1.1	0.900	-0.200	0.721*	0.725*	–	–
19.	0.2521	0.6303	1.2	0.982	-0.218	0.653*	0.716*	–	–
20.	0.2433	0.6083	1.3	1.064	-0.236	0.641*	0.701*	–	–
21.	0.2342	0.5855	1.4	1.145	-0.255	0.620*	0.702*	–	–
22.	0.2249	0.5623	1.5	1.227	-0.273	0.669	0.869*	–	–
23.	0.2154	0.5385	1.6	1.309	-0.291	0.807	1.109*	–	–
24.	0.2057	0.5143	1.7	1.391	-0.309	1.076	1.216*	–	–
25.	0.1958	0.4895	1.8	1.473	-0.327	1.333	1.434*	–	–

Table 6.1: Simulation parameters for the different runs. The first column shows the pump wave frequency normalized to the proton gyration rate. The second column refers to the phase speed of the pump wave, calculated for the fixed wave-number $k_0 = 0.4\Omega_p/V_A$. The third column contains the values of the initial differential streaming $V_\alpha - V_p$, whereas the forth and the fifth columns give, respectively, the initial bulk speed for alphas and protons in the center of momentum framework. Last 4 columns correspond to the values of the final relative drift for the different studied cases, depending on the initial plasma β_s conditions (for more explanations see the text). All velocities are normalized to the local Alfvén speed.

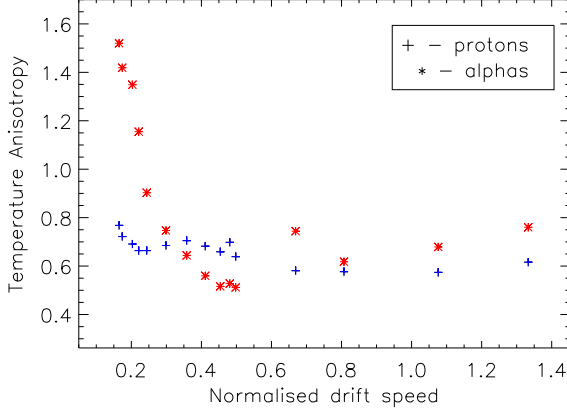


Figure 6.1: Dependence of the ion temperature anisotropies T_{\perp}/T_{\parallel} on the relative drift speed between protons and α particles $V_{\alpha p}$ for $\tilde{\beta}_{\alpha} = 0.02$; $\tilde{\beta}_p = 0.08$, corresponding to case a) from Table 6.1.

$\tilde{\beta}_s$ for the different plasma species in between $\tilde{\beta}_s \in [0.02, 0.35]$, so that we investigate 4 different cases: a) $\tilde{\beta}_{\alpha} = 0.02$, $\tilde{\beta}_p = 0.08$, b) $\tilde{\beta}_{\alpha} = \tilde{\beta}_p = 0.08$, c) $\tilde{\beta}_{\alpha} = \tilde{\beta}_p = 0.2$ and d) $\tilde{\beta}_{\alpha} = \tilde{\beta}_p = 0.35$, where $\tilde{\beta}_s$ is related to the parallel plasma β of the given species and defined as the squared ratio of the parallel thermal speed to the Alfvén speed, $\tilde{\beta}_s \equiv v_{\text{th},\parallel s}^2/V_A^2$. The rest of the plasma conditions are as follows: both ion species were initialized with isotropic Maxwellian distributions, drifting in parallel direction with $V_{\alpha p, \text{in}}$ and in perpendicular with $V_{\perp, s}$, according to Eq. (3.6). The pump wave amplitude was set to $a_0 = 0.25$ and the wave-number was $k_0 = 0.4\Omega_p/V_A$. The electron plasma β for all cases was fixed to $\beta_e = 0.5$. The time step used was $dt = 0.035\Omega_p^{-1}$ for low drifts $V_{\alpha p, \text{in}} \leq 0.8V_A$ and $dt = 0.035\Omega_p^{-1}$ for the rest. The number of superparticles of each species was fixed to 400 per cell. In principle, the ion composition and the partial densities of the different species slightly vary with the type of solar wind and the distance from the Sun. For the sake of simplicity in all simulations we fix the number density of the α particles to be 5 % of the density of the most abundant, electron species, $n_{\alpha}/n_e = 0.05$. Investigation on the dependence of the preferential heating, differential streaming and the intensity of the beam formation on the number density of the α particles is a different subject of research and falls out of the scope of the present work.

The various initial pump wave frequencies, its phase speed, the initial drifts (the relative drift $V_{\alpha p, \text{in}}$ and the bulk velocities V_{α} and V_p) and the resulting final differential streaming for the 4 initial plasma $\tilde{\beta}_s$ conditions, described above are presented on Table 6.1. By comparison of the phase speed of the pump wave and the bulk velocities of the ion species it is easy to recognize the beginning of the regime, where the protons and the α particles are “out of phase”, with the protons being more susceptible to the activity of the pump wave, and the α particles – less dependent (i.e., in this regime the apparent anisotropies for the alphas are smaller as the ones for protons, as their bulk

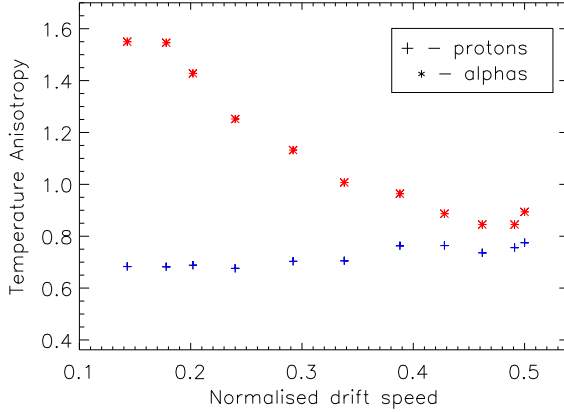


Figure 6.2: Dependence of the ion temperature anisotropies T_{\perp}/T_{\parallel} on the relative drift speed between protons and α particles $V_{\alpha p}$ for $\tilde{\beta}_{\alpha} = \tilde{\beta}_p = 0.08$, corresponding to case b) from Table 6.1.

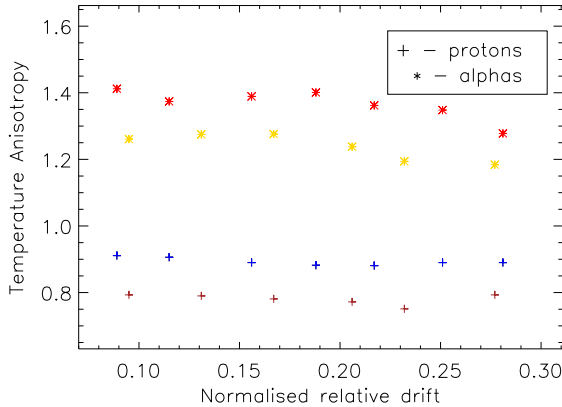


Figure 6.3: Combined plot of the final ion temperature anisotropies T_{\perp}/T_{\parallel} versus final relative drifts $V_{\alpha p, \text{fin}}$ for the cases c) and d) from Table 6.1. The red and blue data points correspond to initially $\tilde{\beta}_{\alpha} = \tilde{\beta}_p = 0.2$, whereas the yellow and light brown – to $\tilde{\beta}_{\alpha} = \tilde{\beta}_p = 0.35$. The relative drifts are normalized to the constant Alfvén speed V_A , set by the homogeneous magnetic background, the proton mass and the electron number density.

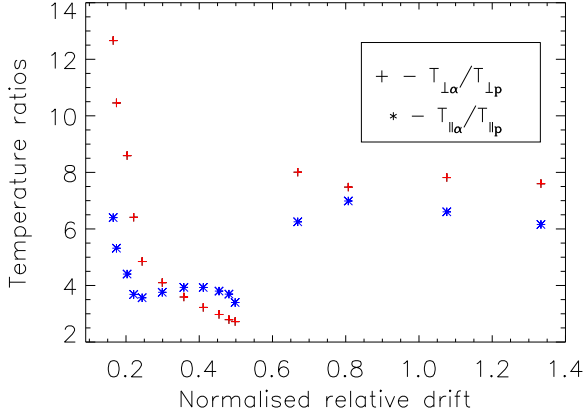


Figure 6.4: Dependence of the parallel and perpendicular temperature ratios between protons and α particles on the relative drift between the 2 plasma species. All the data points were calculated at the final stage of the simulations, where stationary state is reached. The initial conditions correspond to case a) from Table 6.1 with $\tilde{\beta}_\alpha = 0.02$ and $\tilde{\beta}_p = 0.08$.

perpendicular drift, due to the presence of the pump wave, is less). This regime starts when $V_\alpha > v_{ph} > V_p$ and the relative drifts there start to show the characteristic short quasi-stable behavior in the initial stage of the simulations, as discussed in the previous Chapter 5. The last 4 rows give the normalized values of the final relative drifts, calculated at the end of the simulation time. The asterisks denote the cases, where no stationary final states were reached. These data points were excluded from our further analysis, and all the results presented below correspond only to stationary final states.

Fig. 6.1 shows a statistical study on the dependence of the ion anisotropies on the relative drift, similar to the ACE/Wind observations, Fig. 2.8, presented in Chapter 2. The plot corresponds to case a), where the initial plasma $\tilde{\beta}_s$ were $\tilde{\beta}_\alpha = 0.02$ and $\tilde{\beta}_p = 0.08$. Only the data points from simulations that have reached dynamical equilibrium were included (cf. with Table 6.1). The figure shows qualitatively rather similar features to the fast solar measurements presented on Fig. 2.8. The α particles exhibit an enhanced perpendicular heating for low values of the relative drift speed ($V_{\alpha p} < 0.2V_A$ in our simulations) and prominent parallel anisotropies for higher drifts. The proton anisotropies at all relative drifts maintain a higher parallel temperature, due to the proton beam formation. For a given range of the relative drift, $V_{\alpha p} \in [0.35V_A, 0.5V_A]$, the α particles heat up by the IAWs very efficiently in parallel direction, with somewhat reduced perpendicular heating (see Fig. 5.12). This results in the low values of the temperature anisotropy for the alphas in the range $V_{\alpha p} \in [0.35, 0.5]V_A$, where the proton anisotropy exceeds the one of the α particles. Fig. 6.2 demonstrates results in the same format as Fig. 6.1, but for case b), where the ion species were initialized with equal thermal speeds, $\tilde{\beta}_\alpha = \tilde{\beta}_p = 0.08$. The ion anisotropies show similar behavior and once again resemble the observed features from Fig. 2.8, however this time less data points were included (due to the stationary state

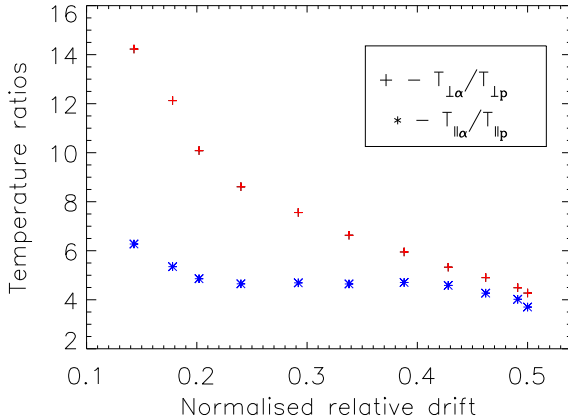


Figure 6.5: The same relation as shown on Fig. 6.4, but for case b), initialized with $\tilde{\beta}_\alpha = \tilde{\beta}_p = 0.08$.

selection rule) and no regime with $(T_{\perp}/T_{\parallel})_p > (T_{\perp}/T_{\parallel})_\alpha$ has been reached. Again the protons remain parallelly heated at all relative drifts, whereas the α particles at low drifts heat preferentially in transverse direction and at high drifts in parallel. Here the slope of the temperature anisotropy curve for the α particles is a bit less steep in comparison to the previous case, Fig. 6.1, where the alphas are initially slightly colder.

As we increase the plasma $\tilde{\beta}_s$, it gets more and more difficult to reach a stationary regime with a saturated final state even for low values of the relative drift speed. Fig. 6.3 shows how the temperature anisotropies profile changes in a high initial plasma $\tilde{\beta}_s$ regime. The yellow (for alphas) and brown (for protons) curves correspond to case c) from Table 6.1, when initially $\tilde{\beta}_\alpha = \tilde{\beta}_p = 0.2$. The red (for alphas) and blue (for protons) curves correspond to case d) with $\tilde{\beta}_\alpha = \tilde{\beta}_p = 0.35$. We can see that the slope of the temperature anisotropy curves becomes almost flat, so that $(T_{\perp}/T_{\parallel})_\alpha$ (denoted by asterisks) is not so steep as in the case of lower initial $\tilde{\beta}_s$, or as in the case of the observations (Fig. 2.8). We can also see that the proton anisotropy (marked by +) is slightly increasing from $(T_{\perp}/T_{\parallel})_p \sim 0.7$ in cases a) and b) to $(T_{\perp}/T_{\parallel})_p \sim 0.8$ and $(T_{\perp}/T_{\parallel})_p \sim 0.9$ for cases c) and d), respectively. The dependence of the ion anisotropies on the values of the initial plasma $\tilde{\beta}_s$ is illustrated on Fig. 6.7. We can see that as the initial β_s increases, the temperature anisotropies for both protons and α particles take values from a narrow restricted interval. For the other cases of high $\tilde{\beta}_s$ and large $V_{\alpha p, in}$ within 2000 gyroperiods the system still does not reach dynamical equilibrium, and there is no saturation for the relative drifts, nor for the ion anisotropies. Therefore we have excluded those cases from our statistical analysis.

Let us now go back to the ion anisotropies, observed in situ in a high $\tilde{\beta}_s$ regime at 1AU near the Earth and speculate a bit on the implications of the results. We have shown that high $\tilde{\beta}_s$ simulations lead to much different ion-anisotropies and hardly reach any stationary regime for high values of the relative drift. Therefore we can deduce that if nonlinear

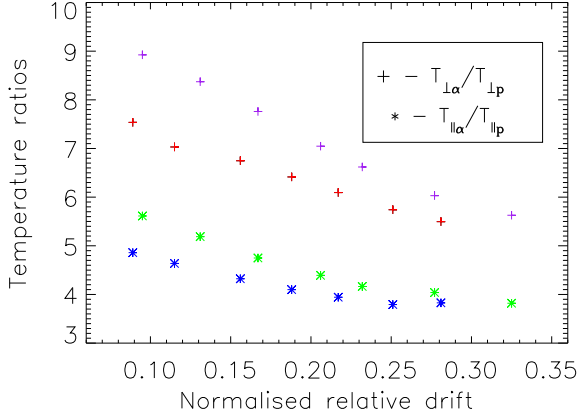


Figure 6.6: Dependence of the temperature ratios between protons and α particles on the relative drift for cases c) and d). The purple and green curves denote, respectively, the perpendicular and parallel temperature ratios for initial values $\tilde{\beta}_\alpha = \tilde{\beta}_p = 0.2$. The red and blue data points refer to $\tilde{\beta}_\alpha = \tilde{\beta}_p = 0.35$.

Alfvén-cyclotron waves are responsible for the particles heating and acceleration, then the observed heating should have occurred earlier, in a lower $\tilde{\beta}_s$ regime, close to the Sun. The simulations also show that for the 2 investigated cases with high initial plasma $\tilde{\beta}_s$, the ions cannot be accelerated by the Alfvén-cyclotron wave up to more than just a small fraction of the local Alfvén speed $V_{\alpha p} \in [0.25, 0.3]V_A$. Thus if one considers that the observed anisotropies were caused by some local heating mechanism, one needs additionally to think of a way how to differentially accelerate the particles in the first place. On the contrary, in low $\tilde{\beta}_s$ conditions the non-thermal ion heating and acceleration by large-amplitude waves develop simultaneously, suggesting that this might be a key mechanism to act in the fast solar wind outflows. We should note, however, that even though the simulated ion anisotropies at low $\tilde{\beta}_s$, Fig 6.1 and Fig 6.2, look rather similar to the observed fast solar wind values near the Earth, the simulated temperature ratios, Figs 6.4 – 6.6 between the 2 species show a different behavior and deviate from the values, based on ACE/Wind measurements [Kasper *et. al.* (2008)]. They differ in several ways: first the value of the perpendicular temperature ratio $T_{\perp\alpha}/T_{\perp p}$ in the simulations is about twice as high, then the parallel ratio does not follow an inverse parabola, and thus the model slopes for both temperature ratios do not reproduce the observations. If we decrease the initial amplitude of the pump wave (reduce it twice, for instance), the simulated values of the temperature ratios go within the observed range. But reduction of the pump amplitude results also in a reduced preferential heating and acceleration. We should note, that the experimental temperature ratios also depend on modeling and plenty of uncertainties. In addition, the real solar wind is rather turbulent, whereas our model assumed initially a single monochromatic wave. Despite these remarks, it is interesting to see that even a simple 1D collisionless model, based on a parametrically unstable nonlinear wave, is still

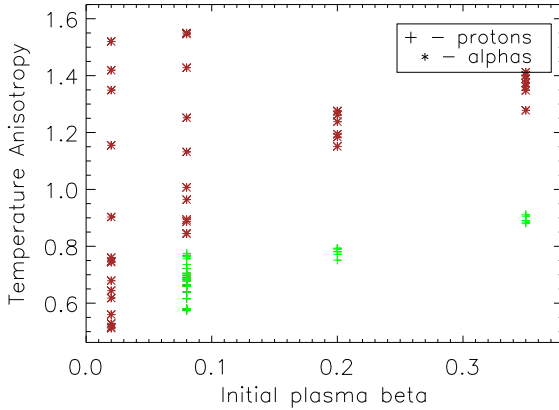


Figure 6.7: Ion temperature anisotropies, taken at the final saturated stage of the simulations versus initial parallel plasma $\tilde{\beta}_s$. The plot indicates that at higher initial $\tilde{\beta}_s$ the anisotropies are more restricted, and there are no prominent signatures for parallel heating of the α particles, unlike the low values of the alpha anisotropy, present at lower initial $\tilde{\beta}_s$.

able to reproduce many of the observed ion features in the fast solar wind.

Fig. 6.4 plots the parallel and perpendicular temperature ratios of α particles and protons for the case, when the two species start with equal initial temperatures. The range $V_{\alpha p, \text{fin}} = [0.35, 0.5]V_A$ exhibits particularly reduced perpendicular temperature ratios, whereas the parallel ones stay almost constant (or slightly increase). This coincides with the regime in the ion anisotropies, Fig. 6.1, where the anisotropy of the protons exceeds the one of the α particles. In that case the low temperature anisotropy for the α particles ($T_{\perp}/T_{\parallel} < 0.7$) is associated with a reduced perpendicular heating. On the contrary, at higher relative drifts $V_{\alpha p, \text{fin}} > 0.5V_A$, the low temperature anisotropy is related to a preferential parallel heating of the α particles.

Fig. 6.5 shows the parallel and perpendicular temperature ratios of α particles and protons for the case, when the two species were initialized with equal thermal speeds. In this case the parallel and perpendicular temperature curves do not overlap each other and there is a general trend that the perpendicular heating of alphas relative to protons gradually decreases with increasing relative drift, whereas the parallel ratio almost does not change. We should note that the parametric instabilities at high drifts make the system very unstable, and hence we have not included data points with $V_{\alpha p} > 0.5V_A$. As we go to higher plasma $\tilde{\beta}_s$, the system becomes unstable at even lower initial drifts. Fig. 6.6 shows the parallel and perpendicular temperature ratios corresponding to two cases of high plasma $\tilde{\beta}_s$, $\tilde{\beta}_\alpha = \tilde{\beta}_p = 0.2$ and $\tilde{\beta}_\alpha = \tilde{\beta}_p = 0.35$, when both species initially have the same thermal speeds. From the three figures one can see that the magnitude of the temperature ratios decreases with increasing the values of the initial plasma $\tilde{\beta}_s$ and their slopes change as well. Together with the temperature ratios, the temperature anisotropy also changes for the different initial plasma $\tilde{\beta}_s$. Fig. 6.7 illustrates this dependence for protons (green

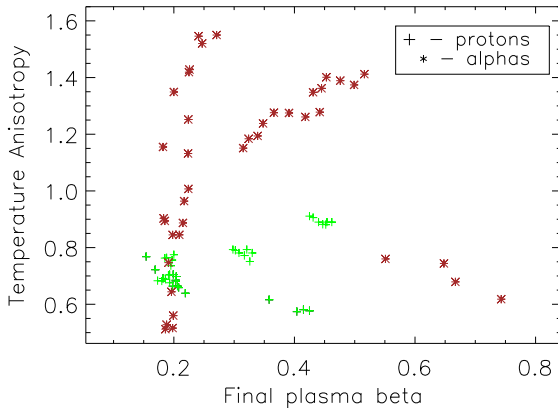


Figure 6.8: Final temperature anisotropy for the protons (shown by green + symbols) and α particles (denoted by red asterisks) versus final parallel plasma $\tilde{\beta}_s$. The plot with the anisotropies for the alphas is much more scattered, whereas the anisotropies for the protons appear more confined within a smaller range $T_{\perp}/T_{\parallel} \in [0.55, 0.95]$. In all simulated cases Landau damping of the daughter IAWs occurred, and related beam formations were present, without a simultaneous strong perpendicular proton heating, which results in the observed parallel anisotropies for the protons.

pluses) and α particles (red asterisks). The plot shows a general tendency to have more scattered (i.e., wider) ion anisotropy range at lower initial $\tilde{\beta}_s$, whereas at high $\tilde{\beta}_s$ there is no parallel anisotropy for the α particles at all. This might be due to the fact that we have included only data points corresponding to low relative drift speeds, $V_{ap} \leq 0.35V_A$. Additionally, the α particles are more affected by the waves and by the values of the initial relative drift V_{ap} than the protons, and their anisotropies lay within a larger range, independently of the initial plasma $\tilde{\beta}_s$. On the contrary, the protons are parallelly heated for all the investigated values of the relative drifts and plasma $\tilde{\beta}_s$, with a slight tendency to increase their anisotropy at larger $\tilde{\beta}_s$.

We may also look at the scatter plot of the final ion temperature anisotropies versus the final plasma $\tilde{\beta}_s$ as presented on Fig. 6.8. The simulated anisotropy-plasma $\tilde{\beta}_s$ relation for the protons falls within the majority of data points as observed in the fast solar wind near the Earth (by ACE/Wind, Fig. 2.9 [Bale *et al.* (2009)]) and beyond (by Ulysses [Gary *et al.* (2002)]). So far, statistical analysis on the behavior of α particles based on in situ measurements in the solar wind remains difficult, due to both instrumental constraints and high uncertainties coming from the low α particle flux. Then, the simulation results could give a prediction for the expected variance of the anisotropies of the α particles $(T_{\perp}/T_{\parallel})_{\alpha}$ depending on their parallel $\tilde{\beta}_{\alpha}$, in case that the ions are heated by unstable Alfvén-cyclotron waves.

Even though both ion species are heated for all investigated values of the initial plasma $\tilde{\beta}_s$, see Fig. 6.9, the amount of parallel heating depends on the individual plasma $\tilde{\beta}_s$ in

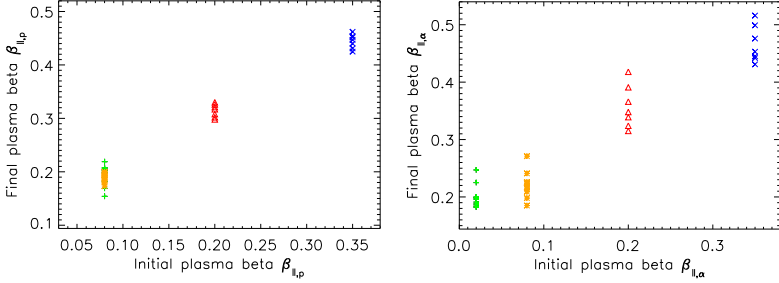


Figure 6.9: Final versus initial parallel plasma $\tilde{\beta}_s$ for protons (left panel) and α particles (right panel). The different colours/symbols correspond to the four investigated initial plasma $\tilde{\beta}_s$ conditions: $\tilde{\beta}_\alpha = 0.02, \tilde{\beta}_p = 0.08$ (green pluses); $\tilde{\beta}_\alpha = \tilde{\beta}_p = 0.08$ (yellow asterisks); $\tilde{\beta}_\alpha = \tilde{\beta}_p = 0.2$ (red triangles) and $\tilde{\beta}_\alpha = \tilde{\beta}_p = 0.35$ (blue crosses).

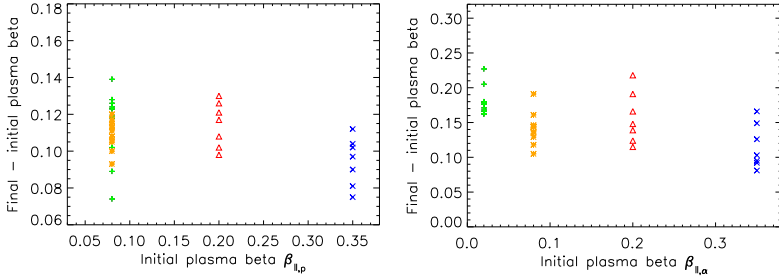


Figure 6.10: The difference between final and initial parallel plasma $\tilde{\beta}_s$ for the two ion populations versus the initial values of $\tilde{\beta}_s$. The left panel is for protons and the right one shows the α particles. The colours and the symbols follow the notations on Fig. 6.9.

a non-trivial manner, as visible on Fig. 6.10. In we only look at the final temperatures, Fig. 6.9, we might think that the ions are strongly heated in a higher $\tilde{\beta}_s$ regime. However, Fig. 6.10 clearly shows that such an assessment would be incorrect. The graph gives a measure of the relative heat absorbed from the waves by each particle species as a function of the initial ion temperature in parallel direction. To estimate the heating rate in transverse direction we need to simply multiply the data points on the ordinate by the corresponding values of the temperature anisotropy. To avoid confusion in the comparison between the different initial plasma $\tilde{\beta}_s$ conditions, the last data points from Table 6.1 (corresponding to high relative drifts) have been excluded. From these figures we can draw the conclusion, that the heating and acceleration processes operate together and hence, the heating rate depends not only on the plasma $\tilde{\beta}_s$, but on the relative drift speed as well. To confirm this idea, Fig. 6.11 shows the final relative drift speed of the particles as a function of the values of their final plasma $\tilde{\beta}_s$. The plot implies that the relative drift is

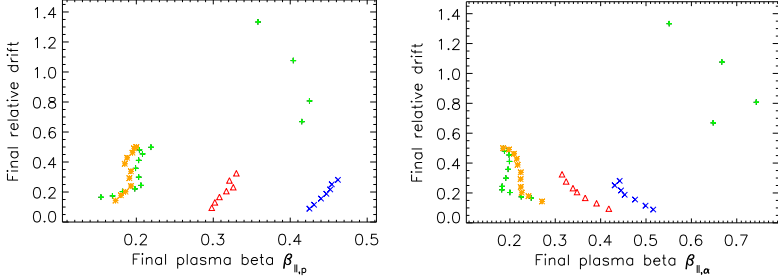


Figure 6.11: Final relative drifts versus final parallel plasma $\tilde{\beta}_s$. The left panel shows the protons and the right one stands for the α particles. The notations follow Fig. 6.10.

strongly dependent on the temperature, especially at low $\tilde{\beta}_s$. The simulations suggest that up to $V_{ap,in} = 0.5V_A$ it's easier to heat the α particles in a low relative drifts regime. Looking from another point of view, the ion acceleration depends on the plasma $\tilde{\beta}_s$, and it is easier to accelerate the helium-4 nuclei at lower $\tilde{\beta}_\alpha$ values, whereas the opposite is true for protons. Having the lower gyrofrequency, the α particles are the first to extract the energy from the waves at low relative drifts, hence it is easier to heat protons at higher drifts and they accelerate faster at lower final (and respectively initial) $\tilde{\beta}_p$. This is, however, true only for initial relative drifts in the range $V_{ap,in} \in [0, 0.5]V_A$.

Above $V_{ap,in} = 0.5V_A$, the parametric instabilities change their nature, the system becomes quickly unstable (after a few proton gyroperiods) and an analogue of the magnetosonic instability occurs. It reduces the value of the initial relative drift and produces strong daughter IAWs, which are fastly being absorbed via Landau damping and heat both ion species in parallel direction. Here, we should note, that for the entire range of initial plasma parameters the system, in principle, is stable with respect to the linear magnetosonic instability, corresponding to the straight line $V_{ap,in} = V_{ap,fin}$ on Fig 6.12. This is confirmed also by simulations, excluding the initial pump. The large-amplitude Alfvén-cyclotron wave, however, provokes nonlinear couplings via the parametric decays, which destabilizes the system at relatively low values of the initial drift speed ($V_{ap,in} > 0.5V_A$) and provides additional source for parallel heating. For details on the kinetics refer to Chapter 5.

Fig. 6.12 shows the change of the initial relative drift speed for the four investigated initial plasma $\tilde{\beta}_s$ cases. The figure demonstrates that we cannot accelerate the ions to relative velocities higher than $V_{ap,in} = 0.5V_A$ and above this value the system becomes unstable. Thus, even though it usually stabilizes the bump-on-tail instability, the role of the pump wave can also be to destabilize the parametric analogue of the magnetosonic instability. That is to say that in the absence of the large-amplitude pump, the plasma system would be stable for all values of the initial relative drift, used in our simulations, so that we would expect no significant change in the relative drift during each simulation run. Then the relative drifts on Fig. 6.12 would follow the straight line. Indeed, results from simulations without a pump prove the relation $V_{ap,in} \approx V_{ap,fin}$. The simulation data on Fig. 6.12, though, shows that inclusion of the pump influences the differential streaming,

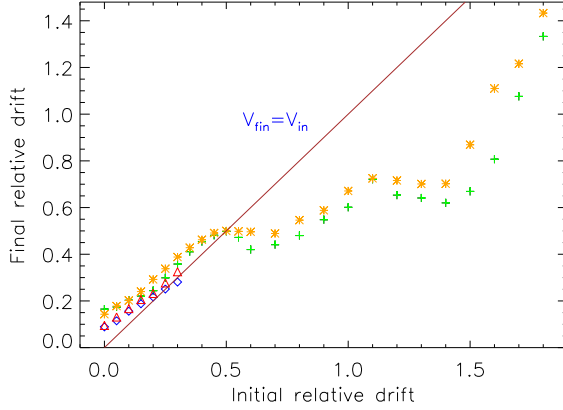


Figure 6.12: Final versus initial relative drifts for different initial parallel plasma $\tilde{\beta}_s$ conditions. Blue diamonds correspond to $\tilde{\beta}_\alpha = \tilde{\beta}_p = 0.35$, case d), red triangles $\tilde{\beta}_\alpha = \tilde{\beta}_p = 0.2$, to case c). Green pluses denote case b), $\tilde{\beta}_\alpha = \tilde{\beta}_p = 0.08$ and yellow asterisks stand for case a) with $\tilde{\beta}_\alpha = 0.02$ and $\tilde{\beta}_p = 0.08$.

so that it can either accelerate the α particles to higher values of the relative drift (for $V_{\alpha p, \text{in}} < 0.5V_A$), or significantly slow them down (for $V_{\alpha p, \text{in}} \geq 0.6V_A$). In addition, for $V_{\alpha p, \text{in}} \geq 0.9V_A$, when $V_\alpha > \omega_0/k_0$ (see Table 6.1), we have a short initial phase, where the relative drift between the α particles and the protons is quasi-conserved (see Fig. 5.10 and Fig. 5.26), suggesting that in this case the pump wave does not interfere much with the motion of the α particles, and they are decelerated later by the daughter waves with the depletion of the pump after the onset of the parametric instabilities. In contrast, at low drifts ($V_{\alpha p, \text{in}} < 0.5V_A$) the resonant daughter waves have higher phase speeds than the bulk of the alphas, hence the α particles get accelerated. Additionally, the pump in those cases causes much more oscillations in the bulk moments (including the parallel motion) of the α particles and less in the bulk moments of the protons, whereas at high drifts the opposite effect is observed (see Chapter 5). Finally, we should note, that all data points with initial relative drifts between $[0.5, 1.4]V_A$ do not reach a stationary state, and hence we have included them only to illustrate the effect of the parametric instabilities.

7 Heating and acceleration of heavy ions in CHs and fast solar wind

This chapter is based on a proceedings material [Maneva *et. al.* (2010)], though it contains an additional survey on the bulk moments of the investigated oxygen species, together with the lighter α particles and protons. Similar to the previous Chapters 5 and 6, we perform 1D hybrid simulations to investigate the nonlinear evolution of the tenuous collisionless magnetized plasma in CHs and the fast solar wind. This time, however, we have extended our research, including an additional heavy ion species. We compare the results from numerical experiments on the behavior of oxygen ions, studying two different ionization states, O^{5+} and O^{6+} , of five and six times ionized oxygen, respectively. Once again we assume initially isotropic velocity distribution functions, where in the presence of the pump, the 3 populations of ion species acquire different perpendicular drift, according to Eq. (4.26), and hence the pump wave influences them differently. The ion distributions are later reshaped via wave-particle interactions with the daughter waves that are born by the parametrically unstable large-amplitude Alfvén-cyclotron pump wave. Once again the decay processes lead to the formation of both acoustic and electromagnetic micro-turbulence, which further influence the motion of the ions via Landau damping and pitch-angle scattering. This leads to a depletion of the pump and destroys the fluid coherence of the medium. Parametric instabilities further act to randomize the ion distributions, causing anisotropic heating and resulting in differential streaming and formation of ion beams. Due to their low mass densities and charge-to-mass ratios heavy ions are preferentially heated and obtain higher anisotropies than the α particles or the protons. *In situ* measurements of high-speed solar wind and remote sensing confirm the existence of ion-cyclotron waves near 1AU [Jian *et. al.* (2009)] and high-frequency plasma waves even above the ion gyroscsles [Briand *et. al.* (2009)]. As discussed in the introductory Chapter 1, nonlinear Alfvén waves are also intrinsic features of the hot plasma in CHs and the fast solar wind [Bruno *et. al.* (2005)]. The idea is to investigate the effect of a single monochromatic large-amplitude Alfvén-cyclotron wave on the ion distributions and compare the behavior of the oxygen ions within the two different ionization states (in spectroscopic notations Oxygen VI and Oxygen VII), as they have been used for remote sensing above CHs [Telloni *et. al.* (2007)] and measured *in situ* in the solar wind near 1AU [Berger *et. al.* (2010)]. This chapter aims to show the preferential heating of minor ions, and simultaneously to throw light on the origin of the different heating rates and anisotropies of the oxygen ions as observed in the corona and in the fast solar wind.

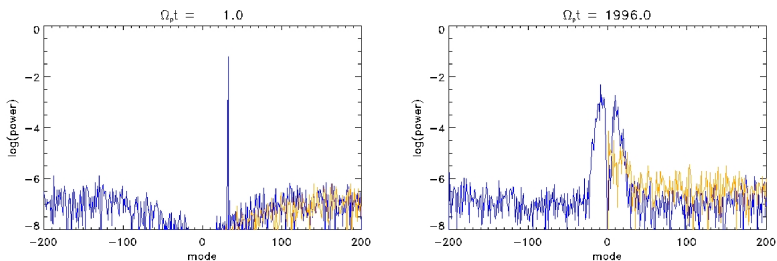


Figure 7.1: Initial power spectra at one iteration step after the beginning of the simulations. The ordinate shows the square of the Fourier-transformed magnetic field fluctuations normalized to the background magnetic field. The abscissa denotes the wave modes m , related to the wave-number in the following manner: $m = 32k/k_0$. Therefore the intense peak at mode number 32 of the electromagnetic spectrum (blue lines) on the left panel represents the large-amplitude pump wave. The low level of acoustic fluctuations (in yellow) is due to the thermal noise of the system and is practically determined by the initial plasma $\tilde{\beta}_s$. The right panel contains a snapshot of the final power spectra at the latest time of the simulations, $t = 1996 \Omega_p^{-1}$, when the macro properties of the system like drifts, temperatures and anisotropies have already reached a saturation state. The graph shows the growth of both ion-acoustic (in yellow) and electromagnetic (blue lines) microturbulence due to continuously operating parametric decays (see Chapters 3 and 5).

7.1 Initial setup

As in the previous chapters all computations are performed in the ions center-of-mass frame of reference, and the size of the box covers 32 times the wavelength of the pump. The time step was $0.03\Omega_p^{-1}$ and the number of grid points was 2048, with 200 particles per cell. Like in the pure proton- α -particle case, due to the self-consistent coupling of the ions and the electromagnetic field of the pump, each ion species attains a different apparent initial anisotropy (as visible on Figs. 7.2–7.3 and Fig. 7.11–7.12), depending on the wave frequency of the pump and the individual ion gyrofrequency. Once again this is not related to the ion thermal motion and hence does not imply different physical temperatures along and across the magnetic field lines. Thus we start the simulations with initially isotropic distributions for all ion species, which after the decay processes causing the depletion of the pump get randomized and further reshaped via the wave-particle interactions with the daughter waves. Additionally all ions initially are drifting in transverse direction, according to Eq. (4.26) and no bulk motion along the parallel axis is assumed, i.e. $V_{\alpha p, \text{in}} = V_{\text{oxy } p, \text{in}} = 0$. The initial pump wave-number was fixed to $k_0 = 0.4\Omega_p/V_A$, the amplitude was taken to be 25% of the magnitude of the background magnetic field, and the normalized number densities were: $n_\alpha = 0.05n_e$ for the α particles and $n_{\text{oxy}} = 0.0003n_e$ for both oxygen species. The ratio of the initial thermal velocity to Alfvén speed was chosen to match SWICS measurements in the fast solar wind [Berger *et al.* (2010)], so that $\tilde{\beta}_p = 0.18$, $\tilde{\beta}_\alpha = 0.2$ and $\tilde{\beta}_{\text{oxy}} = 0.125$ for both ionization states of the oxygen ions. Thus the protons and the α particles at the beginning have almost mass-proportional tempera-

ture ratios. The electron plasma β was set to 0.5. This facilitates the onset of parametric instabilities without directly affecting the basic heating processes considered here.

Fig. 7.1 represents the initial and final spectra from the simulation of a hot plasma, consisting of protons, α particles and O^{5+} ions. In the case of O^{6+} as a minor ions population the main features of the spectra remain the same, with both strong modulational instability (recognized by the electromagnetic peak on the positive, right-hand side of the spectrum and associated acoustic waves) and a decay-like instability (characterized by the peak on the negative, left-hand side of the electromagnetic spectrum) in the final stage. Those two parametric processes are respectively responsible for the generation of daughter acoustic waves which support the acceleration of protons into beams and of backward propagating daughter transverse waves that counteract the beam formation, pushing the particles in the sunward direction. The spectra show a tendency for an inverse cascade with concentration of the wave power at low wavenumber modes (similar to what was previously found in an earlier study on the behavior of α particles in the fast solar wind [Araneda *et al.* (2009); Maneva *et al.* (2009)]). In the final stage we can recognize a strong decay-like instability (apart from the modulational), which determines the less prominent proton beam formation (in comparison with the simulation results, presented in Chapter 5) by pushing the beam protons backward, towards the core.

Fig. 7.2 shows contour plots with snapshots of the early velocity distribution functions for O^{5+} ions, α particles and protons (counting from left to right), whereas Fig. 7.3 plots the VDFs for O^{5+} ions, α particles and protons. Parallel velocities are displayed in horizontal direction and the vertical velocity components (perpendicular to the homogeneous external magnetic field lines) are plotted along the y-axis. All the initial parameters for the two runs were kept the same, and only the pump-wave frequency was slightly shifted in accordance with Eq. (4.24), so that $\omega_0 = 0.29456\Omega_p$ and $\omega_0 = 0.29823\Omega_p$ for the O^{5+} and O^{6+} case, correspondingly. Figs. 7.2 and 7.3 demonstrate that even though the change in the pump wave frequency is very small, the different gyrofrequency of the two oxygen species causes a great difference in the initial apparent anisotropy, with the oxygen VI being initially prone to much high perpendicular drifts.

7.2 Trapping, heating and acceleration

With the depletion of the pump a row of consequent parametric instabilities leads to the formation of micro-turbulent electromagnetic spectra (see Fig. 7.1) and randomization of the initial bulk motion. Then cyclotron resonance leads to further enhanced perpendicular heating of the minor ions, whereas trapping in (and related Landau damping of) the daughter IAWs causes formation of proton beams (see Fig. 7.4 and Figs. 7.5–7.6). Due to their very low density the heavy ions can not absorb a substantial fraction of the available wave power and hence do not seriously affect the behavior of the main species. That implies that heating and acceleration of protons and α particles do not change within runs with different oxygen ions, though, due to their different kinematics, the behavior of the heavy ions themselves can vary significantly. For this sake we present here a combined plot for the trapping of all 4 plasma species, even though they result from different simulations.

Fig. 7.4 illustrates the partial trapping of protons in the electric potential of the daughter

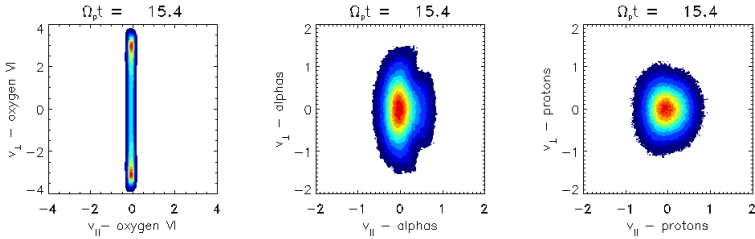


Figure 7.2: Snapshots with contour plots of the early VDFs for O^{5+} , α particles and protons. The distribution for each species is normalized with respect to its own maximum number of particles, and the colour bar ranges from a few % (in dark blue) up to 1 (in dark red). Note the high apparent initial anisotropy of the oxygen ions as compared to protons, α particles and O^{6+} ions (shown on Fig. 7.3). This is due to their larger transverse bound motion induced by the pump, whose frequency is closer to resonance with O^{5+} .

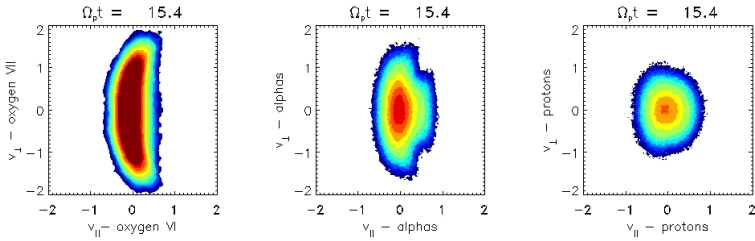


Figure 7.3: Contour plots of the early VDFs for O^{6+} , α particles and protons (from left to right), similar to those on Fig. 7.2, however, this time, a fixed normalization for all species was applied.

ion-acoustic waves whose phase speed approaches $0.6V_A$. At the same time the α particles show slight degree of coherent motion and the oxygen ions are rather randomly squashed and do not coherently react to the waves. Those effects can be more thoroughly examined when we look at the 3D distribution functions. The large expansion rate of the VDF of O^{5+} ions in comparison to velocity distributions of the rest of the species is related to the choice of the initial pump wave as discussed below.

Fig. 7.5 and Fig. 7.6 show the same plots of the velocity distributions as the ones described on Figs. 7.2–7.3, but taken at the final stage of the simulations, long after the decay of the initial Alfvén-cyclotron wave due to parametric plasma instabilities. At that time the initial Alfvén-cyclotron wave is already depleted, and the ion heating has reached a saturation state. In this particular case the proton beam forms (from the absorption of daughter IAWs related to the modulational instability, marked by the prominent electromagnetic peak on the

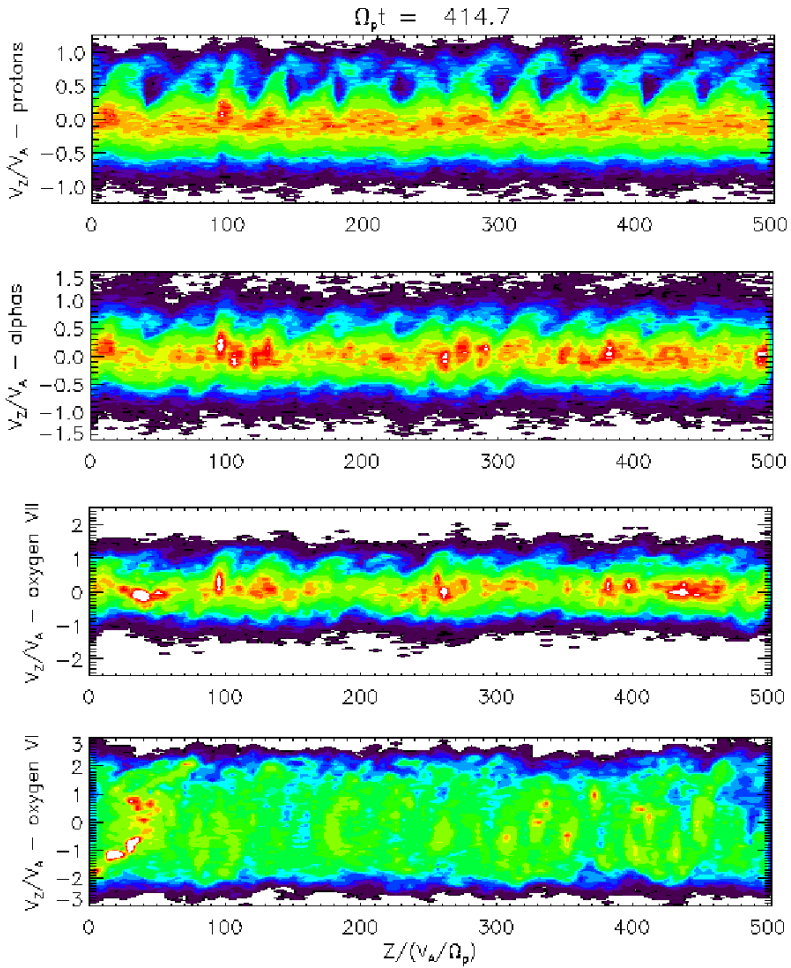


Figure 7.4: 1D phase portrait for protons, α particles, O^{6+} and O^{5+} ions at $\Omega_p t \sim 415$. The plot shows that protons are partially trapped, whereas α particles and oxygen ions are squashed by the waves in a random manner.

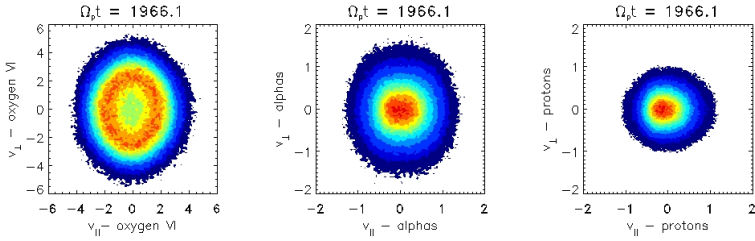


Figure 7.5: Contour plots of the VDFs for protons, α particles and O^{5+} ions at the latest simulation time. We can clearly distinguish the preferential and highly anisotropic heating of the minor ions, rather prominent for O^{5+} . The middle section shows slightly anisotropic heating for the alpha particles as well. The last plot illustrates parallel heating of protons related to the formation of a weak proton beam. Mind the different velocity scales in the distributions. The normalization was adopted from Fig. 7.2.

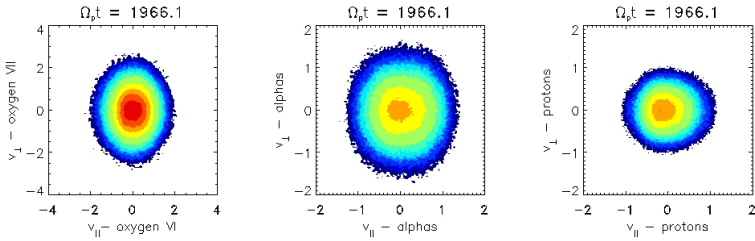


Figure 7.6: The same snapshot as shown on Fig. 7.5, but for the case of protons, α particles and O^{6+} ions. The normalization and the colour bars follow Fig. 7.3.

right-hand side of Fig. 7.1) and smears out again due to wave-particle interactions with the backward propagating electromagnetic daughter waves caused by a decay-like instability (as visible from the high electromagnetic peak on the left-hand side of Fig. 7.1). Note that the heavy ions are more prone to cyclotron resonance which further facilitates their high dispersion in perpendicular direction in comparison to the lighter species. Due to their lower cyclotron frequency O^{5+} ions are closer to resonance with the pump. Thus they are initially forced to follow orbits with much larger perpendicular velocities (see Eq. (4.26)), and therefore later they easily scatter to higher temperatures. We should note, however, that the difference in the initial apparent anisotropy and hence in the acquired heating rates for the two oxygen species strongly depends on the choice of the pump. For example, if we reduce the initial pump frequency to $\omega_0 = 0.25\Omega_p$, their evolutions would be much more similar.

The normalization for Figs. 7.2 and 7.5 was done for each ion species independently using its maximum number density at the given moment of time. The contour colour lev-

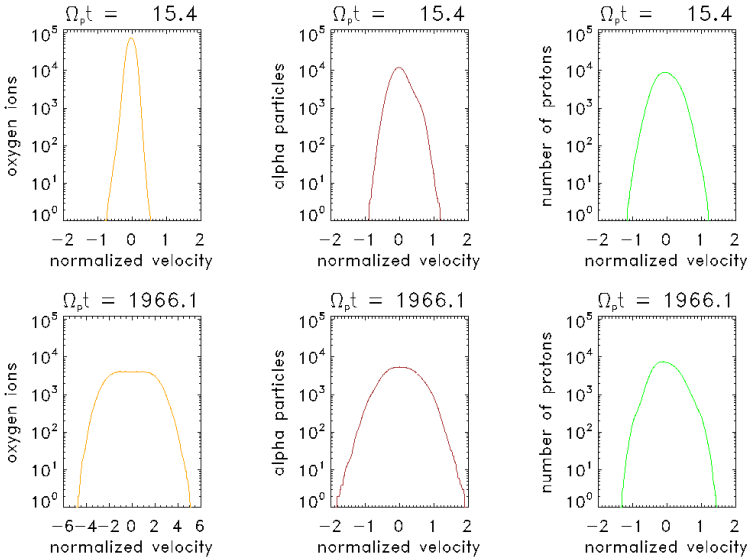


Figure 7.7: Snapshots of the early and final 1D VDFs for O^{5+} ions, α particles and protons (from left to right). The x -axis shows the parallel velocity normalized to the Alfvén speed and the ordinate plots the number of particles with a given speed.

els separate areas with 1 (the darkest blue), 5, 10, 20, 30, 40, 50, 60, 70, 80, 90 and 100 (the darkest red) % of the intrinsic maximum number density of the corresponding specie (i.e. the colours indicate different densities for the protons, α particles and oxygen ions and each distribution is normalized to its own maximum value). For a better visibility, the normalization for Figs. 7.3 and 7.6 was done using fixed values for the contour levels, one and the same for all ion species. Taking this into account, we should note that the distribution functions for both protons and α particles from Figs. 7.2 and 7.3, as well as Figs. 7.5 and 7.6 look the same, and only the heavy species show different features. This supports the idea that the number density for the oxygen ions is far too low to create any change in behavior of the minors, as long as we do not change the rest of the plasma parameters. The ion acceleration in our model in general strongly depends on the ion gyrofrequency of the given particles. For the lighter species (protons and α particles) it stays approximately the same, whereas for the oxygen ions it strongly depends on their ionization state. For the investigated case the O^{3+} ions get much strongly heated than the six-fold ionized oxygen O^{6+} , but the latter accelerates to higher drifts instead. The acceleration of the lighter species in both cases, however, remains practically the same, as well as their anisotropic heating, presented on Fig. 7.11. This suggests once again that the heavy ions are too tenuous to affect the dynamics of the more abundant protons and α particles. Similar ordering of the heating rates with respect to the gyrofrequency of the species were observed in the fast solar wind [Von Steiger *et al.* (1995)], indicating that

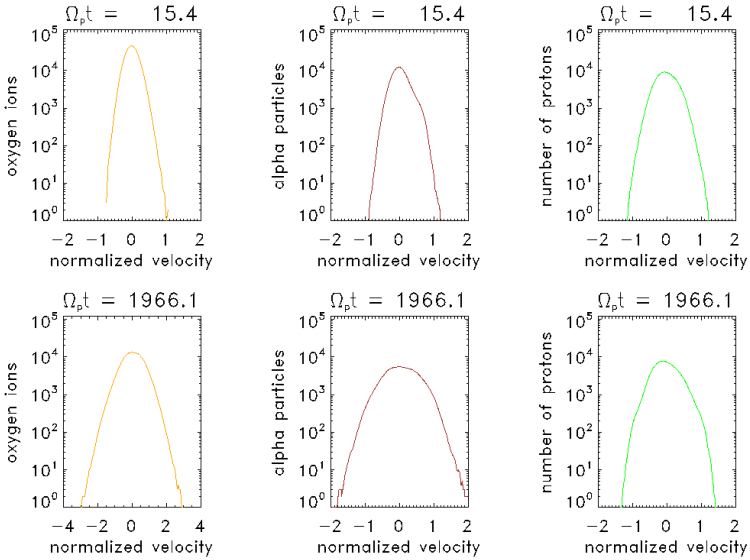


Figure 7.8: Snapshots with the 1D VDFs, similar to Fig. 7.7, but for O^{6+} ions, α particles and protons. Even though their initial states are the same, at the final state O^{6+} ions are much colder than the O^{5+} ions, showing that the preferential heating strongly depends on the charge-to-mass ratio.

higher heating rates correspond to species with lower gyrofrequency.

Fig. 7.7 and Fig. 7.8 show the 1D velocity distribution functions for the 2 types of simulations, including O^{5+} and O^{6+} ion. The plots show the number of particles of a given species with a certain parallel velocity, normalized to the Alfvén speed. Initially we consider the same thermal speed for the two oxygen ionization states, which are additionally assumed to be colder than the protons and the α particles (see Section 7.1). At the early stage, the protons appear to be warmest, but soon after, the minor ions are preferentially heated. In the end, the O VI acquires huge parallel temperature, followed by O VII, the α particles and the protons (see also Fig. 7.11 and Fig. 7.12). We should note, that in this case the proton beams are very dynamic. They form at an early stage, but the backward propagating daughter waves decelerate them back to the core, so that in the end no prominent beams are present in the distributions.

Fig. 7.9 and Fig. 7.10 compare the acceleration rates for the two different ionization states of oxygen ions. The relative drift between protons and α particles in those two cases remains almost the same. The oxygen O^{6+} ions, however, acquire higher speeds than the O^{5+} , but it is only temporary that their bulk speed exceeds that of He^{2+} and in the end, they stream with the same rate as the α particles.

Fig. 7.11 shows that the bulk of the protons gets preferentially heated in parallel direction, whereas for the α particles, perpendicular heating prevails. The temperature anisotropies

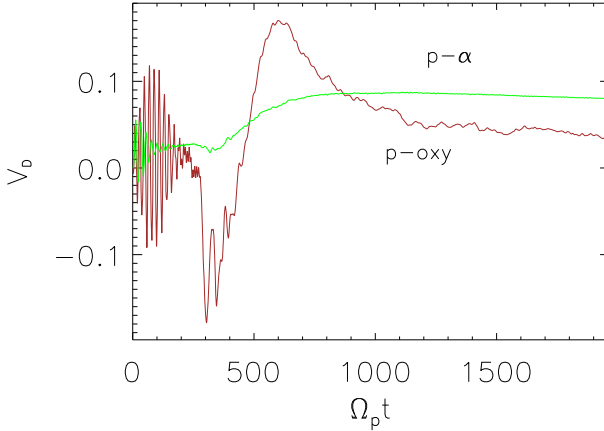


Figure 7.9: Temporal evolution of the relative drifts between the protons and the α particles (given in green), and the protons and the oxygen VI ions (brown colour). All velocities are normalized to the local Alfvén speed. The plot demonstrates that the α particles in this case accelerate faster than the O^{5+} . The prominent initial oscillations are caused by the pump wave. The minimum of the relative streaming between protons and oxygen ions around $\Omega_p t = 300$ (where $V_{\alpha p}$ slightly decreases and $V_{p\text{oxy}}$ takes negative values) appears as the protons accelerate and start to move faster (not faster than the α particles, though). Afterwards the oxygen goes quickly ahead, but around $\Omega_p t = 600$ it undergoes a transition and gradually slows down again. Thus in the final state the α particles are the fastest.

for the heavy ions exhibit rather different features, caused by their different response to the Lorenz force of the pump. The apparent initial anisotropy for the Oxygen VI ions, thus, reaches as far as 1400, but within 100 timesteps only it already reduces to 100 and, after another 200 timesteps, it saturates towards its final value of $(T_{\perp}/T_{\parallel})_{O^{5+}} \approx 1.45$. The initial apparent anisotropy of the Oxygen VII ions also performs fastly damping oscillations. It starts at 40, after a hundred timesteps it drops to 15 and after $\Omega_p t = 300$ it almost saturates at its final value of $(T_{\perp}/T_{\parallel})_{O^{6+}} \approx 1.75$.

Fig. 7.12 presents the parallel and perpendicular kinetic temperature components for the 2 heavy ion species. Both oxygen ions are clearly preferentially heated in perpendicular direction, with the O^{5+} ions being about an order of magnitude hotter than the O^{6+} ions.

Simulations confirm that, due to their low mass densities and charge-to-mass ratios, heavy ions are preferentially heated and become more anisotropic. It is important to notice that the temperature ratios of oxygen ions, α particles and the protons exceed their mass ratios, $T_h/T_p > m_h/m_p$, as found by analyses of Ulysses spacecraft data [von Steiger *et al.* (1995)]. This is a robust feature, which also comes out from the 2 species (proton – α particles) simulations, presented in the previous two Chapters 5 and 6. It is consistent both with resonant heating and quasi-linear diffusion or nonlinear wave-particle

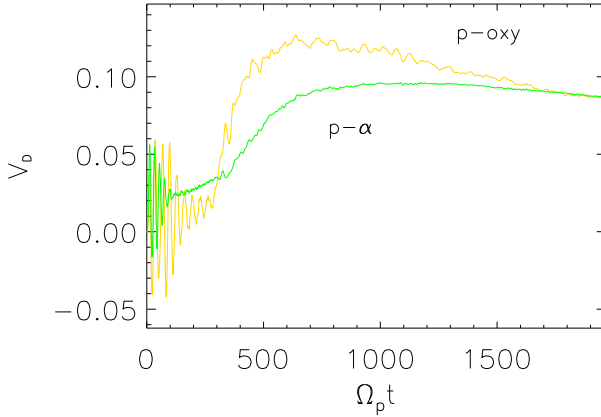


Figure 7.10: The same format for the temporal evolution of the normalized relative drifts like on Fig. 7.9, but in this case O^{6+} was used as a heavy ion specie. As the initial wave frequency is closest to the oxygen gyrofrequency, the α particles and the protons stop oscillating in the electromagnetic field of the pump much earlier than the oxygen ions (true for both ionization states). The α particles start to accelerate first, but are soon overtaken by the heavy ions. In the end the 2 minor species stream at the same rate.

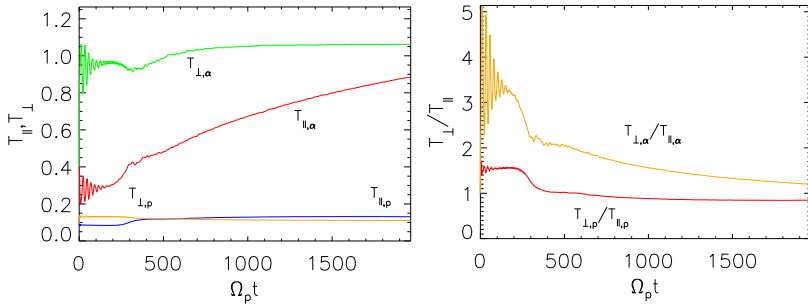


Figure 7.11: Left panel: Parallel and perpendicular components of the kinetic temperature for protons and α particles. Right panel: Temporal evolution of the temperature anisotropy for protons and α particles. Both plots correspond to the simulations with oxygen VI as a heavy species. However, the results for the case when oxygen VII is used instead, show no change in the behavior of the light species and both temperatures and anisotropies for the protons and the α particles remain the same.

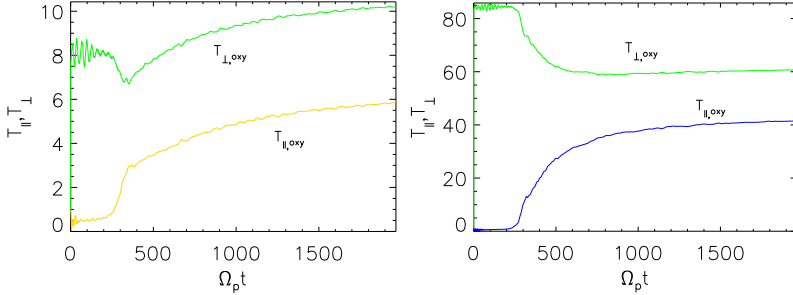


Figure 7.12: Parallel and perpendicular temperatures for the Oxygen VI (to the left) and Oxygen VII ions (on the right panel).

scattering after an initial coherent state with a large transverse bulk velocity, as shown in this work. Furthermore, it is important to stress the influence of the charge-to-mass ratio on the ion dynamics in the presence of a non-linear pump wave. Thus if we consider pump waves obeying the self-consistent dispersion relation Eq. (4.24) corresponding to the same initial conditions (like number densities, drifts and thermal speeds), and if those pump waves are closer to resonance with O^{5+} ions, then the latter will be more strongly heated and their velocity distributions will differ a lot from that of the O^{6+} ions. This is due to the different resonance kinematics of the two ionization states which determines their different response first to the pump itself and later to the turbulent spectra of the daughter waves. In relation to the behavior of the observed coronal O^{5+} ions, we have to mention that under the lower β conditions in coronal holes those ions can be even more easily heated. In addition, we should comment, that the strong oxygen ions anisotropies (about 80-100), as reported by the UVCS team [Kohl *et al.* (1998)] are hardly supposed to be stable. Hence, if not due to line of sight integration [Raouafi and Solanki (2006)], they could be interpreted and attributed to large-amplitude Alfvén-cyclotron waves.

The results from this chapter show, that, if put under the same conditions, the two different ionization states of oxygen ions react to the pump wave in a very different manner (see Eq. (4.26)). But we should note, that initial parallel relative drifts would strongly influence the ion dynamics and change the final heating rates. Based on the conclusions from the previous Chapter 6, we should also mention that it might be more meaningful to initialize the simulations with smaller values of the plasma $\tilde{\beta}_s$ and then compare the results to the observations at 1 AU, as the main heating process starts much earlier, closer to the Sun. Such a comparison is left for a future investigation.

8 Conclusions and outlook

A general introduction into the solar corona and solar wind, with emphasis on the collisionless low-density plasma conditions prevailing in CHs and the fast solar wind, as well as a demonstration of their ubiquitous Alfvénic fluctuations, was presented in Chapter 1. Chapter 2 guided us through the plasma kinetics in CHs and fast solar wind, demonstrating the observed preferential heating and acceleration of heavier ions and the in situ measured nonthermal ion VDFs.

Chapter 3 gave an insight into the parametric instabilities of monochromatic large-amplitude Alfvén-cyclotron waves propagating parallel to a homogeneous background magnetic field. Kinetic effects in parallel direction were introduced to account for wave-particle interactions, involving Landau damping. Still, the investigated dispersion relations are fluid in transverse direction, so that no cyclotron damping effects are taken into account. A dispersion relation, describing the growth rates of both longitudinal and transverse electromagnetic daughter fluctuations, due to the parametric instabilities of the nonlinear pump wave, was derived for a collisionless quasi-neutral, free-of-currents plasma, that is composed of fluid electrons and an arbitrary number of kinetic ion species. The simplest example of a non-drifting electron-proton plasma is given as a test case in the beginning, followed by the dispersion for the special case of parallelly streaming α particles. Finally, O^{+5} ions are included explicitly, with and without relative drifts, to give an example of the evolution of parametric instabilities in the presence of heavy ions. This Chapter brings new insight into the plasma instabilities, when nonlinear monochromatic waves are present in a collisionless homogeneous multi-species plasma.

Chapter 4 introduced the notion of PIC and hybrid codes, and described the numerical methods, used to investigate the kinetic behavior of the solar plasma. We discussed both the physical background and the numerical issues of the initial setup for the numerical simulations. A comparison of some of the numerical results with the theoretical description of parametric instabilities of Alfvén-cyclotron waves, as presented in Chapter 3, shows that the theory can adequately describe the decay of large-amplitude pump waves and the consequent growth of the daughter waves (at least for the longitudinal, ion-acoustic daughter fluctuations).

Chapter 5 showed the effect of large-amplitude Alfvén-cyclotron waves on the ion VDFs. The decay of the pump leads to preferential heating and acceleration of the minor ions, via Landau damping of daughter IAWs and nonlinear pitch-angle scattering by the daughter Alfvén-cyclotron waves. As a result, all ion species acquire nonthermal features in their velocity distributions. Additionally, we have investigated how the heating and acceleration rates change in the presence of differential streaming between the protons and α particles. We demonstrated the results obtained for four different regimes in the values of the initial relative drift speed, showing continuous acceleration (for $V_{ap,in} < 0.5V_A$),

no change of the drift speed (at $V_{\alpha p, \text{in}} = 0.5V_A$), continuous deceleration (for $0.5V_A < V_{\alpha p, \text{in}} < v_{\text{ph}}$) and retarded deceleration of the minor species (for $V_{\alpha p, \text{in}} > v_{\text{ph}}$). In the first regime, the α particles are accelerated to a significant fraction of the local Alfvén speed (up to $0.5V_A$). Generally, they sit between the proton core and the proton beam, similar to what is observed in the fast solar wind. The proton beams in the simulations travel typically at a speed $v_b \in [0.7, 1.3]V_A$, depending on the magnitude of the relative drift speed $V_{\alpha p}$.

A statistical parameter study on the behavior of protons and α particles for a different range of initial relative drifts and plasma $\tilde{\beta}_s$, was presented in Chapter 6. The results show that the ion differential acceleration strongly depends on the values of the initial plasma $\tilde{\beta}_s$: the higher the $\tilde{\beta}_s$, the harder it is to accelerate the ions to a high value of the relative drift speed $V_{\alpha p}$. In addition, the heating rate for the ion species depends on the value of the relative drift speed. For the given frequency and wave-number of the pump, it is easier to heat the protons at higher relative drifts, and the opposite is true for the α particles. Apart from the relative drifts, the heating rate also depends on the initial kinetic temperature of the species. In general, it seems easier to heat the ions in a very low $\tilde{\beta}_s$ regime. However, things are more complicated, as the heating rate for a single species depends on the plasma $\tilde{\beta}_s$ values for both species. Still, we can summarize that in our model simultaneous strong heating and acceleration occur in a low $\tilde{\beta}_s$ domain, whereas, as the temperature of the ion species increases, the wave-particle interaction keeps on heating the particles (the protons preferably at higher drifts, the α particles at lower), but the differential acceleration is much less.

From these results we can conclude that by dissipation of nonlinear Alfvén-cyclotron wave energy one cannot accelerate the α particles to a very high value of the relative drift speed, neither in low (when the wind is still close to the Sun), nor in high plasma $\tilde{\beta}_s$ conditions. In our study the maximal particle acceleration that can be reached yields $V_{\alpha p} = 0.5V_A$, as typically observed in the fast solar wind. To generate the high relative drifts between protons and α particles as observed near the Earth and beyond, one has to invoke a different process, like, for instance, the sweeping mechanism as the Alfvén speed (following the magnitude of the magnetic field) decreases with increasing distance from the Sun, and hence the normalized relative drift effectively increases. High relative drifts can be acquired also at the boundary surface where the fast and the slow wind streams meet.

Chapter 7 considers two different ionization states of oxygen ions as representative examples for heavy ion species in CHs and fast solar wind plasma. The results show that for the given initial conditions the heavy ions are much more affected by the electromagnetic field of the pump Alfvén-cyclotron wave than both the protons and the α particles (as demonstrated for a non-drifting plasma) and their heating rate depends strongly on their gyration frequency. As a rule, in a non-drifting plasma, the lower ionization states of a given ion species are to acquire higher heating rates, as demonstrated for the case of O^{+5} and O^{+6} ions. Simulations suggest that the same is valid for carbon ions as well, though these results are excluded from the present analysis. We should note, however, that higher heating rate is not always related to higher acceleration. Thus, the O^{+5} ions, which reach up to $V_{\text{oxyp}} \sim 0.035V_A$, in our model are a little bit slower than the O^{+6} ions, which accelerate to about $V_{\text{oxyp}} \sim 0.09V_A$. Those values are still very low and the minor α species in both cases do not gain high drifts either. That supports the idea that the ion differen-

tial heating and acceleration probably takes place much closer to the Sun or already in the solar corona. Therefore this issue requires additional investigation, like, for example, performing simulations with a smaller initial plasma $\tilde{\beta}_s$ or different pump-wave number and frequency.

To conclude the results from all chapters, we have shown that in the course of their evolution the velocity distribution functions of all ion species exhibit nonthermal features (related to anisotropic heating and/or ion beam formation). In addition, as demonstrated in Chapter 7, in a high $\tilde{\beta}$ regime, the heavy ions are preferentially heated, though not necessarily preferentially accelerated when we initialize the simulations with relatively large initial plasma $\tilde{\beta}_s$, supporting the idea that such processes take place closer to the Sun, where $\tilde{\beta}_s \ll 1$. Furthermore, both the heating and acceleration rates strongly depend on the charge-to-mass ratio of the given ion species and on the properties of the pump wave. Finally, a more than mass proportional heating rate, giving $T_h/T_p > m_h/m_p$, is observed for all species for all the investigated different initial plasma conditions.

In order to evaluate the relevance of the proposed model to the ion differential heating and acceleration in the solar corona and the fast solar wind, we have to keep in mind our model restrictions, and think about possible improvements as a future scope. Major simplifications of our model are the use of 1D geometry with a homogeneous background magnetic field and the assumption of parallel wave propagation of monochromatic waves only. In this relation, it might be interesting to investigate the effects of wave spectra in an expanding box model, following the expansion of the solar wind and see how those would reflect on the differential heating and acceleration. However, it is not easy to construct a proper self-consistent set of wave-spectra, which might be used to initialize the simulations. Thus, this issue still remains an open problem for a future work.

In addition, gravitational stratification might be taken into account, though there are implications that inclusion of gravity would not quantitatively alter the main results of our research. It is important, though, to perform 2D or 3D hybrid simulations and allow for an oblique propagation as well, as this would allow for additional wave-wave couplings, change the character of the plasma instabilities and might substantially affect the response of the ions and their velocity distribution functions. Nevertheless, the results from such a research would be difficult to interpret without the necessary basic knowledge on the physical processes in the 1D case, subject of the present dissertation.

Finally, it is interesting to analytically investigate parametric instabilities, including cyclotron damping and possibly study the effects of inhomogeneities on the wave couplings and the wave-particle interactions in space plasmas.

A Kinetic dispersion relation for the pump wave - Sonnerup's solution

Here we shortly present the specific type of the pump wave dispersion relation, used for the calculation of the pump wave frequency in the initial simulation setup. From purely mathematical point of view it resembles the cold plasma dispersion relation (the linear kinetic dispersion relation for a parallel wave propagation in a cold homogenous collisionless plasma, as given for example by [R. Davidson (1983)]. However, we should emphasize that the solution, described here (originally found by [Sonnerup and Su (1967)]), is fully nonlinear (not restricted to small wave amplitudes) and is valid for a parallel propagation in a warm homogeneous kinetic plasma. In fact, it should not be considered as a classical dispersion relation (used to analyse plasma instabilities), but rather as a relation between the pump frequency and the wave-number (i.e. only the real part of the dispersion relation should be considered, regardless what are the associated growth rates, as the linear theory analysis breaks down in the presence of large-amplitude waves and hence for the instabilities analyses one needs to perform a more elaborated study, based on parametric instabilities, for example).

For an arbitrary number of species gives the general form of the pump wave dispersion relation reads

$$k^2 - \frac{\omega^2}{c^2} + \frac{1}{c^2} \sum_s \omega_{ps}^2 \frac{\omega - kV_s}{\omega - kV_s - \Omega_s} = 0. \quad (\text{A.1})$$

If we now consider a non-relativistic plasma $\omega^2 \ll k^2 c^2$, assume both charge and current conservation, and concentrate on the low frequency modes far below the electron gyration $\omega \ll \Omega_e$, we obtain

$$k^2 c^2 + \sum_{i \neq e} \frac{\omega_{pi}^2}{\Omega_i} \left[\frac{(\omega - kV_i)^2}{\omega - kV_i - \Omega_i} \right] = 0. \quad (\text{A.2})$$

Actually we are interested in Alfvén-cyclotron waves with frequencies even below the lowest ion gyro-frequency, as above it the validity of Sonnerup's solution for right-handed modes breaks down. If we now consider a plasma consisting of fast fluid electrons and 3 ion species: protons, α particles and 5 times ionized oxygen ions O^{5+} , Sonnerup's solution turns into

$$\frac{\omega_{pp}^2}{\Omega_p} \frac{(\omega - kV_p)^2}{\omega - kV_p - \Omega_p} + \frac{\omega_{p\alpha}^2}{\Omega_\alpha} \frac{(\omega - kV_\alpha)^2}{\omega - kV_\alpha - \Omega_\alpha} + \frac{\omega_{pO5}^2}{\Omega_{O5}} \frac{(\omega - kV_{O5})^2}{\omega - kV_{O5} - \Omega_{O5}} + k^2 c^2 = 0.$$

To be able to directly implement the wave in the numerical simulation we normalize all the frequencies to the proton cyclotron frequency Ω_p and all velocities to the Alfvén speed $V_A^2 \equiv B_0^2/4\pi n_e m_p$. In this way we have

$$\begin{aligned} & \frac{k^2 V_A^2}{\Omega_p^2} + \frac{\omega_{pp}^2 V_A^2}{\Omega_p^2} \frac{(\omega/\Omega_p - kV_p/\Omega_p)^2}{c^2 \omega/\Omega_p - kV_p/\Omega_p - 1} \\ & + \frac{\omega_{p\alpha}^2 V_A^2 \Omega_p}{\Omega_p^2 c^2 \Omega_\alpha} \frac{(\omega/\Omega_p - kV_\alpha/\Omega_p)^2}{\omega/\Omega_p - kV_\alpha/\Omega_p - \Omega_\alpha/\Omega_p} \\ & + \frac{\omega_{p\alpha}^2 V_A^2 \Omega_p}{\Omega_p^2 c^2 \Omega_{\alpha 5}} \frac{(\omega/\Omega_p - kV_{\alpha 5}/\Omega_p)^2}{\omega/\Omega_p - kV_{\alpha 5}/\Omega_p - \Omega_{\alpha 5}/\Omega_p} = 0. \end{aligned} \quad (\text{A.3})$$

If we take into account the relation

$$\frac{\omega_{ps}^2 V_A^2}{\Omega_s^2 c^2} = \frac{n_p n_s m_s}{n_e n_p m_p} \quad (\text{A.4})$$

and introduce the auxiliary dimensionless notations for the normalized densities, charges, frequencies, wave-vectors and drift velocities

$$\begin{aligned} \eta_s &\equiv \frac{n_s}{n_p}, & Q_s &\equiv \frac{q_s}{e}, & X &\equiv \frac{\omega}{\Omega_p}, \\ R_s &\equiv \frac{\Omega_p}{\Omega_s}, & Y &\equiv \frac{kV_A}{\Omega_p}, & U_i &\equiv \frac{V_i}{V_A} \end{aligned} \quad (\text{A.5})$$

the dispersion relation can be written in the way

$$Y^2 + \frac{1}{\eta_e} \left[\frac{(X - U_p Y)^2}{X - U_p Y - 1} + \eta_\alpha Q_\alpha \frac{(X - U_\alpha Y)^2}{X - U_\alpha Y - 1/R_\alpha} + \eta_{\alpha 5} Q_{\alpha 5} \frac{(X - U_{\alpha 5} Y)^2}{X - U_{\alpha 5} Y - 1/R_{\alpha 5}} \right] = 0.$$

When we substitute the numerical values for the charge and frequency ratios we come to the final form:

$$Y^2 + \frac{1}{\eta_e} \left[\frac{(X - U_p Y)^2}{X - U_p Y - 1} + 2\eta_\alpha \frac{(X - U_\alpha Y)^2}{X - U_\alpha Y - 1/2} + 5\eta_{\alpha 5} \frac{(X - U_{\alpha 5} Y)^2}{X - U_{\alpha 5} Y - 5/16} \right] = 0. \quad (\text{A.6})$$

In order to initialize the simulations we solve this relation numerically and select the pump from a single point, corresponding to the normalized wave number $k_0 = 0.4\Omega_p/V_A$. In the case that we want to simulate solar plasma, consisting of electrons, protons and alpha particles only, naturally we have to omit the last term in the dispersion relation. Similar analysis can be made for a different kind of heavy ions (like O^{6+} , C^{5+} or C^{6+} , for instance), which will reflect on the last term in Eq. (A.6) again.

Bibliography

- Alfvén, H., 1942, Existence of Electromagnetic-Hydrodynamic Waves, *Nature*, 150, 405–406
- Araneda, J. A., 1998, Parametric Instabilities of Parallel-Propagating Alfvén Waves: Kinetic Effects in the MHD-Model, *Physica Scripta Volume T*, 75, 164–168
- Araneda, J. A., Gomberoff, L., 2004, Stabilization of right-hand polarized beam plasma instabilities due to a large-amplitude left-hand polarized wave: A simulation study, *Journal of Geophysical Research (Space Physics)*, 109, 1106
- Araneda, J. A., Marsch, E., Viñas, A. F., 2007, Collisionless damping of parametrically unstable Alfvén waves, *J. Geophys. Res. (Space Physics)*, 112, 4104
- Araneda, J. A., Marsch, E., F.-Viñas, A., 2008, Proton Core Heating and Beam Formation via Parametrically Unstable Alfvén-Cyclotron Waves, *Physical Review Letters*, 100, 125 003
- Araneda, J. A., Maneva, Y., Marsch, E., 2009, Preferential Heating and Acceleration of α Particles by Alfvén-Cyclotron Waves, *Physical Review Letters*, 102, 175 001
- Aschwanden, M. J., 2005, *Physics of the Solar Corona. An Introduction with Problems and Solutions* (2nd edition)
- Astudillo, H. F., Marsch, E., Livi, S., Rosenbauer, H., 1995, Non-gyrotropic proton and alpha-particle velocity distributions in the solar wind: TAUS observations and stability analysis, in *Solar Wind 8*, p. 74
- Astudillo, H. F., Livi, S., Marsch, E., Rosenbauer, H., 1996, Evidence for nongyrotropic alpha particle and proton distribution functions: TAUS solar wind measurements, *J. Geophys. Res.*, 101, 24 423–24 432
- Bale, S. D., Kasper, J. C., Howes, G. G., Quataert, E., Salem, C., Sundkvist, D., 2009, Magnetic Fluctuation Power Near Proton Temperature Anisotropy Instability Thresholds in the Solar Wind, *Physical Review Letters*, 103, 211 101
- Banerjee, D., Pérez-Suárez, D., Doyle, J. G., 2009, Signatures of Alfvén waves in the polar coronal holes as seen by EIS/Hinode, *Astron. Astrophys.*, 501, L15–L18
- Baumjohann, W., Treumann, R., 1996, *Basic Space Plasma Physics*, Imperial College Press; World Scientific, London, U.K.; River Edge, U.S.A.

- Belcher, J. W., Davis, Jr., L., 1971, Large-amplitude Alfvén waves in the interplanetary medium, 2., *J. Geophys. Res.*, 76, 3534–3563
- Belcher, J. W., Solodyna, C. V., 1975, Alfvén waves and directional discontinuities in the interplanetary medium, *J. Geophys. Res.*, 80, 181–186
- Berger, L., Wimmer-Schweingruber, R. F., Gloeckler, G., 2010, 3D velocity distribution functions of heavy ions and kinetic properties of O^{6+} at 1 AU, Twelfth International Solar Wind Conference, 1216, 253–256
- Birdsall, C. K., Langton, A. B., 2004, Plasma physics via computer simulation
- Bourouaine, S., Marsch, E., Vocks, C., 2008, On the Efficiency of Nonresonant Ion Heating by Coronal Alfvén Waves, *Astrophys. J. Lett.*, 684, L119–L122
- Boyd, T. J. M., Sanderson, J. J., 1969, Plasma dynamics
- Braginskii, S., 1965, Transport processes in plasma, in *Review of Plasma Physics*, (Ed.) M. Leontovich, vol. 1 of *Review of Plasma Physics*, pp. 201–311, Consultants Bureau, New York, U.S.A.
- Briand, C., 2009, Plasma waves above the ion cyclotron frequency in the solar wind: a review on observations, *Nonlinear Processes in Geophysics*, 16, 319–329
- Bruno, R., Carbone, V., 2005, The solar wind as a turbulence laboratory, *Living Rev. Solar Phys.*, 2
- Bruno, R., Bavassano, B., Villante, U., 1985, Evidence for long period Alfvén waves in the inner solar system, *J. Geophys. Res.*, 90, 4373–4377
- Chapman, S., Tandberg-Hanssen, E., 1958, Thermal Diffusion at High Temperatures in Ionized Gases, in *Conference on Extremely High Temperatures*, (Ed.) H. Fischer & L. C. Mansur, p. 139
- Cohen, C. M. S., Collier, M. R., Hamilton, D. C., Gloeckler, G., Sheldon, R. B., von Steiger, R., Wilken, B., 1996, Kinetic temperature ratios of O^{6+} and He^{2+} : Observations from Wind/MASS and Ulysses/SWICS, *Geophys. Res. Lett.*, 23, 1187–1190
- Cranmer, S. R., Field, G. B., Kohl, J. L., 1999, Spectroscopic Constraints on Models of Ion Cyclotron Resonance Heating in the Polar Solar Corona and High-Speed Solar Wind, *Astrophys. J.*, 518, 937–947
- Davidson, R. C., 1972, *Methods in Nonlinear Plasma Theory*
- Davidson, R. C., 1983, Kinetic waves and instabilities in a uniform plasma, in *Basic Plasma Physics: Selected Chapters, Handbook of Plasma Physics, Volume 1*, (Ed.) A. A. Galeev & R. N. Sudan, p. 229
- De Pontieu, B., McIntosh, S. W., Carlsson, M., Hansteen, V. H., Tarbell, T. D., Schrijver, C. J., Title, A. M., Shine, R. A., Tsuneta, S., Katsukawa, Y., Ichimoto, K., Suematsu, Y., Shimizu, T., Nagata, S., 2007, Chromospheric Alfvénic Waves Strong Enough to Power the Solar Wind, *Science*, 318, 1574

- Derby, Jr., N. F., 1978, Modulational instability of finite-amplitude, circularly polarized Alfvén waves, *Astrophys. J.*, 224, 1013–1016
- Dolla, L., Solomon, J., Lemaire, P., 2004, A Search for Signatures of Preferential Heating by Ion Cyclotron Waves in the Low Corona, in *SOHO 13 Waves, Oscillations and Small-Scale Transients Events in the Solar Atmosphere: Joint View from SOHO and TRACE*, (Ed.) H. Lacoste, vol. 547 of ESA Special Publication, p. 391
- Erdélyi, R., Fedun, V., 2007, Are There Alfvén Waves in the Solar Atmosphere?, *Science*, 318, 1572
- Galeev, A., Sagdeev, R., 1989, Wave-particle interaction., in *Basic Plasma Physics. Selected chapters. Handbook of plasma physics. Vol. 1 and 2*, Amsterdam: Elsevier 1989, (Ed.) Galeev, A. A. & Sudan, R. N., p. 393
- Galeev, A. A., Oraevskii, V. N., 1963, The Stability of Alfvén Waves, *Soviet Physics Doklady*, 7, 988
- Galeev, A. A., Sudan, R. N., 1989, Basic plasma physics. Selected chapters. Handbook of plasma physics. Vol. 1 and 2.
- Gary, G. A., 2001, Plasma Beta above a Solar Active Region: Rethinking the Paradigm, *Solar Phys.*, 203, 71–86
- Gary, S. P., Yin, L., Winske, D., 2000a, Constraints on Ion Temperature Anisotropies: Solar Wind and Solar Corona, *APS Meeting Abstracts*, p. 1004P
- Gary, S. P., Yin, L., Winske, D., Reisenfeld, D. B., 2000b, Alpha/proton magnetosonic instability in the solar wind, *J. Geophys. Res.*, 105, 20 989–20 996
- Gary, S. P., Goldstein, B. E., Neugebauer, M., 2002, Signatures of wave-ion interactions in the solar wind: Ulysses observations, *Journal of Geophysical Research (Space Physics)*, 107, 1169
- Gary, S. P., Skoug, R. M., Smith, C. W., 2005a, Learning about coronal heating from solar wind observations, *Physics of Plasmas*, 12, 056 501
- Gary, S. P., Smith, C. W., Skoug, R. M., 2005b, Signatures of Alfvén-cyclotron wave-ion scattering: Advanced Composition Explorer (ACE) solar wind observations, *Journal of Geophysical Research (Space Physics)*, 110, 7108
- Goldstein, M. L., 1978, An instability of finite amplitude circularly polarized Alfvén waves, *Astrophys. J.*, 219, 700–704
- Gomberoff, L., 2003, Stabilization of linear ion beam right-hand polarized instabilities by nonlinear Alfvén/ion-cyclotron waves, *Journal of Geophysical Research (Space Physics)*, 108, 1261
- Gosling, J. T., 2007, Solar wind, in *Encyclopedia of the Solar System, Second Edition*, (Eds.) L.-A. McFladden, P. R. Weissman, T. V. Johnson, p. 114, Elsevier, London, U.K.; San Diego, U.S.A.

- He, J., Tu, C., Marsch, E., Guo, L., Yao, S., Tian, H., 2009, Upward propagating high-frequency Alfvén waves as identified from dynamic wave-like spicules observed by SOT on Hinode, *Astron. Astrophys.*, 497, 525–535
- Hollweg, J. V., 1994, Beat, modulational, and decay instabilities of a circularly polarized Alfvén wave, *J. Geophys. Res.*, 99, 23 431
- Hollweg, J. V., Isenberg, P. A., 2002, Generation of the fast solar wind: A review with emphasis on the resonant cyclotron interaction, *Journal of Geophysical Research (Space Physics)*, 107, 1147
- Hollweg, J. V., Esser, R., Jayanti, V., 1993, Modulational and decay instabilities of Alfvén waves - Effects of streaming He(2+), *J. Geophys. Res.*, 98, 3491–3500
- Horowitz, E. J., Shumaker, D. E., Anderson, D. V., 1989, QN3D: A Three-Dimensional Quasi-neutral Hybrid Particle-in-Cell Code with Applications to the Tilt Mode Instability in Field Reserved Configurations, *Journal of Computational Physics*, 84, 279
- Inhester, B., 1990, A drift-kinetic treatment of the parametric decay of large-amplitude Alfvén waves, *J. Geophys. Res.*, 95, 10 525–10 539
- Jess, D. B., Mathioudakis, M., Erdélyi, R., Crockett, P. J., Keenan, F. P., Christian, D. J., 2009, Alfvén Waves in the Lower Solar Atmosphere, *Science*, 323, 1582
- Jian, L. K., Russell, C. T., Luhmann, J. G., Strangeway, R. J., Leisner, J. S., Galvin, A. B., 2009, Ion Cyclotron Waves in the Solar Wind Observed by STEREO Near 1 AU, *Astrophys. J. Lett.*, 701, L105–L109
- Kasper, J. C., Lazarus, A. J., Gary, S. P., 2008, Hot Solar-Wind Helium: Direct Evidence for Local Heating by Alfvén-Cyclotron Dissipation, *Physical Review Letters*, 101, 261 103
- Kauffmann, K., Araneda, J. A., 2008, Parametric instabilities of Alfvén waves in a multi-species plasma: Kinetic effects, *Physics of Plasmas*, 15, 062 106
- Kohl, J. L., Noci, G., Antonucci, E., Tondello, G., Huber, M. C. E., Cranmer, S. R., Strachan, L., Panasyuk, A. V., Gardner, L. D., Romoli, M., Fineschi, S., Dobrzycka, D., Raymond, J. C., Nicolosi, P., Siegmund, O. H. W., Spadaro, D., Benna, C., Ciarravella, A., Giordano, S., Habbal, S. R., Karovska, M., Li, X., Martin, R., Michels, J. G., Modigliani, A., Naletto, G., O’Neal, R. H., Pernechele, C., Poletto, G., Smith, P. L., Suleiman, R. M., 1998, UVCS/SOHO Empirical Determinations of Anisotropic Velocity Distributions in the Solar Corona, *Astrophys. J. Lett.*, 501, L127
- Kohl, J. L., Noci, G., Cranmer, S. R., Raymond, J. C., 2006, Ultraviolet spectroscopy of the extended solar corona, *Astron. Astrophys. Rev.*, 13, 31–157
- Lapenta, G., Particle in Cell, in SOLAIRE PostGraduate School on Computational Methods in Astrophysics: Bochum, March 3-14, 2008
- Lapenta, G., Brackbill, J. U., Ricci, P., 2006, Kinetic approach to microscopic-macroscopic coupling in space and laboratory plasmas, *Physics of Plasmas*, 13, 055 904

- Li, X., Habbal, S. R., 2005, Hybrid simulation of ion cyclotron resonance in the solar wind: Evolution of velocity distribution functions, *J. Geophys. Res.*, 110, 10 109
- Maneva, Y. G., Araneda, J. A., Marsch, E., 2009, Parametrically Unstable Alfvén-cyclotron Waves and Wave-Particle Interactions in the Solar Corona and Solar Wind, in *American Institute of Physics Conference Series*, (Ed.) I. Zhelyazkov, vol. 1121 of *American Institute of Physics Conference Series*, pp. 122–126
- Maneva, Y. G., Araneda, J. A., Marsch, E., 2010, Ion distributions in coronal holes and fast solar wind, *Twelfth International Solar Wind Conference*, 1216, 227–230
- Marsch, E., 1991, *Kinetic Physics of the Solar Wind Plasma*, pp. 45–133
- Marsch, E., 2006, *Kinetic Physics of the Solar Corona and Solar Wind*, *Living Reviews in Solar Physics*, 3, 1–100
- Marsch, E., Tu, C., 2001a, Heating and acceleration of coronal ions interacting with plasma waves through cyclotron and Landau resonance, *J. Geophys. Res.*, 106, 227–238
- Marsch, E., Tu, C., 2001b, Evidence for pitch angle diffusion of solar wind protons in resonance with cyclotron waves, *J. Geophys. Res.*, 106, 8357–8362
- Marsch, E., Mühlhäuser, K.-H., Schwenn, R., Rosenbauer, H., Pilipp, W., Neubauer, F., 1982, Solar wind protons: Three-dimensional velocity distributions and derived plasma parameters measured between 0.3 and 1 au, *J. Geophys. Res.*, 87, 52–72
- Marsch, E., Rosenbauer, H., Schwenn, R., Muehlhaeuser, K., Neubauer, F. M., 1982, Solar wind helium ions - Observations of the HELIOS solar probes between 0.3 and 1 AU, *J. Geophys. Res.*, 87, 35–51
- Marsch, E., Vocks, C., Tu, C.-Y., 2003, On ion-cyclotron-resonance heating of the corona and solar wind, *Nonlinear Processes in Geophysics*, 10, 101–112
- Mathews, A. P., 1994, Current Advance Method and Cyclic Leapfrog for 2D Multispecies Hybrid Plasma Simulations, *Journal of Computational Physics*, 112, 102–116
- McComas, D. J., Ebert, R. W., Elliott, H. A., Goldstein, B. E., Gosling, J. T., Schwadron, N. A., Skoug, R. M., 2008, Weaker solar wind from the polar coronal holes and the whole Sun, *Geophys. Res. Lett.*, 35, 18 103
- Melrose, D. B., 1986, *Instabilities in Space and Laboratory Plasmas*
- Nariyuki, Y., Hada, T., 2007, Consequences of finite ion temperature effects on parametric instabilities of circularly polarized Alfvén waves, *Journal of Geophysical Research (Space Physics)*, 112, 10 107
- Nariyuki, Y., Hada, T., Tsubouchi, K., 2007, Parametric instabilities of parallel propagating incoherent Alfvén waves in a finite ion beta plasma, *Physics of Plasmas*, 14, 122 110

- Nariyuki, Y., Hada, T., Tsubouchi, K., 2009, Parametric instabilities of circularly polarized Alfvén waves in plasmas with beam protons, *Journal of Geophysical Research (Space Physics)*, 114, 7102
- Neugebauer, M., Wu, C. S., Huba, J. D., 1978, Plasma fluctuations in the solar wind, *J. Geophys. Res.*, 83, 1027–1034
- Neugebauer, M., Goldstein, B. E., Smith, E. J., Feldman, W. C., 1996, Ulysses observations of differential alpha-proton streaming in the solar wind, *J. Geophys. Res.*, 101, 17 047–17 056
- Ofman, L., 2010, Hybrid model of inhomogeneous solar wind plasma heating by Alfvén wave spectrum: Parametric studies, *Journal of Geophysical Research (Space Physics)*, 115, 4108
- Ofman, L., Gary, S. P., Viñas, A., 2002, Resonant heating and acceleration of ions in coronal holes driven by cyclotron resonant spectra, *Journal of Geophysical Research (Space Physics)*, 107, 1461
- Parker, E. N., 1958, Suprathermal Particle Generation in the Solar Corona, *Astrophys. J.*, 128, 677
- Raouafi, N., Solanki, S. K., 2006, Sensitivity of solar off-limb line profiles to electron density stratification and the velocity distribution anisotropy, *Astron. Astrophys.*, 445, 735–745
- Sagdeev, R. Z., Galeev, A. A., 1969, *Nonlinear Plasma Theory*, in *Nonlinear Plasma Theory*, New York: Benjamin, 1969, (Ed.) Sagdeev, R. Z. & Galeev, A. A.
- Schwadron, N. A., McComas, D. J., 2003, Solar Wind Scaling Law, *Astrophys. J.*, 599, 1395–1403
- Sonnerup, B. U. Ö., Su, S., 1967, Large Amplitude Whistler Waves in a Hot Collision-Free Plasma, *Physics of Fluids*, 10, 462–464
- Steinberg, J. T., Lazarus, A. J., Ogilvie, K. W., Lepping, R., Byrnes, J., 1996, Differential flow between solar wind protons and alpha particles: First WIND observations, *Geophys. Res. Lett.*, 23, 1183–1186
- Swanson, D. G., 1989, *Plasma waves*.
- Telloni, D., Antonucci, E., Doderò, M. A., 2007a, Outflow velocity of the O⁺⁵ ions in polar coronal holes out to 5 R_s , *Astron. Astrophys.*, 472, 299–307
- Telloni, D., Antonucci, E., Doderò, M. A., 2007b, Oxygen temperature anisotropy and solar wind heating above coronal holes out to 5 R_s , *Astron. Astrophys.*, 476, 1341–1346
- Tomczyk, S., McIntosh, S. W., Keil, S. L., Judge, P. G., Schad, T., Seeley, D. H., Edmondson, J., 2007, Alfvén Waves in the Solar Corona, *Science*, 317, 1192

- Treumann, R. A., Baumjohann, W., 1997, Advanced space plasma physics
- Tu, C., Marsch, E., 1997, Two-Fluid Model for Heating of the Solar Corona and Acceleration of the Solar Wind by High-Frequency Alfvén Waves, *Solar Phys.*, 171, 363–391
- Tu, C., Marsch, E., Qin, Z., 2004, Dependence of the proton beam drift velocity on the proton core plasma beta in the solar wind, *Journal of Geophysical Research (Space Physics)*, 109, 5101
- Tu, C., Zhou, C., Marsch, E., Xia, L., Zhao, L., Wang, J., Wilhelm, K., 2005, Solar Wind Origin in Coronal Funnel, *Science*, 308, 519–523
- Tu, C.-Y., Marsch, E., 1995, Mhd structures, waves and turbulence in the solar wind: Observations and theories, *Space Sci. Rev.*, 73, 1–210
- Unti, T. W. J., Neugebauer, M., 1968, Alfvén Waves in the Solar Wind, *Physics of Fluids*, 11, 563–568
- von Steiger, R., Geiss, J., Gloeckler, G., Galvin, A. B., 1995, Kinetic Properties of Heavy Ions in the Solar Wind From SWICS/Ulysses, *Space Sci. Rev.*, 72, 71–76
- Watanabe, K., Sato, T., 1993, High-precision MHD Simulation, in *Space Plasma Physics: Simulation Techniques & Software*, Tera, Tokyo 1993, (Ed.) H. Matsumoto and Y. Omura, pp. 717–720
- Wiegelmann, T., Solanki, S. K., 2004, Why are Coronal Holes Indistinguishable from the Quiet Sun in Transition Region Radiation?, in *SOHO 15 Coronal Heating*, (Ed.) R. W. Walsh, J. Ireland, D. Danesy, & B. Fleck, vol. 575 of ESA Special Publication, p. 35
- Wiegelmann, T., Xia, L. D., Marsch, E., 2005, Links between magnetic fields and plasma flows in a coronal hole, *Astron. Astrophys.*, 432, L1–L4
- Wimmer-Schweingruber, R. F., Von Steiger, R., Geiss, J., Gloeckler, G., Ipavich, F. M., Wilken, B., 1998, O^{5+} in High Speed Solar Wind Streams: SWICS/Ulysses Results, *Space Sci. Rev.*, 85, 387–396
- Winske, D., Omid, N., 1993, Hybrid codes: Methods and applications, in *Space Plasma Physics: Simulation Techniques & Software*, Tera, Tokyo 1993, (Ed.) Matsumoto, H. & Omura, Y.
- Wu, C. S., Yoon, P. H., Wang, C. B., 2009, On nonresonant proton heating via intrinsic Alfvénic turbulence, *Physics of Plasmas*, 16, 054503
- Yoon, P. H., Fang, T., 2009, Proton heating by parallel Alfvén wave cascade, *Physics of Plasmas*, 16, 062314

Publications

Publications in refereed scientific journals

- J. Araneda, Y. Maneva and E. Marsch, “Preferential Heating and Acceleration of α Particles by Alfvén-Cyclotron Waves”, 2009, *PRL*, vol. 102, p.175001.
- Todor M. Mishonov, Yana G. Maneva, Zlatan D. Dimitrov and Tihomir S. Hristov, “On the theory of MHD waves in a shear flow of a magnetized turbulent plasma”, 2007, *Bulgarian Astronomical Journal*, vol. 9, p. 51.
- T.M. Mishonov, M.V. Stoev and Y.G. Maneva, 2007, “On the origin of solar wind. Alfvén waves induced jump of coronal temperature”, *EPJD*, vol. 44, p.533-536.

Contributed papers in conference proceedings

- Y. G. Maneva, J. Araneda and E. Marsch, 2010, ‘Ion distributions in coronal holes and fast solar wind’. Refereed AIP conference proceedings of “Solar Wind 12” (CP1216), 21-26 June 2009, Staint-Malo, France. Editors: M. Maksimovic, K. Issautier, N. Mayer-Vernet, M. Moncuquet, and F. Pantellini; ISBN 978-0-7354-0759-6.
- Y. G. Maneva, J. Araneda and E. Marsch, 2009, “Parametrically Unstable Alfvén-cyclotron Waves and Wave-particle Interactions in the Solar Corona and Solar Wind”. AIP conference proceedings of “School and Workshop on Space Plasma Physics” (CP1121), 31 August - 7 September 2008, Kiten, Bulgaria. Editor: I. Zhelyazkov; ISBN 978-0-7354-0656-8.
- T. M. Mishonov, Z. D.Dimitrov, Y. G. Maneva and T. S. Hristov, 2009, “Amplification of Slow Magnetosonic Waves by Shear Flow: Heating and Friction Mechanisms of Accretion Disks”. AIP conference proceedings of “School and Workshop on Space Plasma Physics” (CP1121), 31 August - 7 September 2008, Kiten, Bulgaria. Editor: I. Zhelyazkov; ISBN 978-0-7354-0656-8.

Acknowledgements

I would like to acknowledge my previous tutor Prof. Todor Mishonov, who urged me to apply for my current position on the first place, and without whom I would never have taken the initiative of becoming a PhD at the Max Planck Institute for Solar System Research (MPS).

I would like to thank MPS and the International Max Planck Research School (IMPRS) on Physical Processes in the Solar System and Beyond at the Universities of Göttingen and Braunschweig for funding the research, presented in this thesis. I would like to thank my family, and Jaime, Volkmar and M. Madjarska for their continuous support and understanding, together with all my Bulgarian friends (especially Du) without whom I would never be able to make it.

I am grateful to my supervisor, Prof. Eckart Marsch, for taking me as a student and for believing that I can handle. Next thanks go to all the group members for the rare, but stimulating discussions about solar physics, with special thanks to Redouane, who gave me plenty of useful tips and advice during my first months in Lindau. I am also thankful to Prof. Wolfgang Glatzel for accepting me as his student at the University of Göttingen and always being helpful.

Another gratitude goes to the coordinator of the IMRS school, Dr. Dieter Schmidt, for creating a good academic atmosphere, and for his care and advice during my work at the MPS.

I'd like to specially thank Jonathan and Robert for their precious help and support in various discussions, as well as different tips in computing. Many thanks go to Prof. Manfred Schüssler and his group for showing me what a true research group should be like. I'm grateful to Raphael, as well, for all the tips in IDL I've received and to Prof. Franz Kneer for providing me with an additional office to work in Göttingen.

Here I need to add all the IMPRS colleagues, who were especially helpful in the last and rather important "writing" stage, as well as my climbing friends, with whom plenty of relaxing weekends in the nature helped to clear my mind and gave me strength to keep on working on my research.

Finally, I'm grateful to all the administrative staff at the MPS for their efforts, help and availability.

Lebenslauf

Persönliche Daten

Name: Yana Maneva
Geburtstag: 18.05.1982
Geburtsort: Sofia, Bulgarien
Staatsbürgerschaft: Bulgarisch

Schulausbildung

09/1988-06/1995: Grundschule, Sofia, Bulgarien.
09/1995-06/2000: Realsprachschule für Englisch
mit Intensivkursen in Mathematik,
Geschichte und Spanisch,
Sofia, Bulgarien.

Studium

10/2000-07/2004: Diplom in Physik, Arbeit in Theoretischer
Astrophysik, Sofia Universität "Sv. Kliment
Ohridski", Sofia, Bulgarien.
10/2004-06/2006: Magister in Theoretischer Physik, Arbeit in
Supraleitung, Sofia Universität "Sv. Kliment
Ohridski", Sofia, Bulgarien.

Promotion

02/2007-08/2010: Doktorarbeit am Max-Planck-Institut für
Sonnensystemforschung, Katlenburg-Lindau,
Deutschland.